A Bispectral Analysis of Nearshore Flow Meter Data

by Devon James Danielson

A thesis submitted to the faculty of graduate studies in partial fulfillment of the requirements for the degree of

Master of Science

Department of Civil Engineering
University of Manitoba

Winnipeg, Manitoba, Canada

April, 2003

THE UNIVERSITY OF MANITOBA

FACULTY OF GRADUATE STUDIES

*****

COPYRIGHT PERMISSION PAGE

A BISPECTRAL ANALYSIS OF NEARSHORE FLOW METER DATA

BY

DEVON JAMES DANIELSON

A Thesis/Practicum submitted to the Faculty of Graduate Studies of The University of Manitoba in partial fulfillment of the requirements of the degree of

Master of Science

Abstract

The movement of beach sediments, leading to erosion and accretion, has been shown by many researchers to be fundamentally associated with nearshore wave field properties such as wave skewness. With recent advancements in velocity sensors, large collections of high quality velocity data are being gathered and examined throughout the world. SandyDuck '97, the source of the data used herein, is one such collaborative effort of experimenters. Faculty and students from Dalhousie University, the University of Manitoba and Memorial University of Newfoundland formed the Canadian part of this collaboration. Over two months of semi-continuous data were collected from five different locations in the nearshore. Two of these locations were equipped with Acoustic Doppler Velocimeter (ADV) sensors in addition to traditional Electromagnetic Current Meters (EMCM) and pressure sensors.

Using the ADV and EMCM from one of the two frames, a large dataset of concurrent and relatively collocated velocity records has been compiled. These data facilitate a detailed comparison of the instrumentation that addresses concerns over the accuracy of the EMCM's. The results indicate very good agreement between these records. Deviations between the measurements from the two instruments are discussed and can likely be explained simply by local variations, especially vertical variations in the wave field.

Using the ADV records from over a two month period, contributions to velocity skewness are examined. The majority of the velocity skewness at this location is shown to arise from only three of a possible ten terms resulting from an expansion of the cross-shore velocity into three parts; the mean flow, the short wave part and the long wave part. The three dominant terms involve; i) the skewness from the short wave part, ii) the correlation between incident short waves and the mean flow, and iii) the correlation between the wave envelope and the long wave motion.

Also using this ADV data, parameterization techniques that attempt to relate skewness to nearshore parameters are evaluated. The main parameter used for these parameterization is the Ursell number. The formulations suggested by these parameter techniques are shown to inadequately describe the skewness because of an apparent lack of wave asymmetry which, when present, leads to an eventual decrease in wave, and therefore velocity, skewness.

Acknowledgments

I would like to thank my advisor, Dr. Jay Doering for his continuous support, guidance and patience throughout my graduate research. I have very much enjoyed being Jay's student and am proud to have earned a degree under his guidance.

Thanks also to my family, especially to my wife Cristi and my parents, for their encouragement over the past few years.

Finally, I would like to thank my examining committee members, Dr. Peter Rasmussen and Dr. G. Naterer for their time and effort, and for their questions and contribution to this thesis.

Table of Contents

List of Figures

List of Tables

Nomenclature

a	[L]	wave amplitude
A	[-]	total asymmetry
A_{ww}	[-]	asymmetry due to wind-wave frequencies
$A(f)$	[L]	complex Fourier coefficient
$B(f_1, f_2)$	[units^{3}T^{-2}]	complex bispectral estimate
B_{pp}	[-]	normalized biamplitude due to self-self interaction of the primary
B_{ww}	[-]	normalized biamplitude due to wind-wave frequencies
c_d	[-]	coefficient of bottom drag
C	[-]	ratio of seaward to shoreward energy dissipation
f	[T^{-1}]	frequency
f_c	[T^{-1}]	cutoff frequency for high/low-pass filter
f_p	[T^{-1}]	frequency of spectral peak
f_t	[T^{-1}]	terminal frequency for high/low-pass filter
g	[LT^{-2}]	constant of acceleration due to gravity
$G(f)$	[-]	gain correction for electromagnetic current meters
H_s	[L]	significant wave height
h	[L]	local depth of still water
i	[-]	imaginary unit, $\sqrt{-1}$
i_b		bedload transport
$\hat{i}$	[-]	unit vector in the cross-shore direction
k	[L^{-1}]	radian wavenumber
K		kurtosis
L	[L]	incident wavelength
L_o	[L]	deep water wavelength
P	[units^{2}T^{-1}]	spectral energy density
s^2		variance
S	[-]	total skewness
S_{ww}	[-]	skewness due to wind-wave frequencies
n	[-]	length (number of points) of a time series
t	[T]	time

$\tan\phi$	[-]	sediment internal angle of friction
T_p	[t]	peak period
Ur	[-]	Ursell number
u	[LT^{-1}]	cross-shore velocity
u_f		
u_s	[LT^{-1}]	short wave (high frequency) contribution to cross-shore velocity
u_l	[LT^{-1}]	long wave (low frequency) contribution to cross-shore velocity
v	[LT^{-1}]	long-shore velocity
v_f	[LT^{-1}]	
β	[-]	beach slope
ε_b	[-]	efficiency factor
ε^2		integrated variance
φ	[-]	surf similarity parameter
$\omega(f)$	[°]	phase correction for flow meters
$\zeta(t)$		a stationary random function of time
γ^2	[-]	coherence squared
η	[L]	water surface elevation
θ	[°]	instrumentation correction angle
ρ	[ML^{-3}]	fluid density
τ	[T]	time lag

General Notation

a^*	complex conjugate
$\overline{a}$	mean quantity
$\lvert a \rvert$	modulus or amplitude
E[ ]	expected value or average operator
< >	time average
$\Re\{\}$	real part
$\Im\{\}$	imaginary part

CHAPTER 1

Introduction

1.1 Background

Coastal environments have always attracted human interest. Recreational properties along rivers, lakes and ocean shorelines are in demand now, more than ever. The very same thing that makes these properties desirable also threatens to take them away. The complex dynamics of coastal environments continue to overcome man's attempt to subdue and control coastal erosion. Beach environments are no exception.

Researchers have long been trying to understand the processes leading to the erosion and accretion of beach sediments, with theories of beach equilibrium dating back to the late 1800's. These earliest theories were generally based on the forces acting on a single grain, such as "the null-point hypothesis". This theory, although attributed to Cornaglia (1889), was developed and tested by Ippen and Eagleson (1955), Eagleson and Dean (1961) and Eagleson *et al.* (1965). The underlying idea of this theory is coarser material of a well-graded sample of sediment deposited seaward of breaking will be transported offshore, while the finer material will be transported onshore. Field observations, however, disagree with this suggestion.

Others have tried, with little success, to develop empirical models for predicting cross-shore beach equilibrium that relate sediment transport rates to incident wave characteristics such as wave steepness, height or power. These models, often result in tenuous correlations and lack theoretical justification.

Cornish (1898) noticed that the shoreward velocity associated with a wave crest was more effective at moving coarse sediment than was the seaward velocity associated with the wave trough, thus introducing the link between sediment transport and velocity skewness. This is consistent with Stokes theory (1847) that predicts that the onshore velocity is stronger and shorter in duration than the offshore velocity. Wave skewness and asymmetry are illustrated in Figure 1.1, and are exhaustively discussed in further sections of this thesis.

Inman and Bagnold (1963) were the first to formalize the importance of a skewed oscillatory velocity field to cross-shore beach equilibrium. In doing so, they developed an equation for the equilibrium beach slope,

$$\tan(\beta) = \tan(\phi)\left(\frac{1-C}{1+C}\right), \tag{1.1}$$

where β is the beach slope, $\tan\phi$ is the sediment coefficient of friction (Coulomb, 1776), and C is the ratio of the energy dissipated due to friction during seaward sediment transport to that during the shoreward transport of sediment. Inman and Frautschy (1966) proposed that this ratio, C, was proportional to a function of 3rd powers of the cross-shore flow.

Bagnold's model for bedload transport (Bagnold, 1963, 1966), as developed and formulated by Bailard and Inman (1981), is

$$\langle i_b \rangle = \frac{\varepsilon_b c_d \rho}{\tan\phi}\left[\langle u^3 \rangle - \frac{\tan\beta}{\tan\phi}\langle |u|^3 \rangle \hat{i}\right], \tag{1.2}$$

where i_b is total bedload transport, ε_b is an efficiency factor, c_d is the bottom drag coefficient, ρ is the water density, u is the total instantaneous velocity vector, $\hat{i}$ is a unit vector in the onshore direction, $|\ |$ denotes the modulus of, and $< >$ denotes a suitable time average. This model for bedload transport is particularly attractive because it contains only a few "free parameters", ε_b and c_d and implicitly incorporates the downslope component of gravity by including beach slope dependence. The principle assumptions of the model are 1) the bedload transport responds instantaneously to the flow and 2) the flow is fully developed; i.e., the model does not describe the initiation of sediment movement, nor does it apply to large particles that may move only intermittently during peak flows – this has been incorporated into more recent formulation of the model (Hardisty, 1983; Bowen and Doering, 1984).

In the shoaling region it is usually reasonable to assume near-normal incidence waves and weak long-shore currents, in which case the total instantaneous velocity vector **u** can be replaced by the cross-shore component of velocity u; thus,

$$\langle i_b \rangle = \frac{\varepsilon_b c_d \rho}{\tan\phi}\left[\langle u^3 \rangle - \frac{\tan\beta}{\tan\phi}\langle |u|^3 \rangle\right]. \tag{1.3}$$

This is the same formulation for bedload transport used by Bowen (1980) to investigate beach equilibrium. If Beach equilibrium occurs by bedload transport $\langle i_b \rangle = 0$, then

$$\tan(\beta) = \tan(\phi)\frac{\langle u^3 \rangle}{\langle |u|^3 \rangle}. \tag{1.4}$$

Various definitions of velocity skewness have been studied, but the usual definition, is given by,

$$S = \frac{\langle (u-\overline{u})^3 \rangle}{\langle (u-\overline{u})^2 \rangle^{3/2}}. \tag{1.5}$$

Most researchers have adopted a convention whereby they compute moments about the record mean. Because both moment terms in (1.4), $\langle u^3 \rangle$ and $\langle |u|^3 \rangle$ are computed from the total, instantaneous flow, they include any contribution from the mean flow. The effect of the mean is often removed in order to compare moments between records. Also, because bispectral analysis is the Fourier transform of the second-order covariance function, the mean flow is removed in the transform. Bispectral analysis cannot therefore elucidate any interactions with the mean flow.

The use of Bailard and Inman's model (1.3) is very difficult because one would require detailed spatial and temporal measurements of the flow field in order to estimate $\langle u^3 \rangle$ and $\langle |u|^3 \rangle$. Estimation of these parameters by other means would therefore be very desirable. Linear theory cannot be used to estimate third-order moments because it represents the sea surface as a linear superposition of waves of random phase, which by definition has zero skewness.

Some researchers have modeled the spatial variability of velocity moments using Stokes waves. This is questionable since shoaling a Stokes wavetrain does not lead to wave asymmetry because the harmonic components of the wavetrain remain phase-locked and in phase with the primary, (Doering, 1995). Waves in nature become asymmetric as the phase of the n^{th} harmonic is shifted by $n\pi/2$.

(Figure 1.1). This phase shifting not only leads to an increase in wave asymmetry; it also leads to an eventual decrease in wave skewness.

Huntley and Bowen (1975) were among the earliest to obtain relatively accurate measurements of the nearshore flow using fast response electromagnetic current meters. In their study, they contrasted the hydrodynamics over shallow and steeply sloping beaches. Over the shallow slope, they observed an onshore cross-shore velocity skewness that decreased slowly with decreasing depth. Over the steep slope, however, they noticed the cross-shore skewness decreased rapidly as the waves reached shallower depths and changed sign after reaching the break zone, indicating an offshore skewed flow in the surf zone.

Greenwood and Sherman (1984) showed that the cross-shore velocity skewness (including mean flow contributions) tended to be positive lakeward of the bar and negative landward, over a gentle sloping, multiple barred beach in the Great Lakes.

Guza and Thornton (1985) examined the spatial and temporal variations of many velocity moments including the third moment, which is related to the skewness. They found that the velocity skewness increased as the wavetrain began to shoal, reached a maximum seaward of breaking and then decreased.

Elgar and Guza (1985) used bispectral analysis to analyze skewness and asymmetry of shoaling surface gravity wave pressure measurements. They noticed that in deep water, phase coupling occurred between low and higher frequencies within the spectral peak, suggesting a difference interaction between primary frequencies. They also observed that the low frequency wave was 180° out of phase with the primary, indicative of bound long waves. In shallower water, they noticed numerous triad interactions involving 1^{st}, 2^{nd}, 3^{rd} and higher harmonics and an evolution of the phase relations between these wind-wave frequency triads consistent with the steepening of the shoreward face of a progressive wave. In very shallow water, the phase coupling between low and wind-wave frequencies resulted in a skewness with opposite sign to, and about 40% of the magnitude of, the skewness arising from interactions between the primary and higher frequencies.

Foote et.al. (1992) examined various contributions to total cross-shore velocity skewness using a simpler approach. They chose to consider the total instantaneous cross-shore velocity as the sum of three constituent parts, i.e.,

$$u = \bar{u} + u_s + u_l, \tag{1.6}$$

where u = the total instantaneous velocity field,

$\bar{u}$ = the mean flow,

u_s = the short wave contribution, and

u_l = the long wave contribution.

By expanding $\langle u^3 \rangle$ in terms of these three components, the normalized cross-shore velocity skewness becomes

$$\langle u^3 \rangle = \overline{\left(\bar{u} + u_s + u_l\right)^3} \tag{1.7}$$

$$= \bar{u}^3 + \overline{u_s^3} + \overline{u_l^3} + \overline{3\bar{u}u_s^2} + \overline{3\bar{u}u_l^2} + \overline{6\bar{u}u_s u_l} + \overline{3u_l^2 u_s} + \overline{3u_s^2 u_l} + \overline{3\bar{u}^2 u_s} + \overline{3\bar{u}^2 u_l}$$

Term (1) (2) (3) (4) (5) (6) (7) (8) (9) (10)

The ten terms of this expansion each represent different contributions to the total velocity moment; their contributions are as follows:

Term 1 is the mean flow cubed

Term 2 represents the short wave velocity skewness

Term 3 represents the long wave velocity skewness

Term 4 represents the Inman/Bagnold-type term where short waves mobilize the sediment, which is then moved by a mean flow.

Term 5 is similar to Term 4, except the sediment mobilization is due to the long waves.

Term 6, Term 7, Term 8 } correlations between short and long wave components.

Terms 9 & 10 are, by definition, very small (≈0) because they involve the averaging of random variables u_s and u_l, respectively.

They found that particular moment terms dominate through the nearshore zone. Seaward of the surf zone, terms 2, 4 and 8 dominated the total skewness, whereas within the surf zone terms 2, 4 and 5 dominated. In both cases the mean flow contribution was significant, (i.e., term 4).

Foote and Huntley (1994) examined cross-shore current and suspended sediment data. They compared skewness contributions from each of mean, long and short waves to sediment suspension data.

Doering and Bowen (1995) examined the spatial variation of velocity skewness and asymmetry for shoaling and breaking surface gravity waves. Using the Ursell parameter, they successfully parameterized the cross-shore velocity skewness and asymmetry arising from phase coupling between wind-wave frequencies. This was done using the bispectrum as an analysis tool. It showed that the variation of normalized integrated biamplitude arising from the self-self interaction of the primary is well described by the Ursell number. They also developed the following equations for integrated biamplitude, skewness and asymmetry arising from wind-wave components, i.e.,

$$B_{ww} = 0.8 + 0.62\log(Ur), \tag{1.8}$$

$$S_{ww} = [0.8 + 0.62\log(Ur)]\cos\{[-90° + 90°\tanh(0.73/Ur)]\pi/180\}, \text{ and} \tag{1.9}$$

$$A_{ww} = [0.8 + 0.62\log(Ur)]\sin\{[-90° + 90°\tanh(0.73/Ur)]\pi/180\}, \tag{1.10}$$

respectively. The Ursell parameter was computed using a shallow water approximation and is given by

$$Ur = \frac{3}{4}\frac{g}{8\pi^2}\frac{H_c T_p^{\,2}}{h}. \tag{1.11}$$

Doering et. al. (2000) developed an analytical expression for the skewness of a large collection of data from a number of field environments using genetic programming. The expression, shown in equation 1.13, provided a good fit to data collected during field experiments in Terschelling, Netherlands and Duck, North Carolina (1994 & 1997). This expression was chosen from a number of

candidates because it had the highest correlation with the measured data. It is difficult, as acknowledged by the authors, to observe a clear physical meaning of the expression

$$S = -14.076\left[\tanh\left(1 + a_1 + \sqrt{a_2 + a_3} + a_4\right)\right] + 14.133, \tag{1.12}$$

where

$$a_1 = \frac{2.582}{L/h}, \tag{1.13}$$

$$a_2 = \left|\xi - 0.207\right|, \tag{1.14}$$

$$a_3 = \sqrt{\left|-0.22 + \left|\frac{\xi \tanh(Ur) + 2.527}{L/h}\right|\right| + \left(\frac{L/h}{Ur^2}\right)}, \tag{1.15}$$

$$a_4 = \left|\frac{L/h}{Ur} - 0.218\right|, \text{ and} \tag{1.16}$$

$$Ur = \frac{H_s L^2}{h^3}. \tag{1.17}$$

L is the incident wave length, h is the local still water depth, H_s is the significant wave height, and ξ is the surf similarity parameter.

1.2 Research Objectives

It is generally accepted that wave and therefore velocity skewness is a major contributor to the suspension of sediment in nearshore sandy environments. Most of the research that suggests this sediment transport link to wave skewness has been done using velocity data obtained with electromagnetic current meter (EMCM) technology. With the advent of newer acoustic technologies, such as the Acoustic Doppler Velocimeter (ADV), it is thought that our ability to measure near-bottom water velocities has been considerably improved. These instruments have the ability to remotely measure the three components of velocity, at sampling rates up to 25 Hz. The database used for this research is comprised of over two months of semi-continuous data from two nearshore stations, each with collocated ADV and EMCM instrumentation.

Using these data, the objectives of this research are therefore:

i) to attempt to validate or scrutinize existing research that is based on electromagnetic velocity measurements by comparing collocated EMCM and ADV measurements,

ii) to examine the adequacy of ADV instrumentation in measuring near bottom velocities,

iii) to examine the parameterization of skewness and asymmetry in the nearshore, and

iv) to examine the relative contributions to skewness from the mean flow, infragravity and gravity waves.

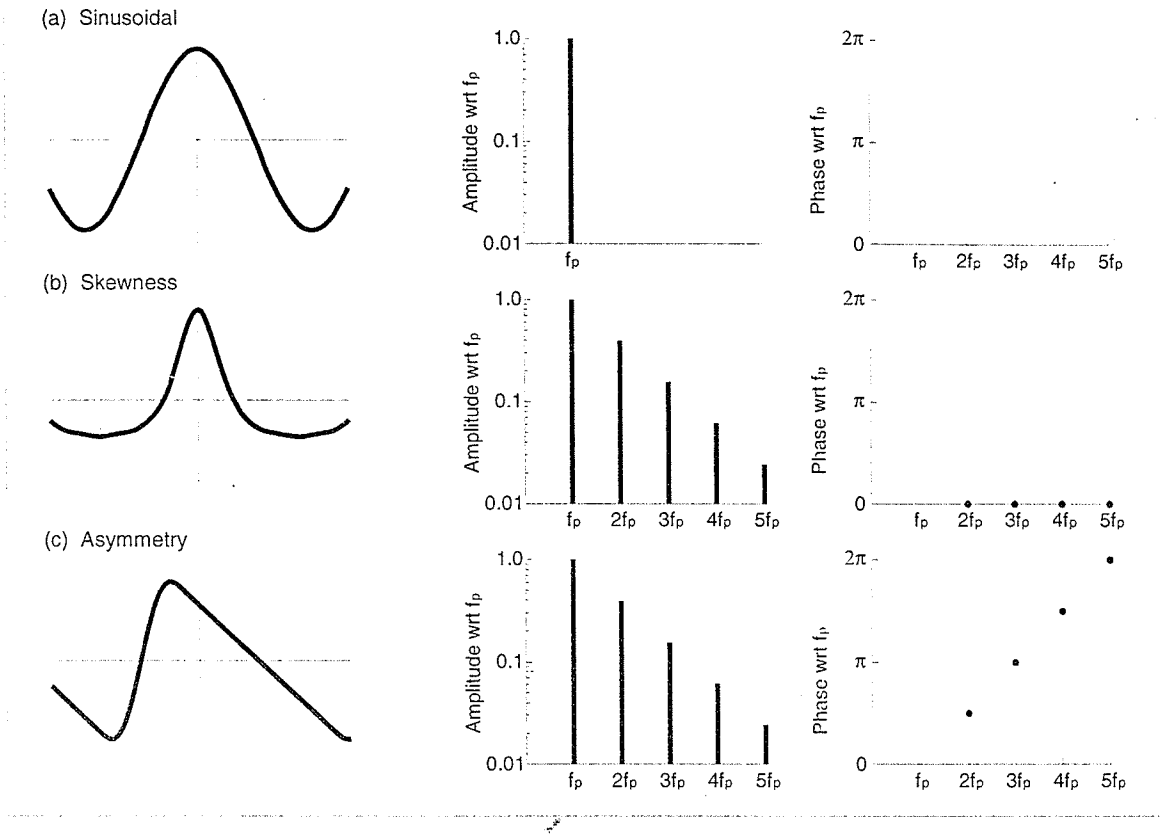

Figure 1.1 (a) Schematic showing a sinusoidal profile that is symmetric with respect to both the horizontal and vertical. (b) A skewed profile, i.e., one that lacks symmetry with respect to the horizontal. Note that this profile is vertically symmetric. (c) An asymmetric profile, i.e., one that lacks symmetry with respect to the vertical. Note that this profile is horizontally symmetric. The spectral composition and phase of the harmonics with respect to the primary frequency (f_p) is shown to the right of the profile. Notice that (b) and (c) have identical spectral composition. However, the phase of the n^{th} harmonic is shifted by $n\pi/2$ for the asymmetric profile, whereas the harmonics are all phase-locked and in phase for the skewed Stokes-type wave. A phase relation between the harmonics and the primary other than that shown in (b) and (c) results in a profile that is both skewed and asymmetric. (source: *Doering* 1988)

CHAPTER 2

The Field Experiment

2.1 Introduction

The data used in this research was collected during an international collaborative effort of over 250 participants in Duck, North Carolina. This experiment, known as SandyDuck '97, was the most recent of a series of experiments at Duck. Hosted by the U.S. Army Corp. of Engineers, the experiment was held at the U.S. Army Corp., Office of Naval Research Field Research Facility in Duck, N.C, near Cape Hatteras. The facility is equipped with instrumentation for wind, wave, current and tidal measurement. During the experiment, these measurements were supplemented with bathymetry, deep-water wave data and directional wave data. The physical characteristics of the experiment site were typical of the sandy shores of the barrier islands of North Carolina's coast.

The research herein is part of one of a series of experiments within SandyDuck '97, performed by a Canadian team of investigators and students from Dalhousie University, the University of Manitoba and Memorial University of Newfoundland. The scientific objectives of this group were numerous, emphasizing nearshore sediment and fluid dynamics. The Canadian experiment was to involve the 6-node, L-shaped array shown in Figure 2.1, however, node E was never instrumented. Instruments deployed included sonar imaging equipment, combination pressure gauge and current meter (PUV) sensors, 3-component coherent Acoustic Doppler Velocimeter (ADV) velocity profilers, temperature sensors, frame-tilt sensors, and broadband hydrophones for ambient noise measurements.

2.2 The Experimental Site Nearshore Environment

Coastal landforms can vary greatly in character. The geological processes that occur may be dynamic and rapidly changing or they can be comparatively stable. The low, long and narrow barrier islands of the United States typically retreat at rates of ½ to 2 meters per year, however rates in excess of 20 meters per year have been observed.

The experimental site chosen was typical of the North Carolina Barrier Islands (Figures 2.2 to 2.4). The nearshore bottom slopes were roughly 1:100, with a bar located approximately 50-70 meters offshore. Figure 2.5 illustrates the cross-shore profiles near the two instrument frames used in this study.

2.3 Instrumentation

The instrumentation deployed by the Canadian team of investigators was positioned as shown in Figure 2.1. Frames A through D formed a cross-shore array of measurements and frames A and F were to provide some insight into the long-shore structure of the nearshore dynamics. Figure 2.5 illustrates cross-shore profiles at stations 875, 975 and 1025 (FRF coordinate system long-shore measurements, refer to Figure 2.1).

The data used for this research was processed and grouped into three data sets: (1) EMCM (sampled continuously @ 2Hz), (2) ADV (sampled intermittently @ 25Hz) and (3) Concurrent, nearly-collocated EMCM and ADV (@ 2Hz and 25Hz, respectively). The first data set was used to examine the contributions to the bulk skewness arising from the low frequency, high frequency and mean flow velocities. The second was to examine parameterization techniques. The third data set was required to facilitate the inter-comparison. To satisfy these requirements, only the ADV, EM and pressure sensors on frames B and F could be used. The usefulness of the data collected at frame F was limited as a result of intermittent burial of the sampling volume and boundary-induced turbulence and sediment suspension. The data recorded by each of these is described in §2.4.

2.3.1 The SonTek ADV-Ocean

Both of the frames used for this study (B & F) were equipped with a SonTek Acoustic Doppler (Ocean) Velocimeter (ADV). The respective elevations of each ADV transducer face on frames B and F were –2.46 m and –1.5 m, National Geodetic Vertical Datum (NGVD), respectively. The ADV, and accompanying software, calculates three components of velocity within a remote sampling volume located approximately 18 cm away from the transducer face (Figure 2.6). The transducer transmits a series of short sound pulses at a known frequency. Each sound pulse travels through the water and is reflected in all directions by the particulate matter in the water. A portion of this energy reaches the sampling volume and is reflected back to the three receivers on the ADV. The software then uses a technique called pulse coherent (or pure coherent) processing to resolve the 3D velocity field relative to the orientation of the probe. A detailed explanation of the principles of operation is given by SonTek (1996).

2.3.2 The Marsh-McBirney Electromagnetic Current Meter

Each of the five instrument frames deployed by the Canadian team included Marsh-McBirney Electromagnetic Current Meters (EMCM). Because the elevations of these units were not available, they were estimated using the water levels measured by the FRF (NGVD) at the pier and the measured pressure records at each frame. For each of a series of pressure records, the mean pressure (meters of water) was subtracted from the water surface elevation (NGVD). The resulting time series of EMCM elevation estimates were then examined, any apparent outliers were removed, and the remaining values were averaged giving an approximation of the instrument elevation. This provides only an estimate of the elevation of the current meters, given that the local water surface elevation could be affected by factors such as radiation stress and that the pressure measurements were periodically affected by sand collecting in the tubes. For the purposes herein, however, only an approximate elevation is necessary because above the bottom boundary-affected region the flow dynamics should be very similar. Figure 2.7 illustrates the above-described estimation. The EMCM elevations on frames B and F were -0.40 m and -0.55 m (NGVD), respectively.

The EMCM's operate on the principle of Faraday's Law, which states that a conductor moving in a magnetic field induces an electrical potential that is proportional in magnitude to the velocity of the motion of the conductor. This electrical potential acts at right angles to both the direction of motion and the magnetic field axis. This magnetic field is generated by driving a coil that is located in the head, with an alternating square wave, (Doering 1988). The four electrodes on the head of the probe (Figure 2.8) are located in a plane normal to the magnetic field generated by the solenoid. These electrodes are capable of measuring two orthogonal components of induced voltage (i.e., flow) in the plane that they define. In our case, the probe was oriented so that the four electrodes were located in a horizontal plane, allowing direct measurements of the two components of the horizontal flow. These data were rotated in order to align their axis with those of the ADV; see §2.5.3.

2.4 The Field Data

With the completion of the experimental field program, the Canadian investigation team left North Carolina with a large amount of data from each of the current-meters and pressure sensors. The quality of these data varied, and not all of it was suitable for this research.

2.4.1 ADV Data

The Acoustic Doppler Velocimeters were configured to sample the three component velocity field at a rate of 25 Hz. Their operation was not continuous, recording for approximately 20 minutes at a time either once or twice an hour, depending on the sea state. The data was internally converted to velocities by the SonTek package in real-time, stored on the main server in the Canadian onshore lab and then written to compact discs. In addition to the velocity data, the SonTek instrumentation recorded sample-to-bed distance, sound speed and some quality control data. A GPS was used to record atomic-clock times for synchronization of all data. Descriptions of these data follow.

- ***Speed of Sound:*** Because the speed of the acoustic pulses through water is critical in the velocity computations, it was recorded for each record. This value is a function of temperature and salinity, and is automatically accounted for in the velocity calculations. This parameter was therefore not required post-experiment.

- ***Sample to Boundary Distance:*** The SonTek instrumentation measures the distance from the sampling volume to the bed. Unfortunately, only one value is recorded per velocity record. A negative value is recorded in situations where the boundary cannot be detected. This happens when the distance is either too large or too small (i.e., buried sampling volume). This can also happen when the sediment concentrations are too high. In some cases the distance to boundary could not be measured, yet the data looks real (albeit very turbulent). The distance to the boundary for these records could only be speculated by examining those records before and after it.

- ***Return Signal Amplitudes and Correlation's:*** In order to assess the quality of the ADV data, the SonTek units record signal quality data. This includes signal-to-noise ratios, signal strength and outgoing signal/return signal correlations.

2.4.2 EMCM Data

The EMCMs measured the horizontal velocities at a rate of 2 Hz. These instruments operated almost continuously, with scattered downtimes for technical problems. Generally, these data were collected in ½-hour records.

The coordinate systems of these velocity measurements depended on the orientation of the probes, which were periodically bumped and rotated, presumably by debris. Divers measured these rotations occasionally throughout the experiment.

In order to measure water velocities, the instruments required calibration, which was done using tow tank experiment data in the laboratory facility of the Oceanography Department at Dalhousie University. In doing this, the sensor is towed at different speeds and directions. "Data from both flow directions is used to avoid obtaining an erroneous offset. A linear least-squares regression is used to determine the electronic offset and linear gain calibration factor" (Doering, 1988), i.e.,

$$speed = offset + gain \times output(volts).$$

Using these values of offset and gain for each instrument, the water velocities were computed in real time in the field.

2.4.3 Pressure Meter Data

Like the EM current meters, the pressure meters recorded the water pressure at a rate of 2 Hz. Obviously, the pressures recorded by this instrument should have been independent of their orientation. Because the pressure tubes were mounted facing upwards, however, sand tended to collect inside them raising concerns as to the data quality. These instruments were positioned adjacent to the EM probes.

2.5 Data Processing

Three data sets were used for the analysis described in this thesis. The first two required only data checking and despiking (if necessary), the last however required concurrent time series of ADV and EM velocity measurements to facilitate the intercomparison. This requirement limited the data substantially. If either the EM or the ADV data was bad, neither could be used. Also, with the ADV sampling for only twenty minutes at a time, either once or twice an hour (depending on the mode of operation), much of the EM data was not useful. Much larger data sets, however, were available for the remaining analysis (data sets 1 & 2) because most of these limitations did not apply.

2.5.1 Data Set #1 (EMCM Velocity Measurements)

Using automated routines, all of the electromagnetic current meter data was checked for outliers, which were subsequently removed. Almost all of the outlier values in these data have a dropout value of 32,767. These points were easily found and replaced with the average of the adjacent points. The few remaining outliers were found manually and the time series were corrected by either replacing these points, salvaging a portion of the time series or by simply discarding the record. Unfortunately, most of these bad data occurred in groups, making their replacement impossible.

In order to correct the gain and phase attenuation associated with the transfer function of the electromagnetic flow meter electronics, a gain phase correction was applied to the data. By carrying out a nodal analysis of the nominal electronic components, Doering, (1988) found the transfer functions for the two filters in the flow meter electronics to be

Filter 1

$$G_1(f) \approx 1.0, \quad f < 1Hz \tag{2.1}$$

$$\varphi_1(f) = \tan^{-1}\left\{\frac{2\pi f - 17.9}{17.7}\right\} + \tan^{-1}\left\{\frac{2\pi f + 17.9}{17.7}\right\} \tag{2.2}$$

Filter 2

$$G_2(f) = 10^{-\left\{5.33 - \log\left(\sqrt{4\pi^2 f^2 + 42600^2}\right) - \log\left(\sqrt{4\pi^2 f^2 + 5^2}\right)\right\}} \tag{2.3}$$

$$\varphi_2(f) = \tan^{-1}\left\{\frac{2\pi f}{42600}\right\} + \tan^{-1}\left\{\frac{2\pi f}{5}\right\} \tag{2.4}$$

$G(f)$ and $\varphi(f)$ are the gain and phase corrections, respectively, and f is a frequency (Hz).

Throughout the field experiment, the electromagnetic current meters were found to abruptly move on their mounting rods. These movements, observed from the cross- and long-shore velocity measurements using principle axis theory, are believed to be due to debris impact, significant weed accumulation, etc. This required correction in order to maintain a consistent coordinate system. Also, in order to perform an intercomparison between the ADV and EM data, it was necessary to ensure that the cross-shore and long-shore axis of each data record coincided. For these reasons, the EM time series were rotated using the principal axis rotation method shown below:

$$\begin{bmatrix} u'_1 & v'_1 \\ u'_2 & v'_2 \\ u'_3 & v'_3 \\ \vdots & \vdots \\ u'_n & v'_n \end{bmatrix} = \begin{bmatrix} u_1 & v_1 \\ u_2 & v_2 \\ u_3 & v_3 \\ \vdots & \vdots \\ u_n & v_n \end{bmatrix} \times \begin{bmatrix} \cos\theta & \sin\theta \\ -\sin\theta & \cos\theta \end{bmatrix} \tag{2.5}$$

where u'_i is the rotated i^{th} term in the cross-shore velocity time series,
v'_i is the rotated i^{th} term in the long-shore velocity time series,
u_i is the i^{th} term in the cross-shore velocity time series,
v_i is the i^{th} term in the long-shore velocity time series, and
θ is the required rotation angle.

The data were rotated using angles as measured periodically by divers. In order to perform a check on these field measurements, a principle axis analysis was performed on each concurrent ADV and EMCM record. It was assumed that, because of the close proximity of these two instruments, the principle direction of wave propagation should have been the same at each. The difference in the angles as determined by the principle axis analysis for each instrument provided an estimate of the required EMCM-rotation angle. Figure 2.9 illustrates the measured and estimated rotation angles throughout October for frames B and F. The required rotation angles were via the following equations that estimate the angle of the principle axis vector that maximizes the cross-shore velocities and minimizes the long-shore velocities.

$$rotation = \tan^{-1}\left(\langle \eta(v) \rangle / \langle \eta(u) \rangle\right) \tag{2.5}$$

$$rotation = 0.5 \tan^{-1}\left(2\langle uv \rangle / \left[\langle u^2 \rangle - \langle v^2 \rangle\right]\right) \tag{2.6}$$

$$rotation = \tan^{-1}\left(\left\langle \left(v - \langle v \rangle\right)^2 \right\rangle / \left\langle \left(u - \langle u \rangle\right)^2 \right\rangle\right) \tag{2.7}$$

The variation between these values was considered acceptable, contrary to the aforementioned assumption, because of the horizontal and vertical distance between the two instruments.

2.5.2 Data Set #2 (ADV Velocity Measurments)

The ADV was manually observed for bad records and/or bad portions of records. Because of the large amounts of data available, records that contained segments of bad data were eliminated from the data set. An automated routine was applied to the remaining records in order to correct any outliers.

Most of the bad records were obvious, however, there were some cases when the sampling volume was too close to the bed and it became difficult to distinguish between turbulence and noise. Velocity accelerations, far exceeding those expected, were found near the bed. Figure 2.10 shows a sample of EMCM and ADV data. When very near the bottom, the ADV exhibits a much more noisy structure than the EMCM (mounted higher in the water column), even though it appears to follow the same (lower frequency) carrier waves. In order to assess this data, the accelerations of the time series were plotted, (Figure 2.11). Given that the magnitudes of these accelerations greatly exceed the accelerations due to the restoring force of gravity, ($g = 9.806\ m/s^2$), one would hypothesize that this

data is not merely turbulent fluctuations. It seems more likely, rather, that the rapid fluctuations are noise, caused by one or more of the reasons explained in §2.3.1.

SonTek (1996) lists a few sources of interference associated with boundary layer measurements. The first source is if the boundary enters the sampling volume. "In this case the ADV will be measuring the Doppler shift of the reflection from the boundary rather than the reflection from particles in the water. This will typically bias velocities towards zero (since the boundary is normally stationary), although this is not completely predictable (particularly if dealing with non-stationary or non-uniform boundaries)."

The ADV sends two pulses for each velocity measurement, therefore a second source of boundary interference can result if the reflection of the first pulse from the boundary overlaps the return signal of the second pulse from the sampling volume, Figure 2.12.

Some of the records that remained following this screening process required despiking. The ADV data had many more outliers than the EMCM, (with random values). Manual despiking was therefore not feasible. Instead, an automated routine was used that found all points lying beyond a window from a lowpass of the record. This window was defined as 4.1037 standard deviations of the lowpass-removed record (Equation 2.8). This is the value associated with the 99.996% confidence interval; i.e., 1 in 25,000. In order to obtain an acceptable fit for this lowpass, a first lowpass using a graham filter with cutoff and terminal frequencies of $4/T_p$ and $4/T_p+0.05$ was used. A window was created from this lowpass, defined by

$$Window = \begin{cases} LP + 4.1037\sigma_{u-LP} \\ LP - 4.1037\sigma_{u-LP} \end{cases}, \tag{1.8}$$

where u is the uncorrected time series, and LP is the time series generated by lowpass filtering u.

The procedure used is illustrated in Figure 2.13. This method was considered acceptable because of the Gaussian form that u-LP exhibited. Also, this Gaussian high frequency fluctuation also hints toward its unimportance as a contribution to skewness. Any points lying outside this window were replaced by the corresponding lowpass value. Because the spikes had a deleterious effect on the fit of this first lowpass, another was run on the new record. Having done this, another (better fitting)

window was created and the points that were replaced previously as well as any new outliers were replaced with the corresponding value of this new lowpass.

The number of points replaced in each record was recorded. In order to check the despiking algorithm, these values were compared to the number of points that should have exceeded the 99.996% confidence interval, (i.e., 1 in 25,000 points). The records generally had more than 50 data points replaced (up to nearly 350 points in the extreme cases), far more than should statistically have been expected. This would suggest that the replaced values were done so appropriately, because the statistics would suggest they were spikes.

2.5.3 Data Set #3 (Colocated EMCM and ADV Records)

Because each pair of "collocated" sensors on frames B and F were horizontally separated by approximately 0.70 m and 0.75 m, respectively, the velocity time series of each were lagged by an amount depending on the group velocity and the direction of wave propagation. In order to account for this, and because the real time was irrelevant in this analysis, a cross-correlation was performed in order to determine this lag for each record (after a temporary resampling of the ADV and EMCM to 10 Hz). One of the time series was then temporarily time-shifted by this amount and the two series were then truncated at their beginning and/or end so as to have the same starting and ending times. The lag was then removed and its value recorded for later use. The original sampling rates of 2 Hz and 25 Hz were retained for the EMCM and ADV time series, respectively.

Because most of the EMCM data recorded in September was subject to a time jitter problem, it was decided that only the data recorded in October would be used for the intercomparison analysis, leaving a still substantial dataset. The bad records were removed from the data set, identified using automated routines based on parameters such as the correlation between the EM and the ADV. Of course, resampling of the ADV data to 2 Hz was first required. The remaining data was visually checked for quality.

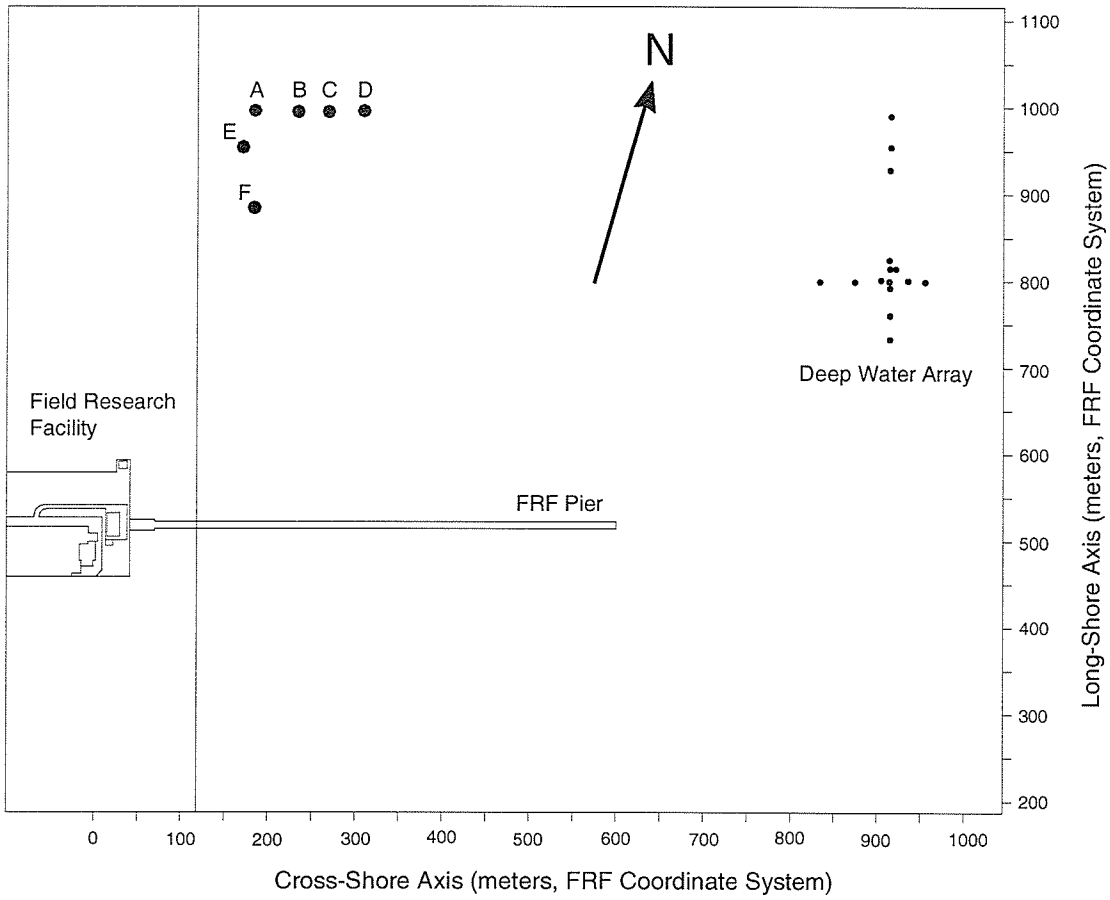

Figure 2.1. Instrument frame locations within the Field Research Facility Infrastructure. This research uses EMCM and ADV instrumentation on frames B and F.

Figure 2.2. Northern view of the coastline at the experimental site (bottom right). Photograph taken from the video tower.

Figure 2.3. View of the coastline at the experimental site with dune, beach and nearshore.

Figure 2.4. Southern view of the experimental site and FRF pier. Notice the CRAB surveying local bathymetry.

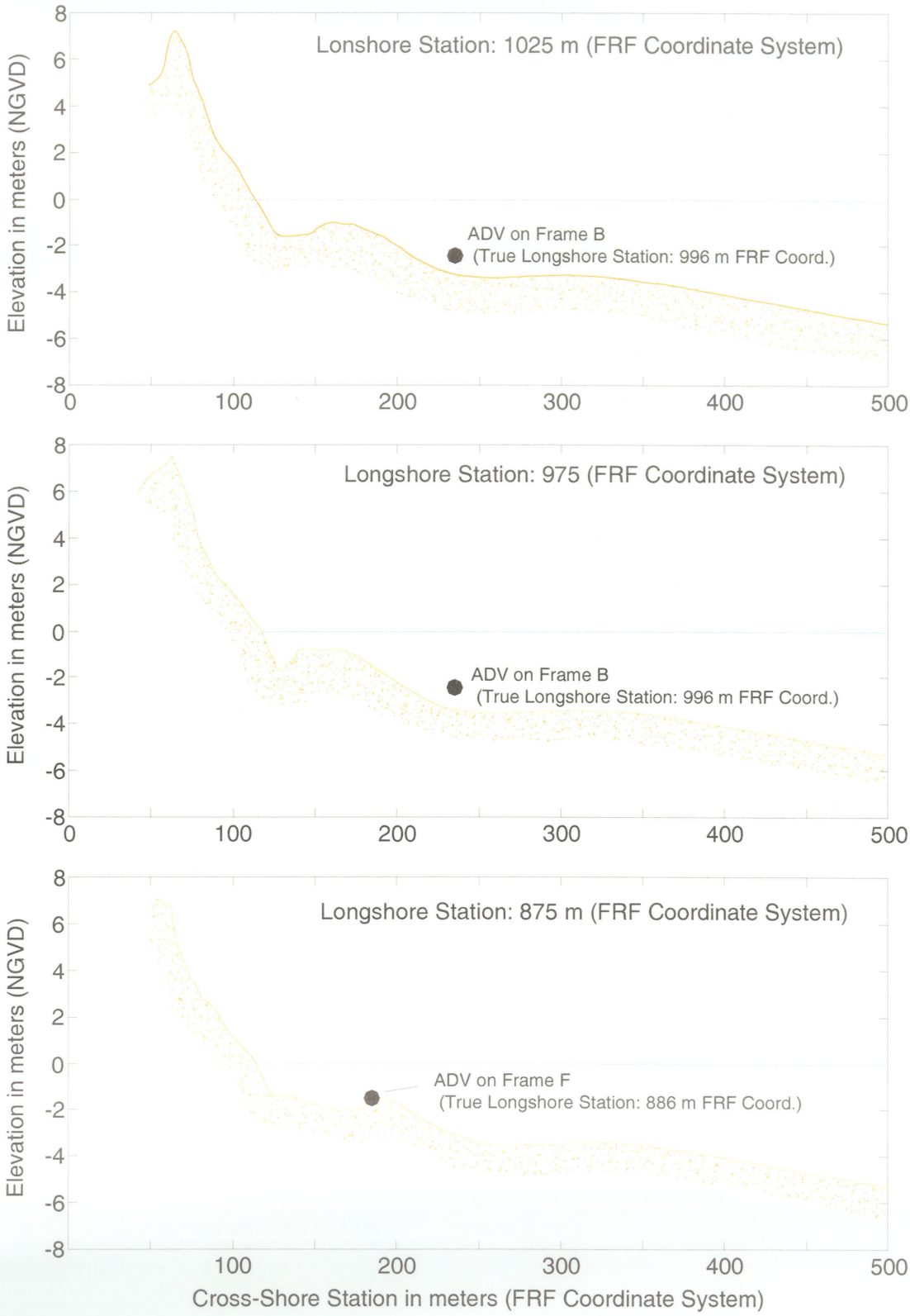

Figure 2.5. Cross-shore profiles near the instrument frames (See Figure 3.2.4 for a plan view of the experiment site) .

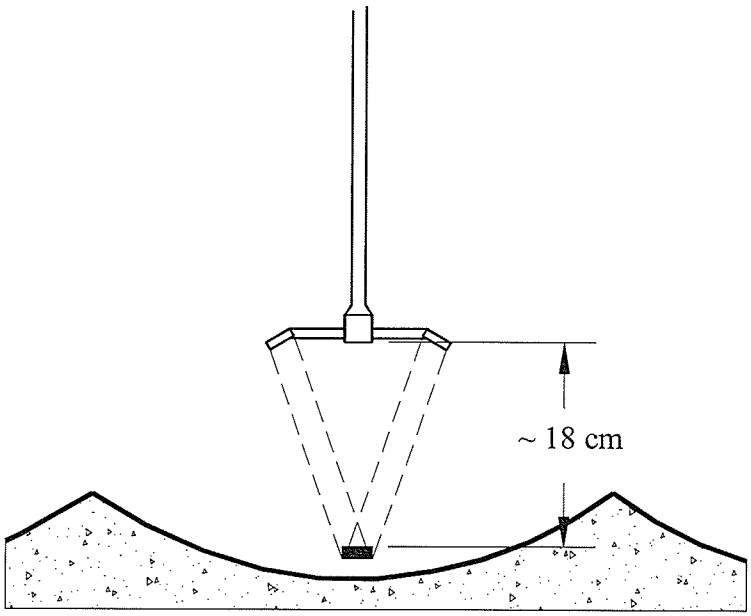

Figure 2.6. ADV Remote Sampling Strategy.

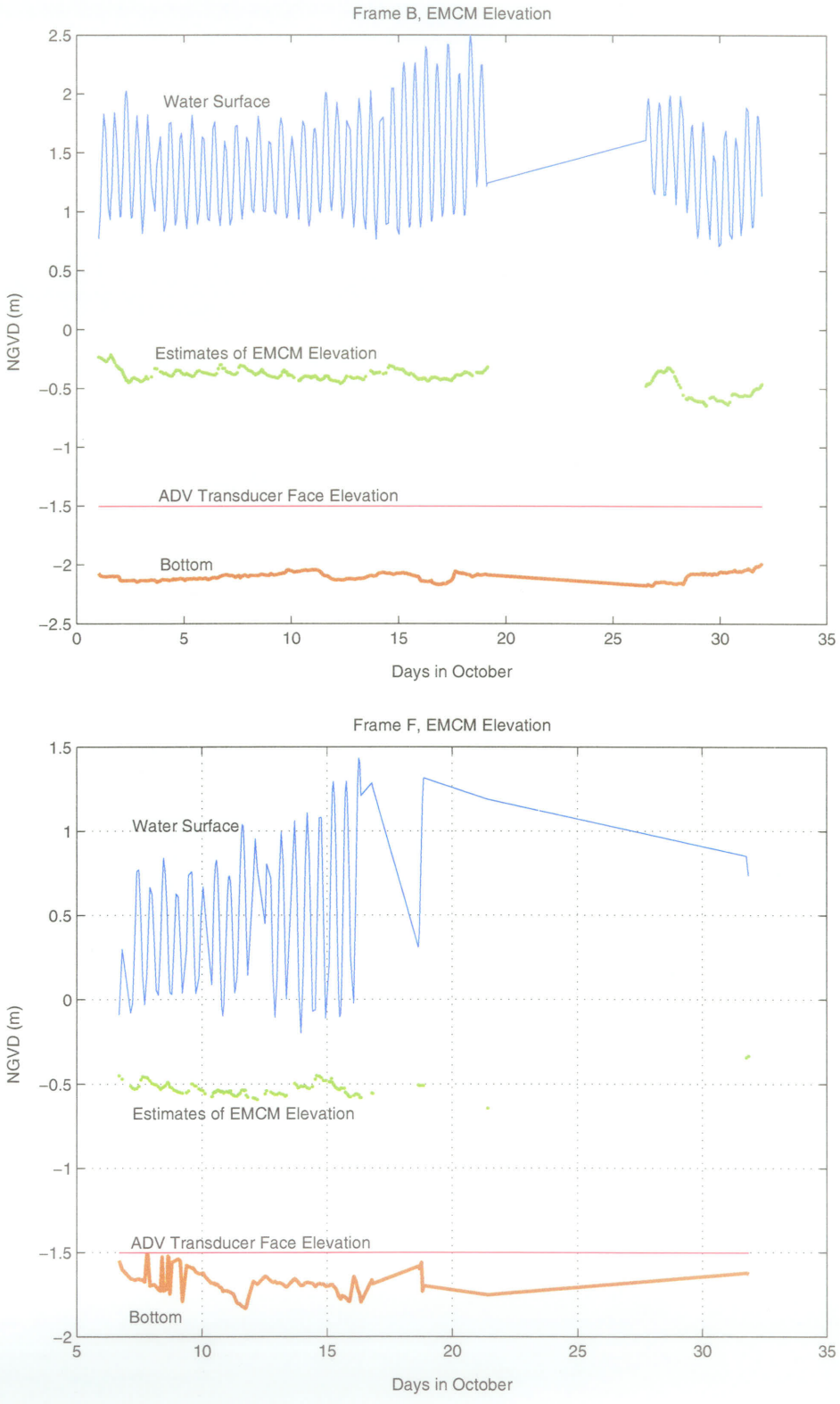

Figure 2.7. EMCM elevation estimation on frames B and F.

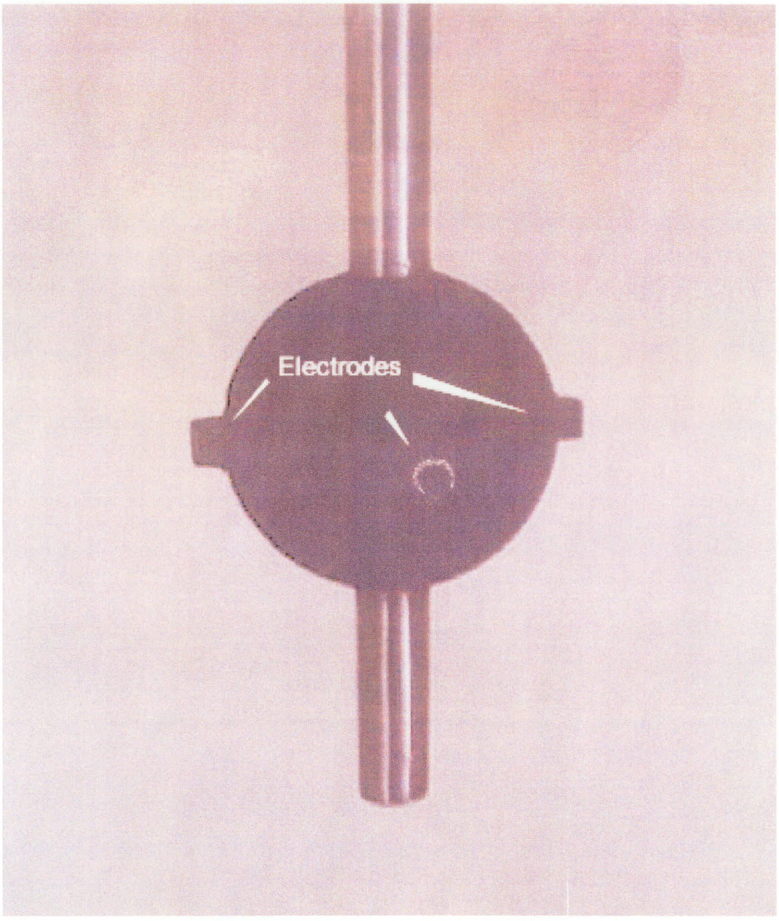

Figure 2.8. Sensing head of a Marsh McBirney electromagnetic current meter.

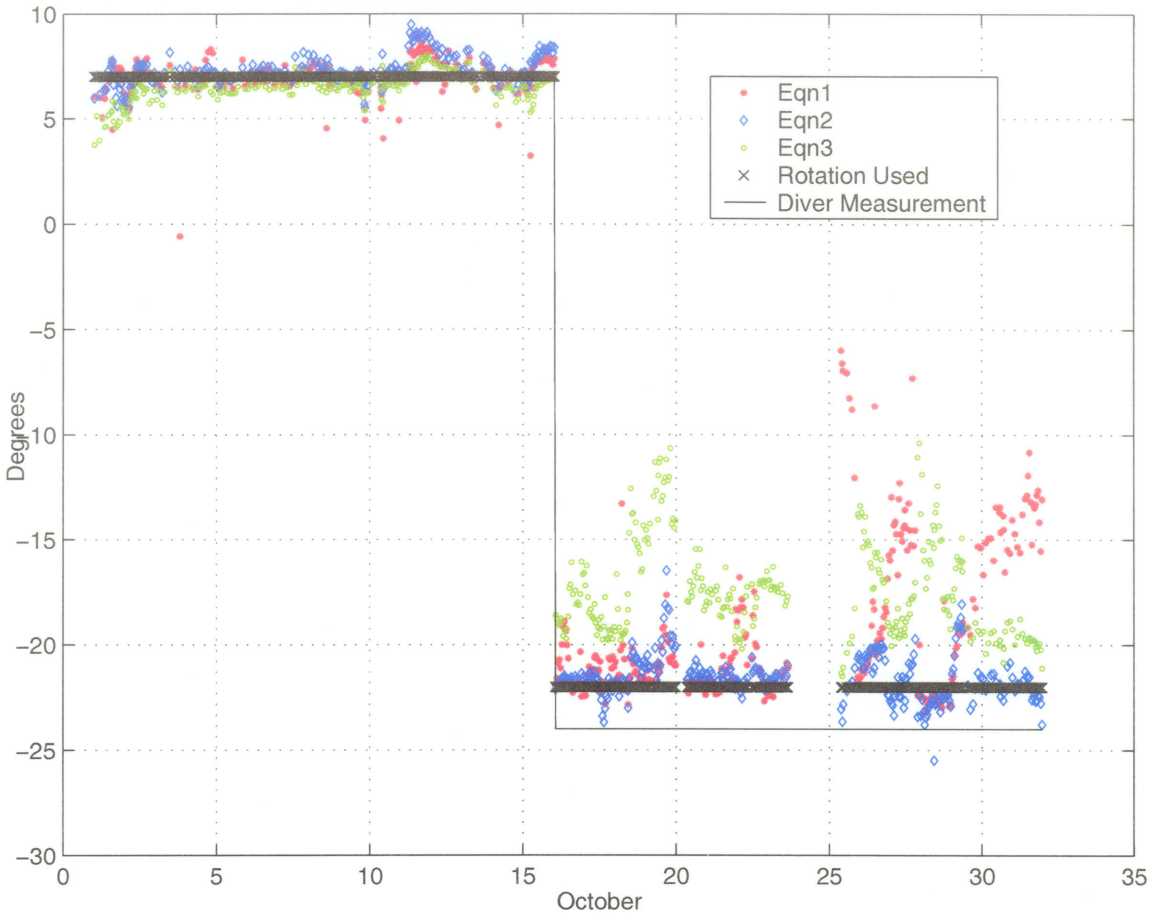

Figure 2.9. The estimated (3 equations), measured, and used rotations for the electromagnetic current meter data.

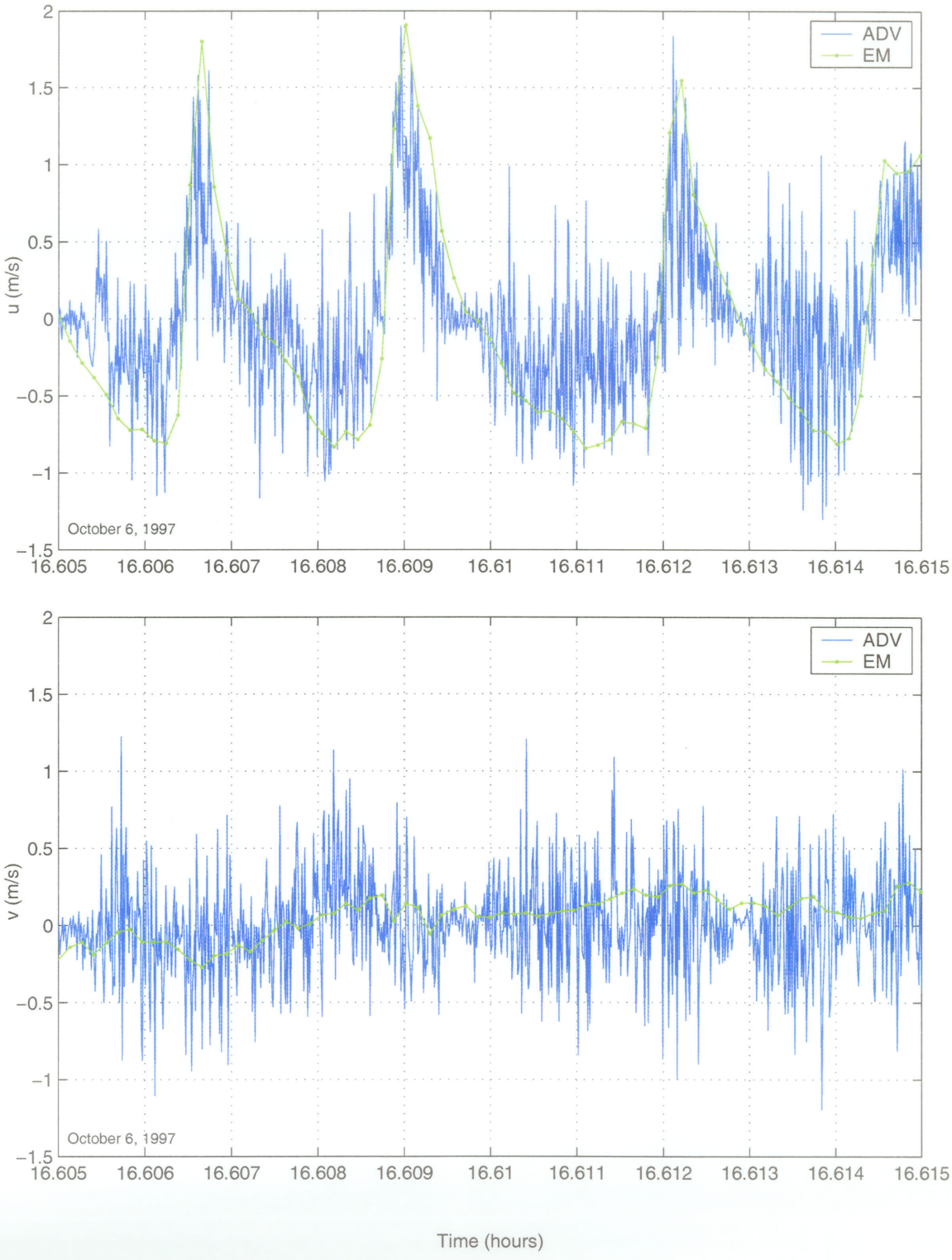

Figure 2.10. A sample of concurrent ADV and EMCM data. This ADV sample was recorded very near the bed and exhibits a large amount of high frequency fluctuation following a lower frequency carrier wave structure very similar to that of the EMCM.

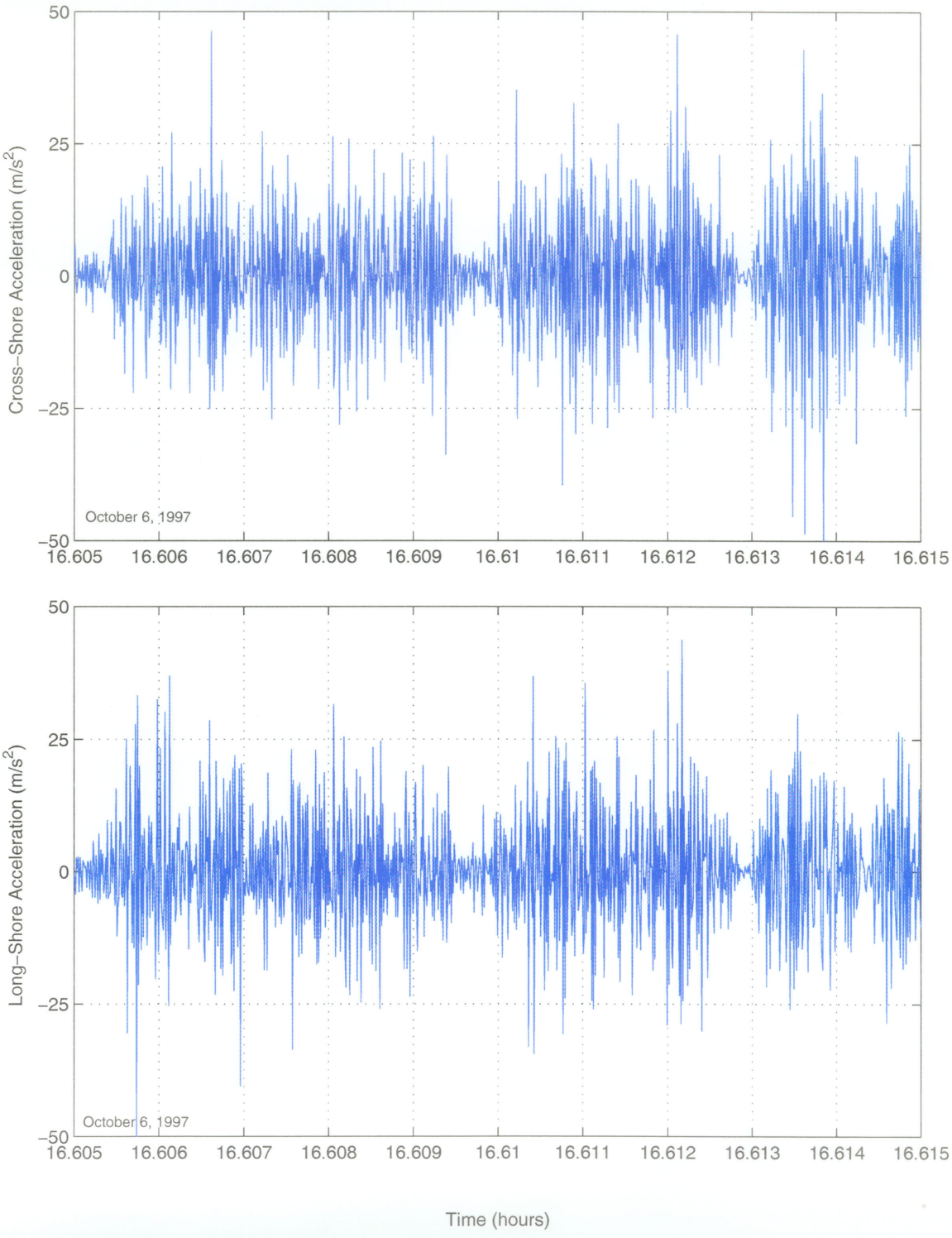

Figure 2.11. Accelerations associated with the time series shown in Figure 3.10

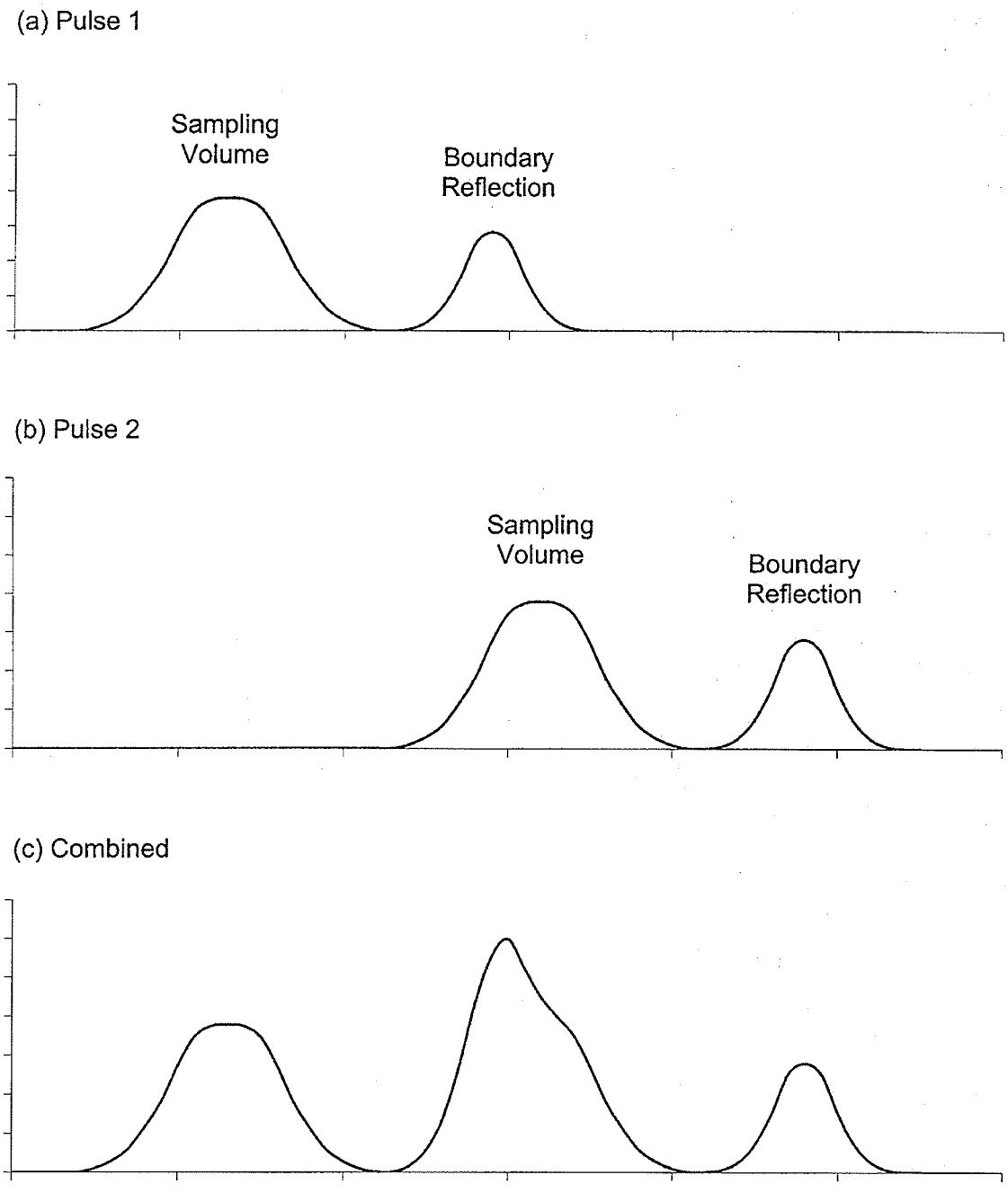

Figure 2.12. ADV Return Signal Overlap. (a) return signal from pulse 1, (b) return signal from pulse 2, (c) signal interference from the boundary layer return of pulse 1.

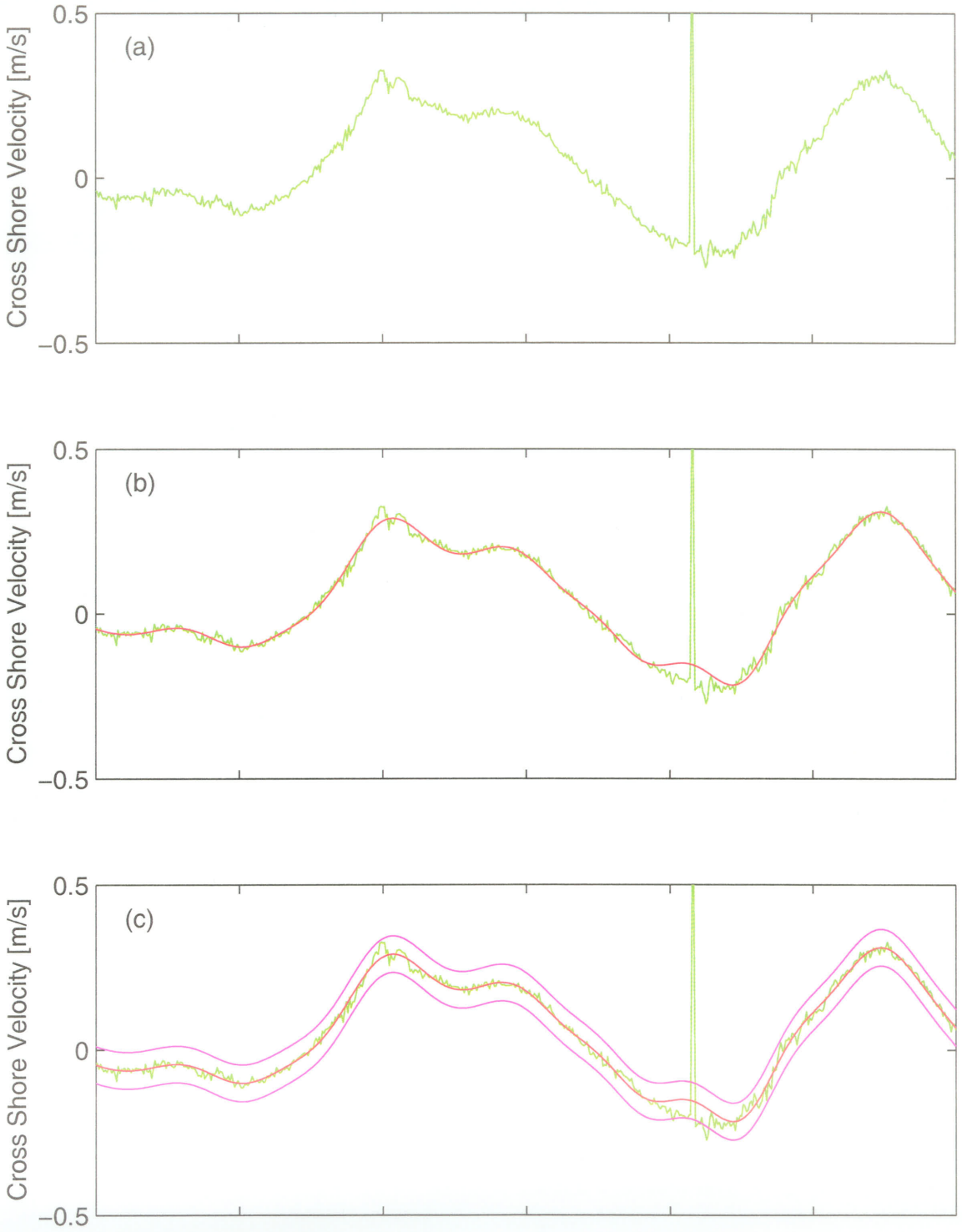

Figure 2.13, ADV Despiking Routine. (a) ADV example time series, (b) lowpass of time series, (c) window of 4.0 standard deviations of the LP-removed data,

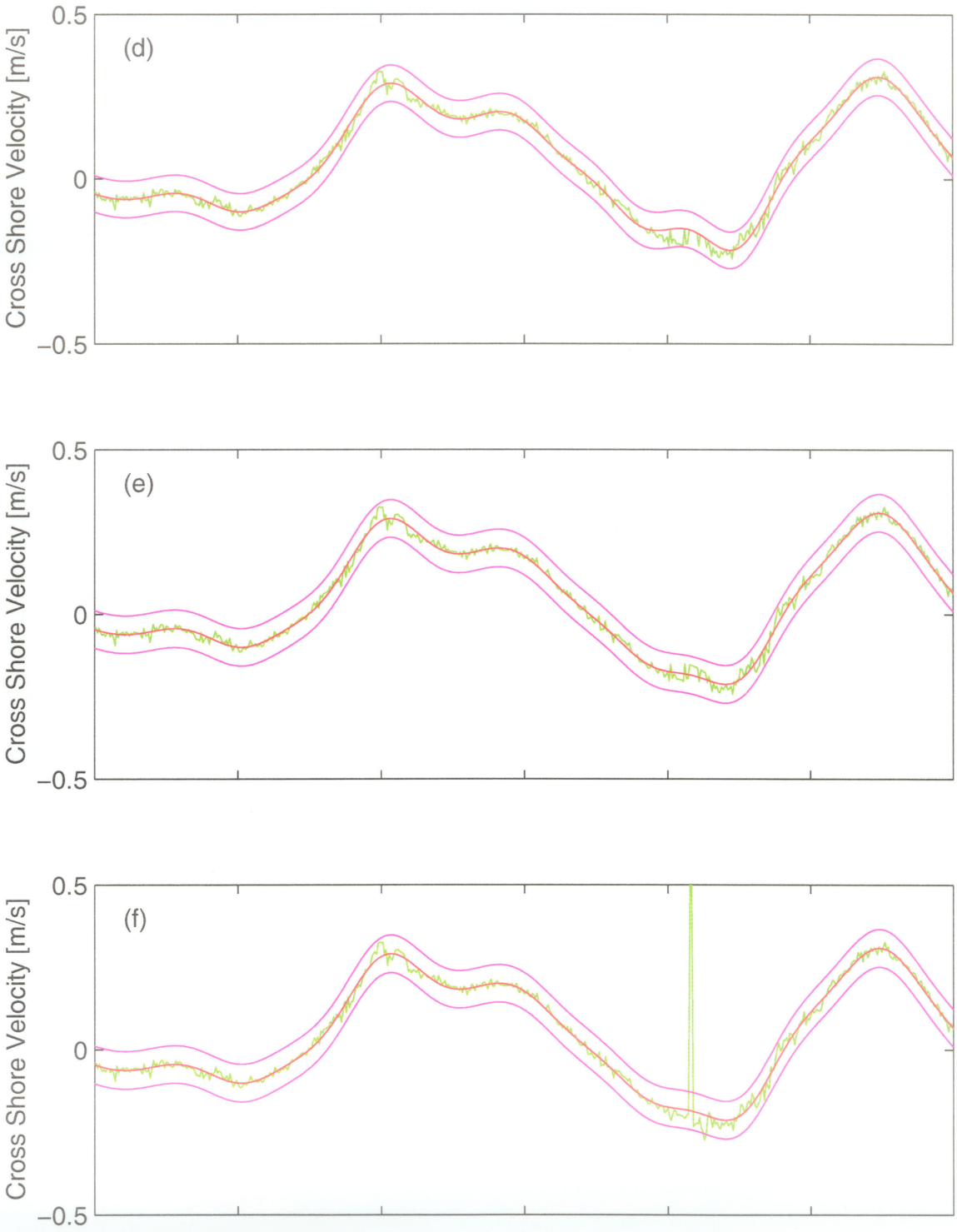

Figure 2.13, (cont'd) ADV Despiking Routine. (d) points outside of window replaced with lowpass value, (e) lowpass of new data, and (f) new window on original time series.

CHAPTER 3

Current Meter Intercomparison

3.1 Introduction

Since the introduction of the Marsh-McBirney model 512 electromagnetic current meter in the early 1970's, many coastal investigators have taken advantage of, and relied upon, their speed and presumed accuracy. Replacing the rotor-type sensors that preceded them, the Marsh-McBirney electromagnetic current meter was capable of recording large amounts of data at frequencies of up to 2 Hz. This presumed accuracy, however, has not gone unchallenged. Suggestions have been made that the AC/DC gain response could have errors of up to 40% (Aubrey et. al, 1984), although this disagreed with the vast majority of literature. These findings have since been dismissed. Another concern, however, is the flow disturbances caused by the sensor itself. It seems very likely that there could be an effect on the flow regime in its vicinity since the four probes that measure the flow are located on a relatively large sphere. This effect, if it existed, would only be expected under oscillatory flow since the instruments were calibrated using a tow tank, (i.e., not oscillatory). Although the majority of investigators believe the EMCM's to be an accurate means of measuring orbital velocities, a detailed examination of such still seems desirable. One of the objectives of this research noted in §1.2 is to examine the measurements of the EMCM on frame B as compared to the concurrent measurements made by the neighbouring ADV.

Doering and Bowen (1987) performed a comparison of skewness estimates from Marsh-McBirney Current Meters (MMCM's) and colocated pressure sensors. Using cross-spectral analysis, they found that colocated MMCM measurements were highly coherent, both inside and outside the surf zone. Consequently, normalized skewness estimates computed from the bispectrum from these current meters differed by only a few percent. Comparison of the MMCM and the pressure sensor had

similar results. They showed that the observed differences between normalized skewness estimates from the pressure sensor and the MMCI are consistent with the theoretical expectation that pressure has a nonlinear dependence on velocity. Given that their observations were consistent with theoretical expectations; Doering and Bowen (1987) asserted that MMCM was not subject to errors of the magnitude suggested by Aubrey et. al. (1984).

In order to address the question of flow disturbances from the spherical probe, Guza and Thornton (1980) designed and built an open-framed electromagnetic current meter in order to perform an intercomparison between it and the Marsh McBirney model. They evaluated the correlation between hourly records and noticed a constant bias between the measured mean flows that were roughly equal to the estimated accuracy of the sensor offset calibrations. They noticed that the root-mean-square deviations from this bias were less than 2.0 cm/s, and were contributed to by errors in both gain calibration and sensor orientation. In addition to comparisons of measured oscillatory currents, they compared the measured currents to those estimated using linear theory applied to colocated pressure sensor measurements. Time series of U^T_{rms}, (the rms total oscillatory flow for a 1-hour record), were generated and were found to be very highly correlated. They examined fluctuations of U^T_{rms} ratio about the mean ratio and indicated these would be indicative of flow meter gain distortions probably associated with variations in the hydrodynamic environment. Their examination of the ratio of U^T_{rms} from both deployments suggested that their open-framed sensor overresponded, relative to the spherical probe, at low total speeds (mean + U^T_{rms}), and underresponded at higher total speeds. Relative to pressure data and linear theory, both flow meter types overresponded at low speeds and underresponded at high total speeds. They were unable to determine if these apparent gain distortions of the flow meters relative to pressure are associated with errors in the linear theory or with the response characteristics of the flow meters. Cross-spectra between all sensors (including the pressure) show high coherence and phase differences of a few degrees, and they suggest that the response of both flow meters is only slightly frequency dependent. They also discussed various practical difficulties in accurately measuring the flow-induced micro-volt potentials in an electromagnetically noisy environment, with potentially interfering current meters. From all of these findings, these authors concluded that both instruments, (i.e. open frame and MMCM), performed favorably for measuring orbital velocities.

Although it is acknowledged that for the present study there will be some differences in the flow behavior at each instrument location, they are sufficiently close to one another that the time series should be quite similar. As discussed in Chapter 2, those ADV records that were thought to have a boundary effect were not used in this comparison because one would expect a difference between them and another record measured higher in the water column.

3.2 Comparative Parameters and Methodology

The purpose of this intercomparison is to gain insight into the accuracy of both the EMCM and the ADV measurements as they pertain to nearshore hydrodynamics. For this reason, it seems necessary to include an examination of higher order moments in the comparison. Differences in the original time series will be increasingly amplified through higher order analysis.

In order to compare the time series of each of the two instruments, several parameters were chosen. The most obvious, of course, were linear regression and correlation between the two time series. The first four statistical moments: mean, variance, skewness and kurtosis, defined as

$$\bar{x} = \frac{\sum_{i=1}^{n} x_n}{n}, \tag{3.1}$$

$$s^2 = \frac{\sum_{i=1}^{n} (x_i - \bar{x})^2}{n-1}, \tag{3.2}$$

$$S = \frac{\sum_{i=1}^{n} (x_i - \bar{x})^3}{(s^2)^{1.5}(n-1)}, \text{ and} \tag{3.3}$$

$$K = \frac{\sum_{i=1}^{n} (x_i - \bar{x})^4}{(s^2)^2(n-1)}, \tag{3.4}$$

respectively, were used to examine the shape of each of the wave time series.

Power spectra were computed for each instrument, for each record and compared using correlation.

Cross-spectral analysis is performed to examine the coherence and phase spectra for the ADV and EMCM records. The coherence provides a measure of the correlation between the two measurements at each frequency and the phase spectrum indicates the phase difference between the two records at each frequency. For this analysis, the records were broken into 20 blocks of data; the coherence and phase were computed and averaged to obtain 40 degrees of freedom. Transforms were done using a Hamming window with no overlap. The biased upper limit on zero coherence (95% confidence limit) is estimated using

$$C^2 = 1 - \alpha^{\frac{2}{d.o.f.-2}}. \tag{3.5}$$

The integrated variance of the incoherent signal between the two records over the incident wave frequency to 1 Hz, can be represented by

$$\varepsilon^2 = \int_{f=0}^{f=1} \left(1-\gamma^2\right) \left(P_{EMCM} P_{ADV}\right)^{1/2} df, \tag{3.6}$$

where ε is the integrated deviation between the two instrument recordings, γ is the coherence and P is the energy density spectrum.

3.3 Observations

The objective of this intercomparison was to examine the agreement between EMCM and ADV data. In order to ensure an unbiased comparison, it was decided to limit the dataset to those that contain ADV data not influenced by the bottom. In other words, this study will not include any record that is sufficiently close to the bottom that boundary layer effects or other near-bottom disturbances may be significantly affecting the velocities. This is a reasonable restriction since we would expect the records to have differences if the bottom has a larger effect on one sensor than on the other. Therefore, to be conservative, a minimum sampling volume to boundary distance of 20 cm was chosen. For this reason, and because the ADV sampling volume on Frame F was typically very close to the bottom, only Frame B was used for the intercomparison.

Figure 3.1 illustrates a portion of a typical cross and long-shore time series as recorded by the EMCM and ADV instrumentation, post-processed in the manner described in Chapter 2. The agreement between these time series is very good. In this example, beginning at 05:30 on October 11, 1997, the EMCM and ADV instruments were positioned 55 and 165 cm from the bottom, respectively. With the ADV being sufficiently away from the bottom, boundary effects should be negligible.

In order to compare ADV and EMCM time series, the ADV records were resampled from 25 Hz to 2 Hz. This was done by applying an anti-aliasing (lowpass) FIR filter to the record during the resampling process. Figure 3.2 is a segment of the cross-shore time series of a typical record, illustrating the resampled time-series.

Figure 3.3 is a one-to-one plot of EM data versus the resampled ADV data for both cross and long-shore velocities. As mentioned, linear regression and correlation between each pair of records were the first steps in the intercomparison. For this example file, (05:30, October 11, 1997), the correlations for the cross shore and long shore velocities are 0.981 and 0.907, respectively. Although this shows the two records are very highly correlated, (keeping in mind that long-shore structure is much more dependent on vertical position than is the cross-shore), correlation does not reveal anything as to agreement in the value of the data, only agreement in their shape. Also shown on Figure 3.3 is the equation resulting from the linear regression. The slopes of these best-fit lines indicate that the record magnitudes also compare very well as they are very close to unity. As was the case with the majority of the records used for this intercomparison, this record comprised 2800 points.

The first four moments computed for this record are given in the following table.

TABLE 3.1 – VALUES OF THE FIRST FOUR MOMENTS (05:30, OCT. 11, 97)

	ADV Cross-shore	EMCM Cross-shore	ADV Long-shore	EMCM Long-shore
$\overline{x}$	0.020	0.016	0.036	0.023
s^2	0.089	0.088	0.008	0.007
S	0.675	0.750	-0.054	-0.053
K	3.291	3.667	2.974	3.379

Although the mean velocities measured by these instruments are quite different, the variance and skewness estimates are quite similar. The kurtosis estimates associated with the wave peakiness in the long-shore direction are subject to somewhat larger error.

Figures 3.4 and 3.5 illustrate a second time series, beginning at 19:30 on October 4, 1997. The time series in this example exhibits one of the worst agreements between ADV and EMCM data used for the intercomparison. In this example, the correlations are 0.916 and 0.556, respectively. The slopes of the best fit lines are 0.922 and 0.738, respectively. It is apparent that the long-shore velocities do not agree very well in this example.

The first four moments computed from this record, are shown in Table 3.2.

TABLE 3.2 – VALUES OF THE FIRST FOUR MOMENTS (19:30, OCT. 4, 97)

	ADV Cross-shore	EMCM Cross-shore	ADV Long-shore	EMCM Long-shore
$\overline{x}$	-0.009	-0.012	-0.122	-0.131
s^2	0.019	0.021	0.004	0.004
S	0.124	0.248	0.078	0.033
K	3.025	3.128	2.831	3.107

In general, there is good agreement between the data from these two instruments, except for the skewness estimates.

To carry these comparisons forward, throughout all applicable records, the comparative parameters were calculated for each record and examined in bulk. Figures 3.6 through 3.9 show the comparison of the mean flow, variance, skewness and kurtosis, respectively for all records used in the intercomparison data set. The two records considered previously are indicated in each figure with the symbols □ and O for the October 4 and October 11 records, respectively.

Figure 3.10 illustrates the correlation coefficient for each record, for both the cross and long shore velocities. Again, the two example records are indicated in these plots. It is apparent that the cross shore measurements are very strongly correlated with r^2 values greater than 0.9. The long-shore

records are not as strongly correlated, with r^2 values as low as 0.55 but typically above 0.80. As mentioned earlier, however, the long-shore records will be more depth dependent and correlations as great as those for the cross-shore records should not be expected.

In order to compare the power spectra computed from the data obtained by each sensor, correlations were computed. These correlations, illustrated in Figure 3.11, are very strong, even for the long-shore records.

Cross-spectral analysis was performed to further compare the spectra from each record. The coherence and phase spectra for the first example time series, (05:30, October 11, 1997), are shown in Figure 3.12. Also shown in the Figure 3.12 is the 95% confidence level for non-zero coherence; the cross and long-shore spectra are coherent well beyond 0.5 Hz. When compared to the power spectra for these same records, (Figure 3.13), it is apparent that there is very little energy beyond 0.5 Hz. The incoherence found beyond 0.5 Hz is therefore due largely to the relatively high noise/signal ratio. The coherence, phase and power spectra for the second example time series are shown in Figures 3.14 and 3.15, respectively. Once again, the records are found to be coherent out to 0.5 Hz, after which the frequencies have very little associated energy, resulting in a high noise/signal ratio.

As discussed earlier in this chapter, the integrated variance of the incoherent signal between the two records can be represented by (3.6). This parameter provides a means of comparing the coherence for all records in the intercomparison data set. The ε values for the cross and long-shore records can be seen in Figures 3.16 (a) & 3.17 (a), respectively. Integrated variance values of up to approximately 11 cm/s can be observed. When normalized by the record standard deviation, integrated variances (of the incoherent signals) as high as 25% of the record standard deviation can be observed in the cross-shore with values of nearly 60% in the long-shore direction.

Another method used to compare the coherence spectra in bulk was to examine the frequency at which each spectra fell below a coherence value of 0.8. This is not to say that values lower than this are not coherent, it simply provides a means to roughly examine the shape of the coherence spectra. The results of this comparison, for the cross-shore and long-shore are shown in Figure 3.18 (a) and (b), respectively. It is evident that no record exhibits a coherence lower than 0.8 at frequencies less than 0.2 Hz. Figure 3.19 provides a similar comparison, indicating the frequency at which the coherence falls below the 95% Confidence level. In all cases, the two signals are coherent beyond 0.4

Hz and 0.3 Hz for the cross and long-shore components, and in most cases it is beyond 0.5 Hz. More specifically, 93% of the cross-shore records and 92% of the long-shore records are coherent beyond 0.5 Hz.

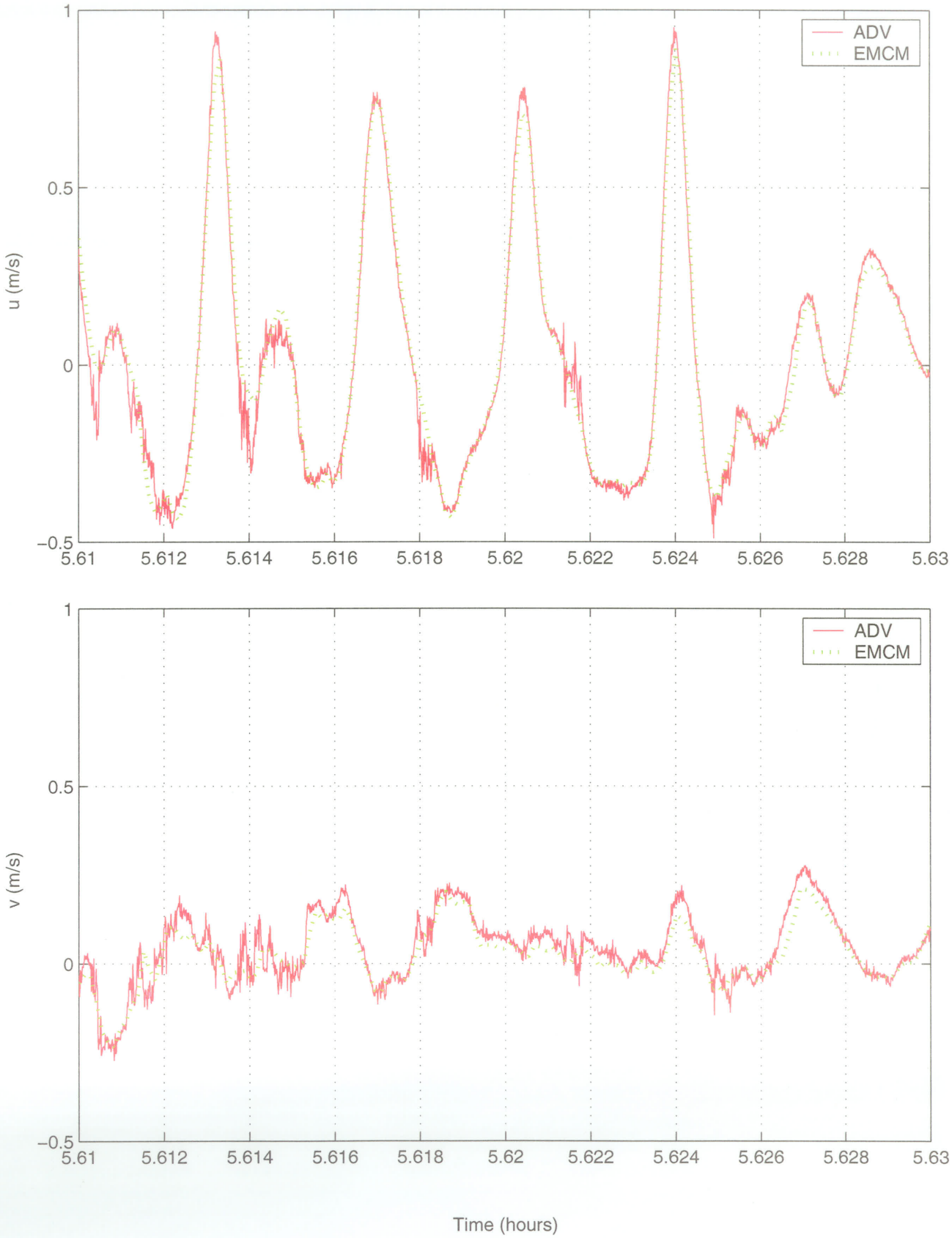

Figure 3.1. EMCM and ADV time series for 05:30 on October 11, 1997.

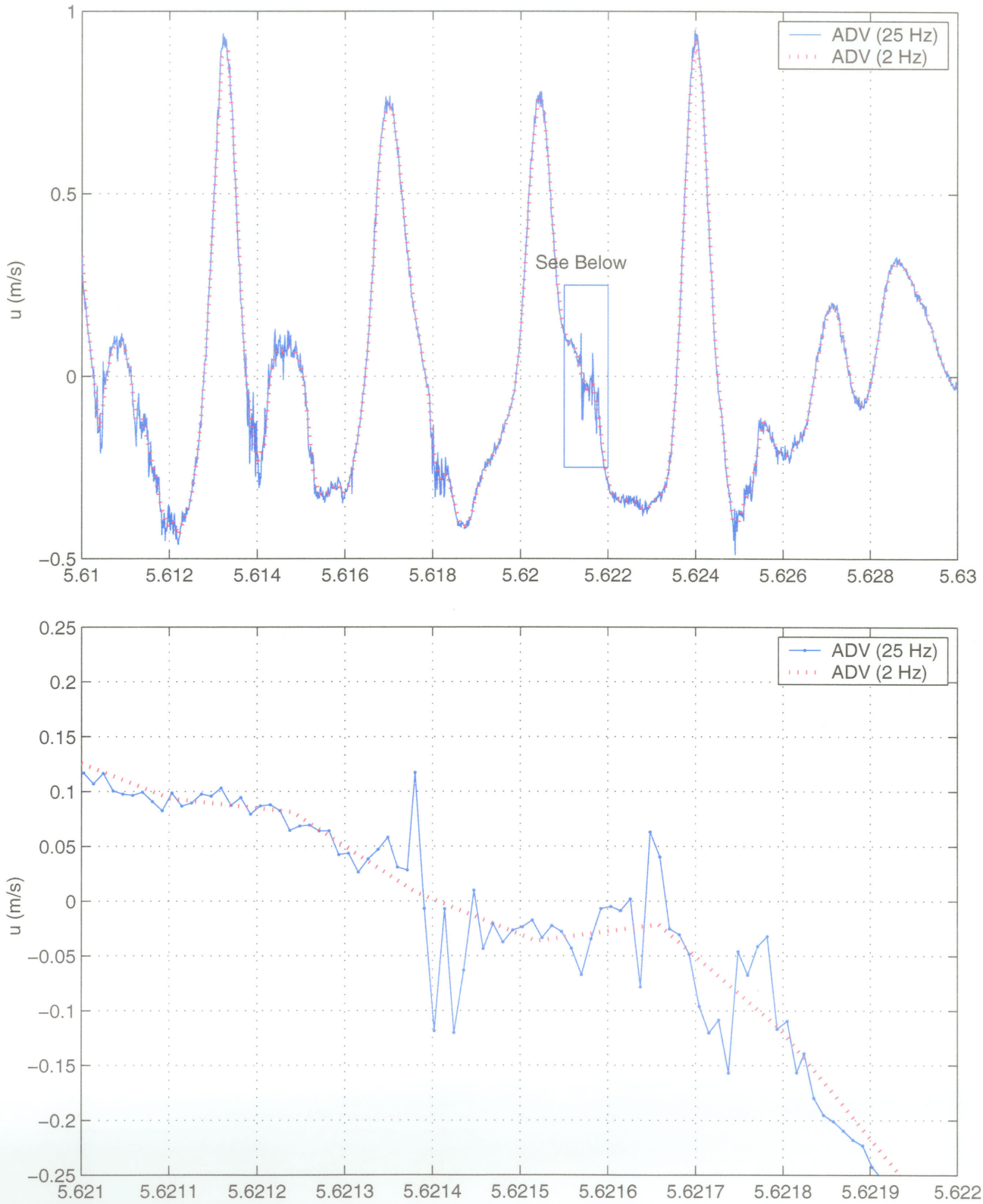

Figure 3.2. Cross-Shore time series showing the comparison between the original 25 Hz data and the resampled ADV data.

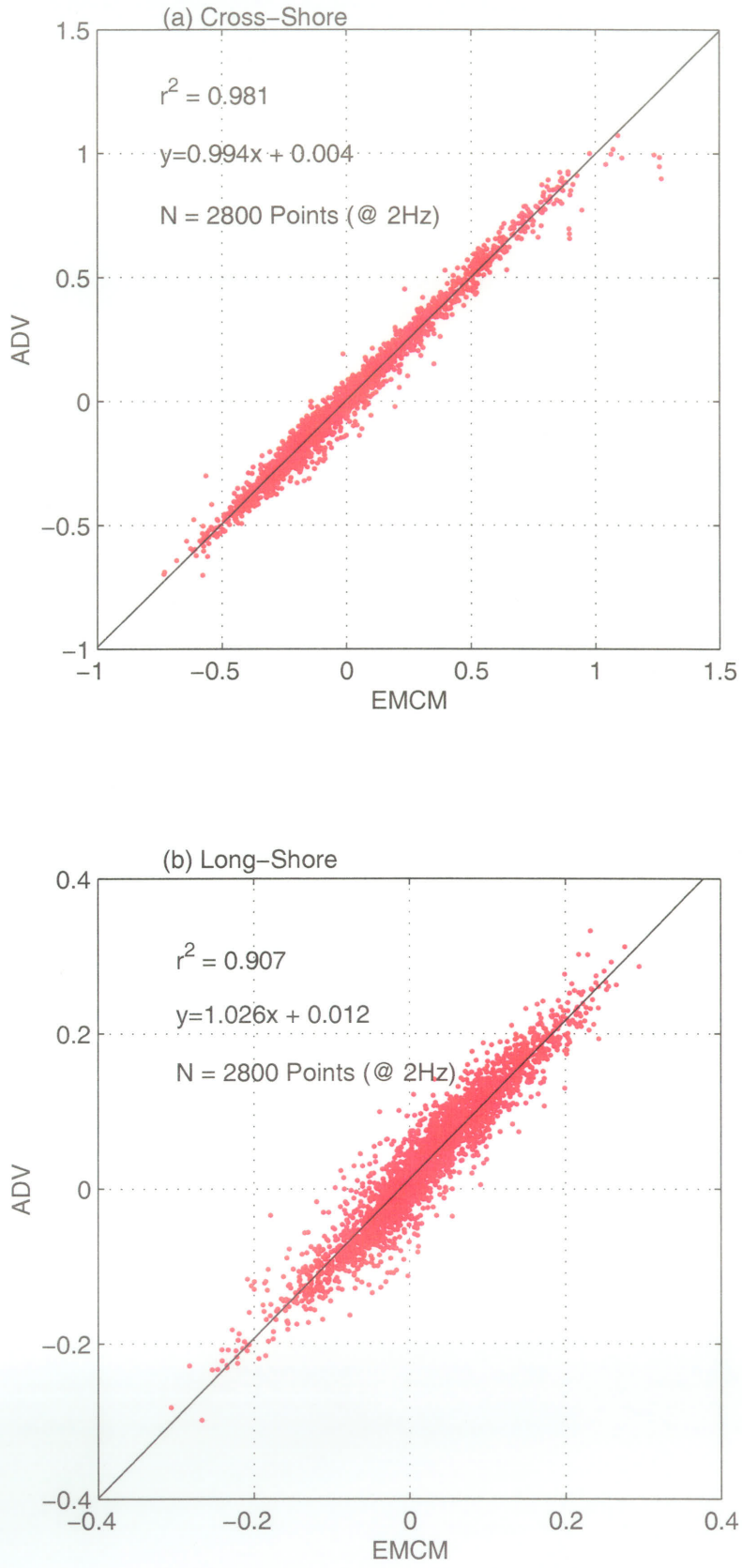

Figure 3.3. ADV vs.EMCM data for 05:30 on October 11, 1997.

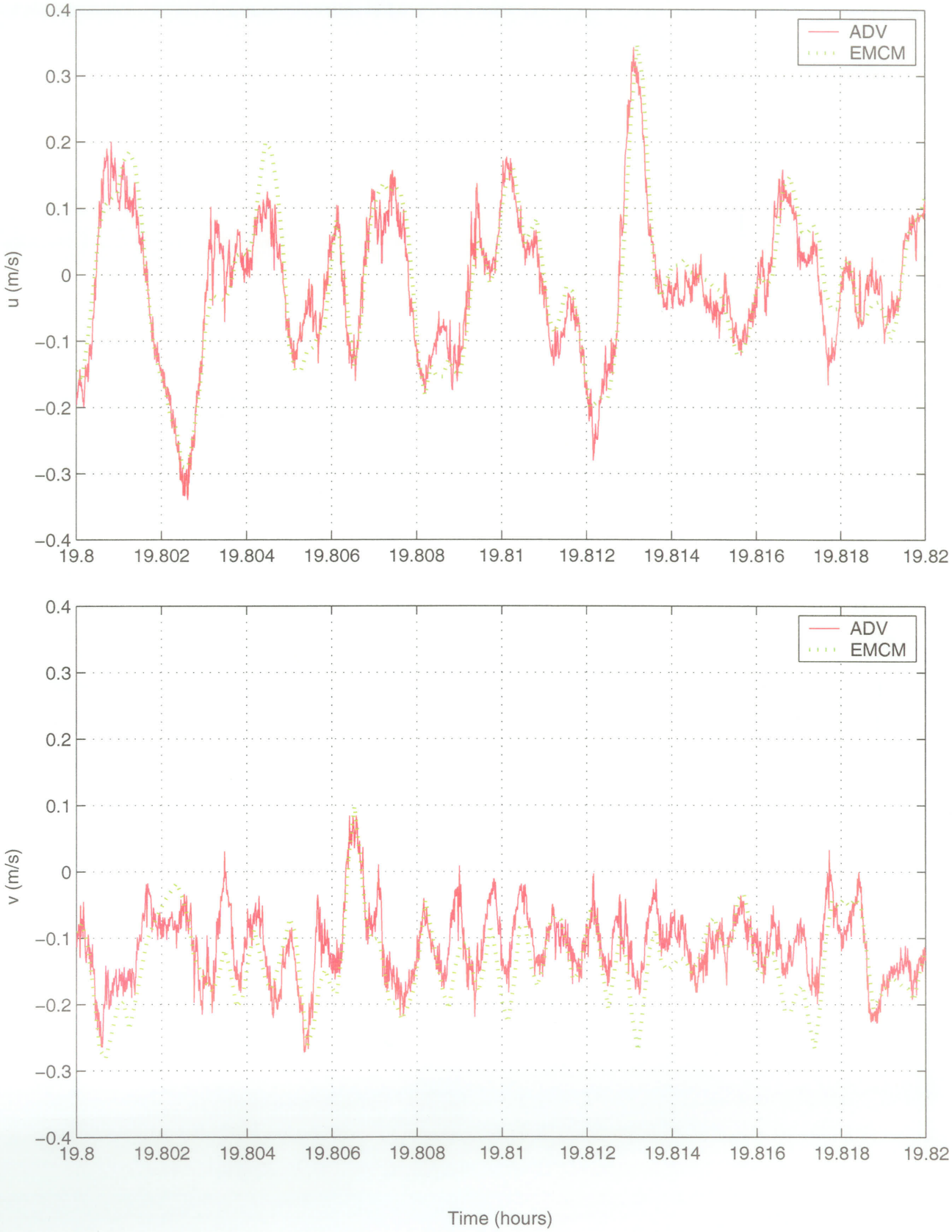

Figure 3.4. EMCM and ADV data from 19:30 on October 4, 1997.

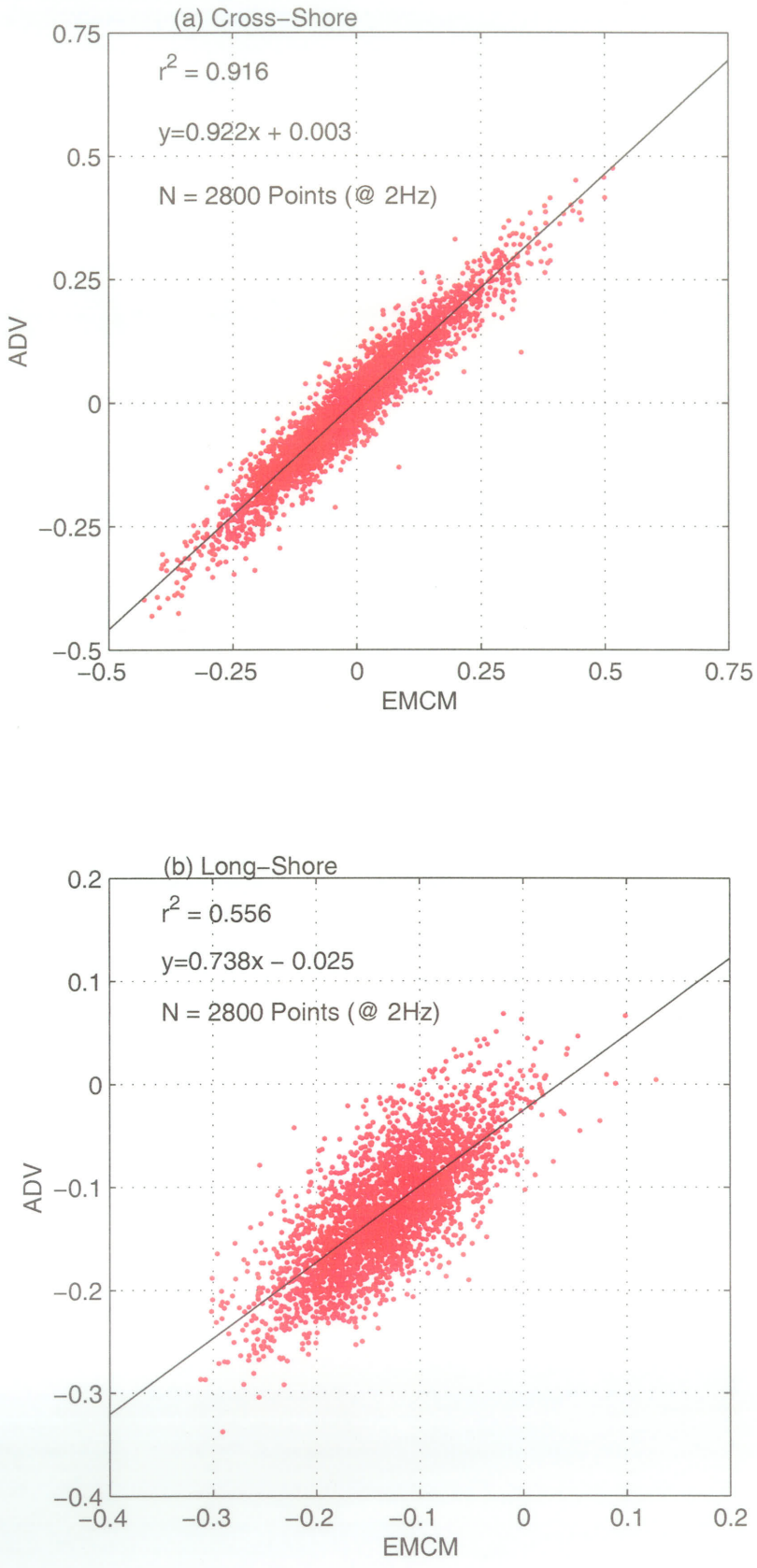

Figure 3.5. ADV vs.EMCM data for 19:30 on October 4, 1997.

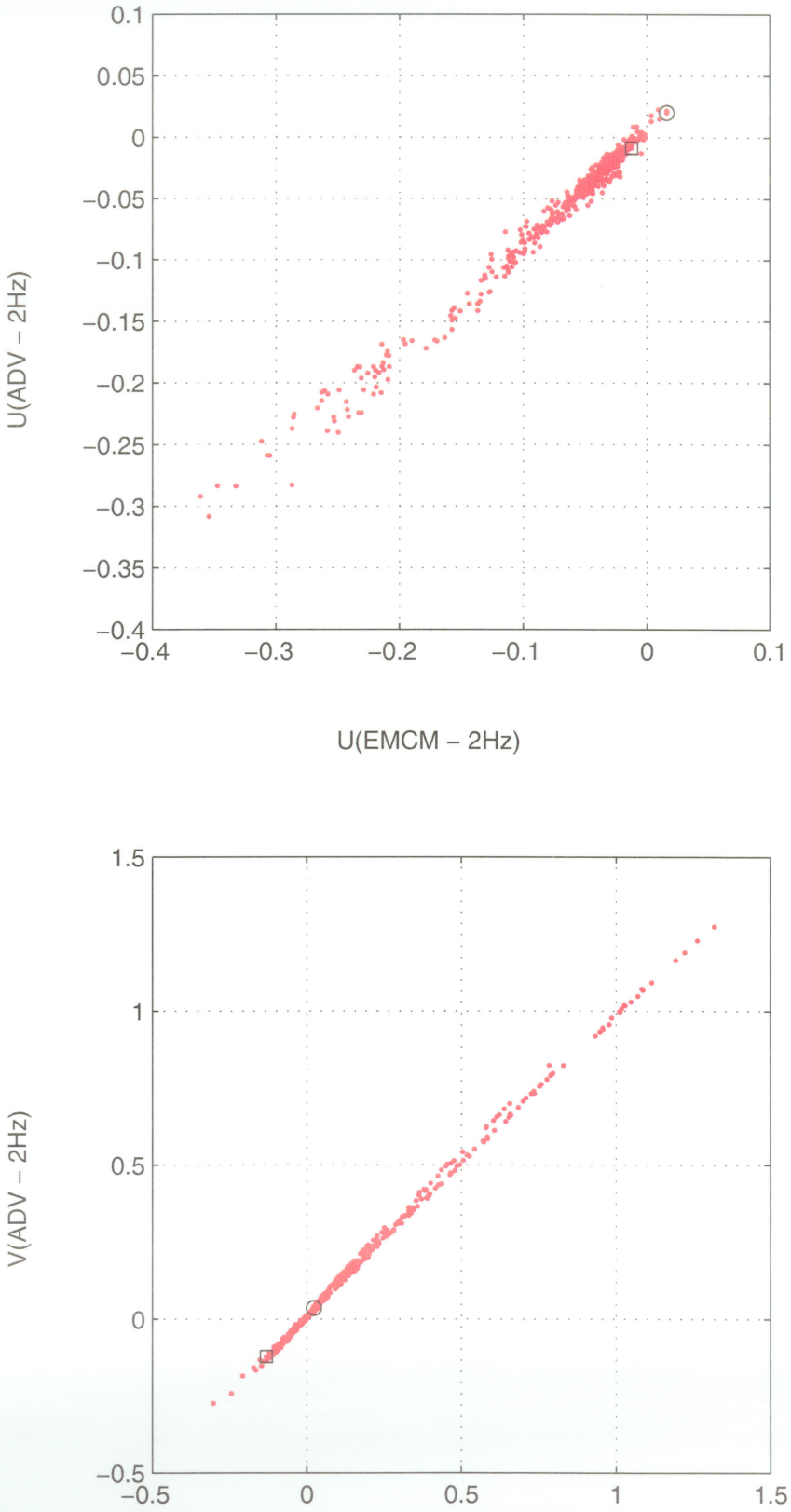

Figure 3.6. Comparison of mean flow estimates between ADV and EMCM.

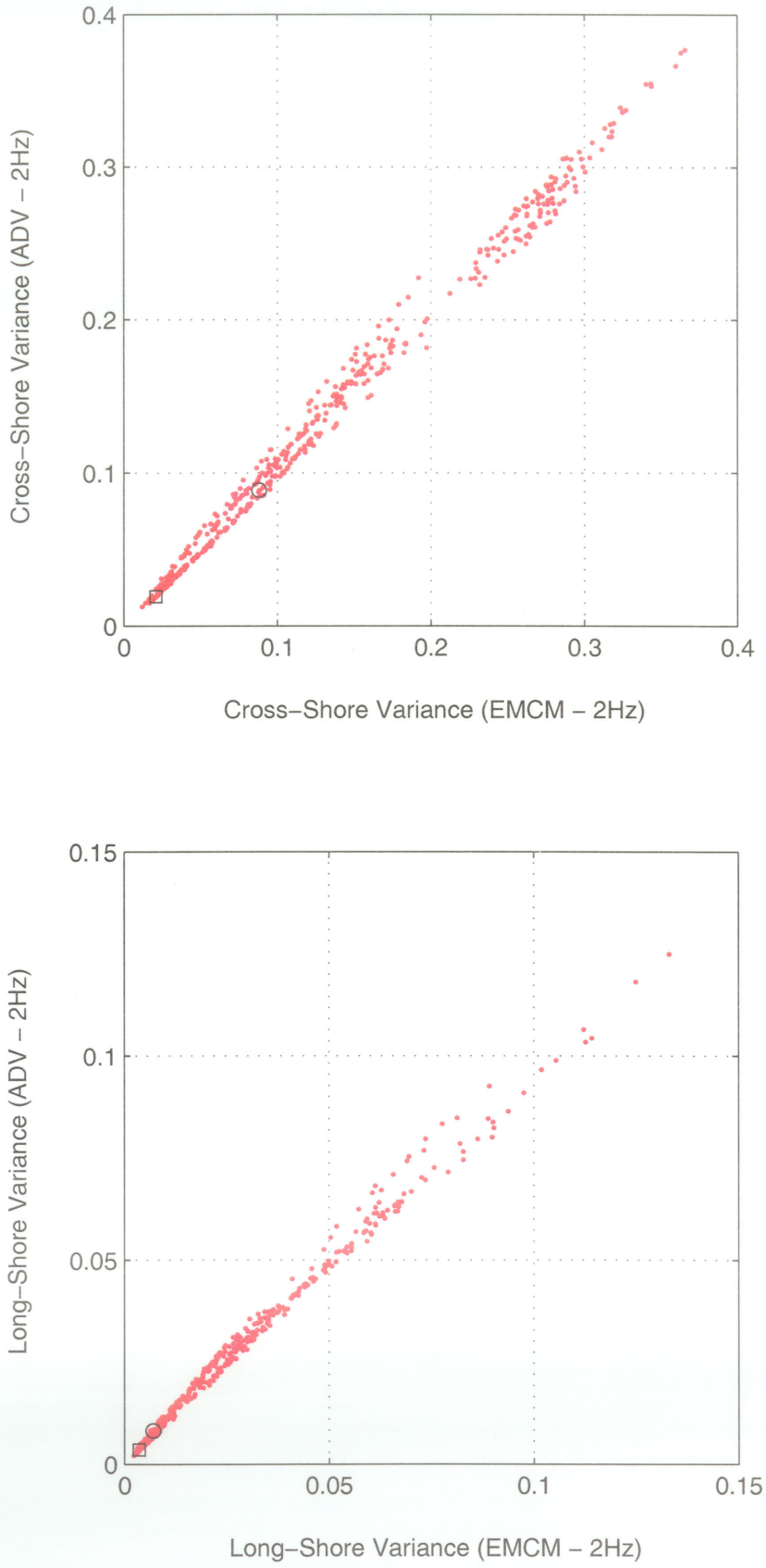

Figure 3.7. Comparison of variance estimates between ADV and EMCM.

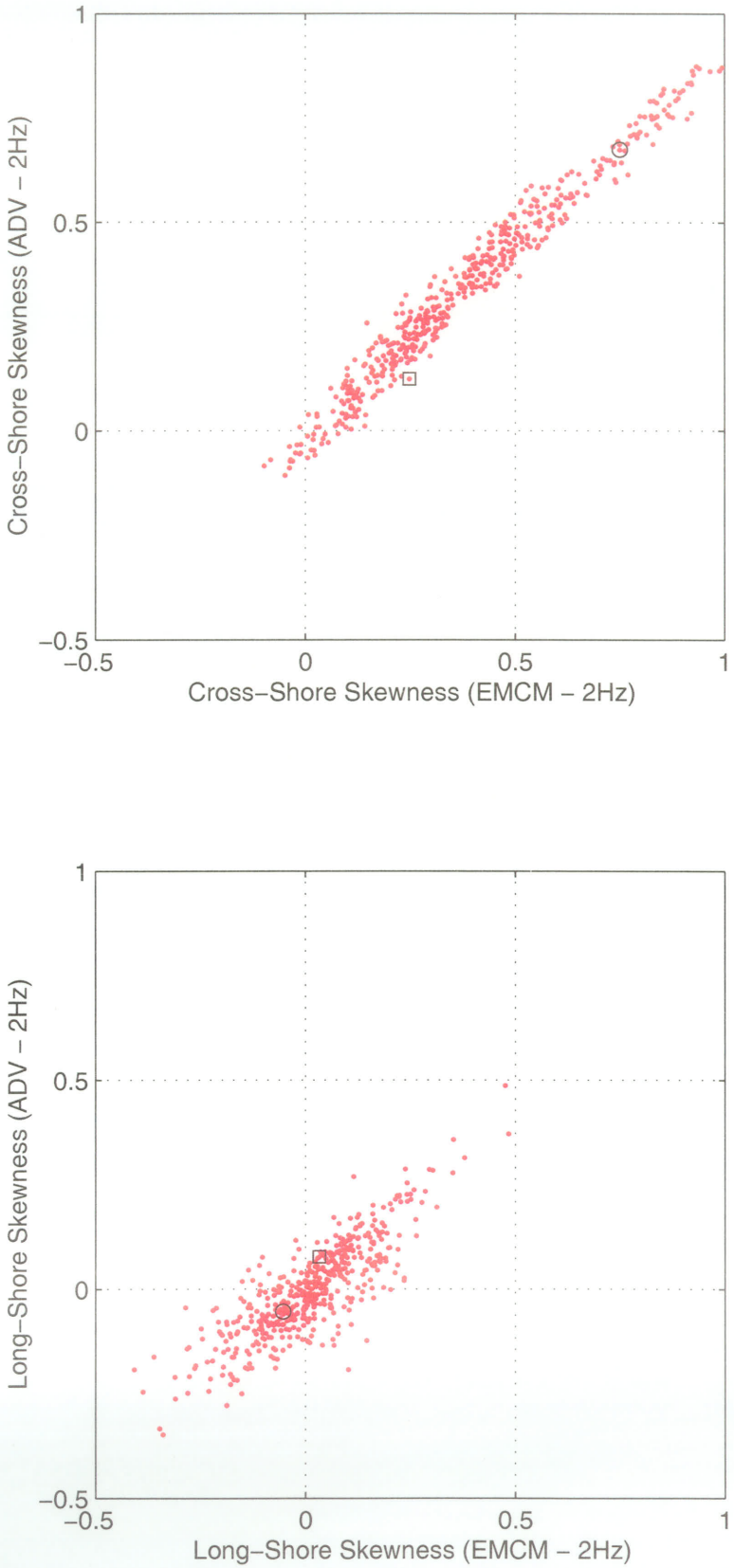

Figure 3.8. Comparison of skewness estimates between ADV and EMCM.

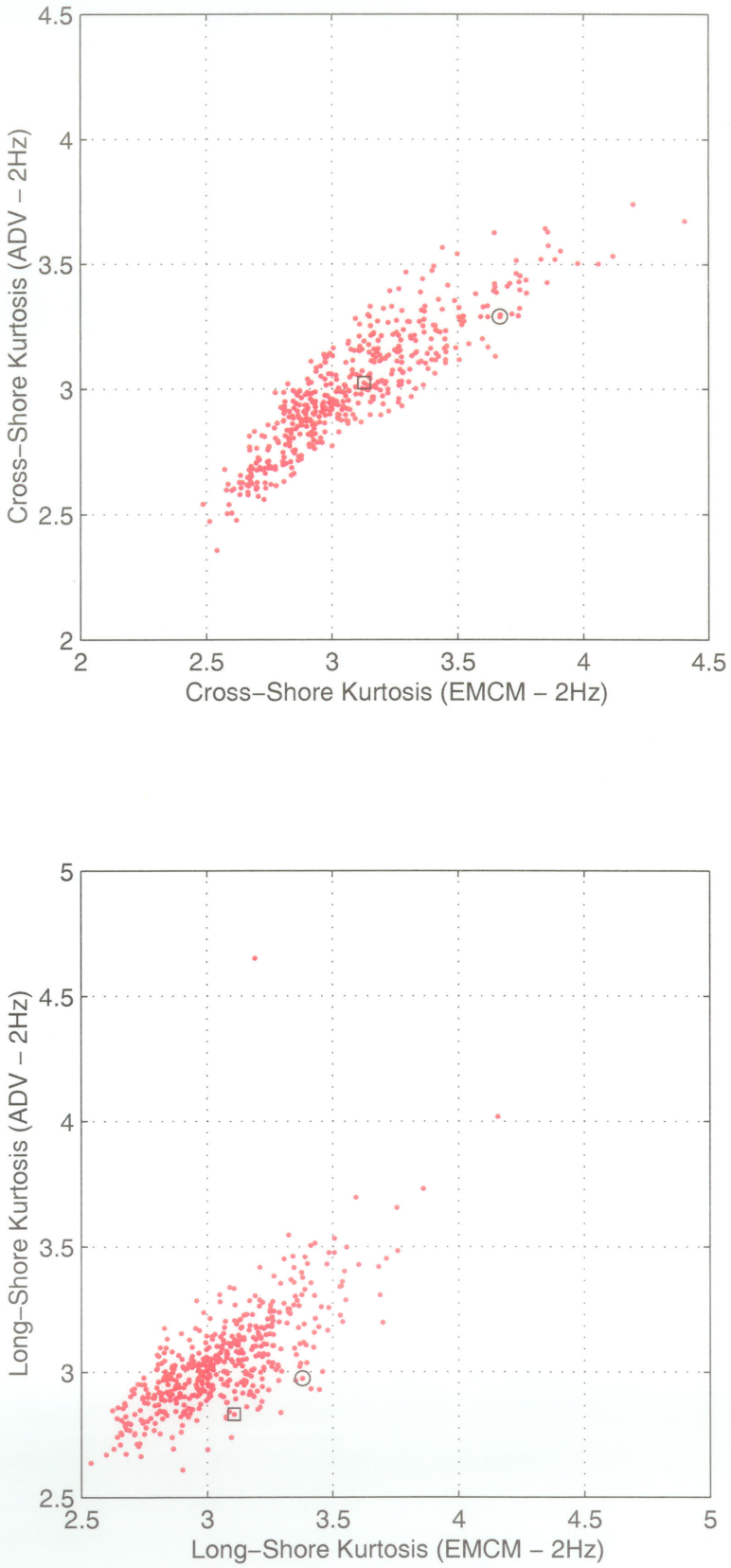

Figure 3.9. Comparison of kurtosis estimates between ADV and EMCM.

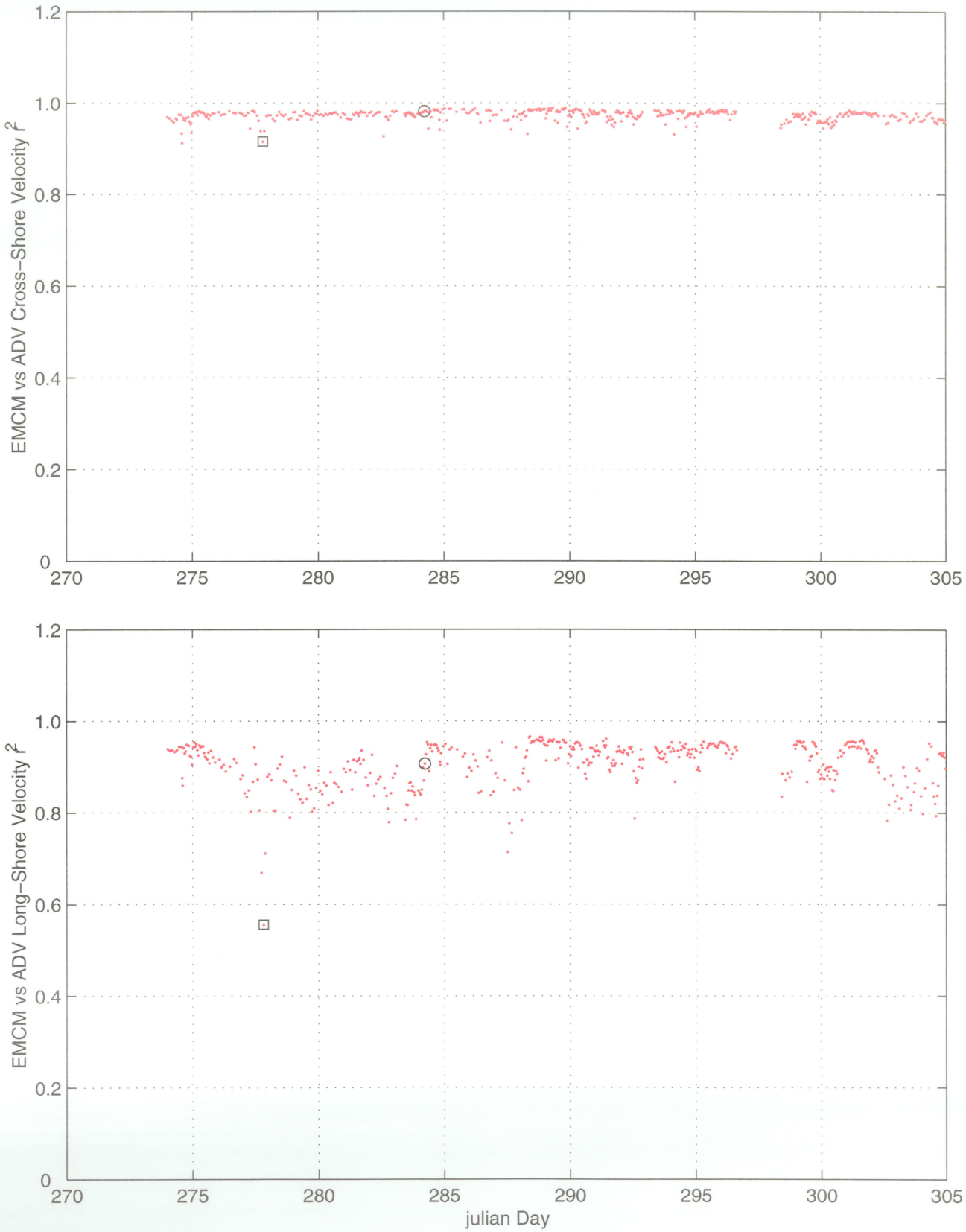

Figure 3.10. Velocity correlation coefficients for all records in the intercomparison datset.

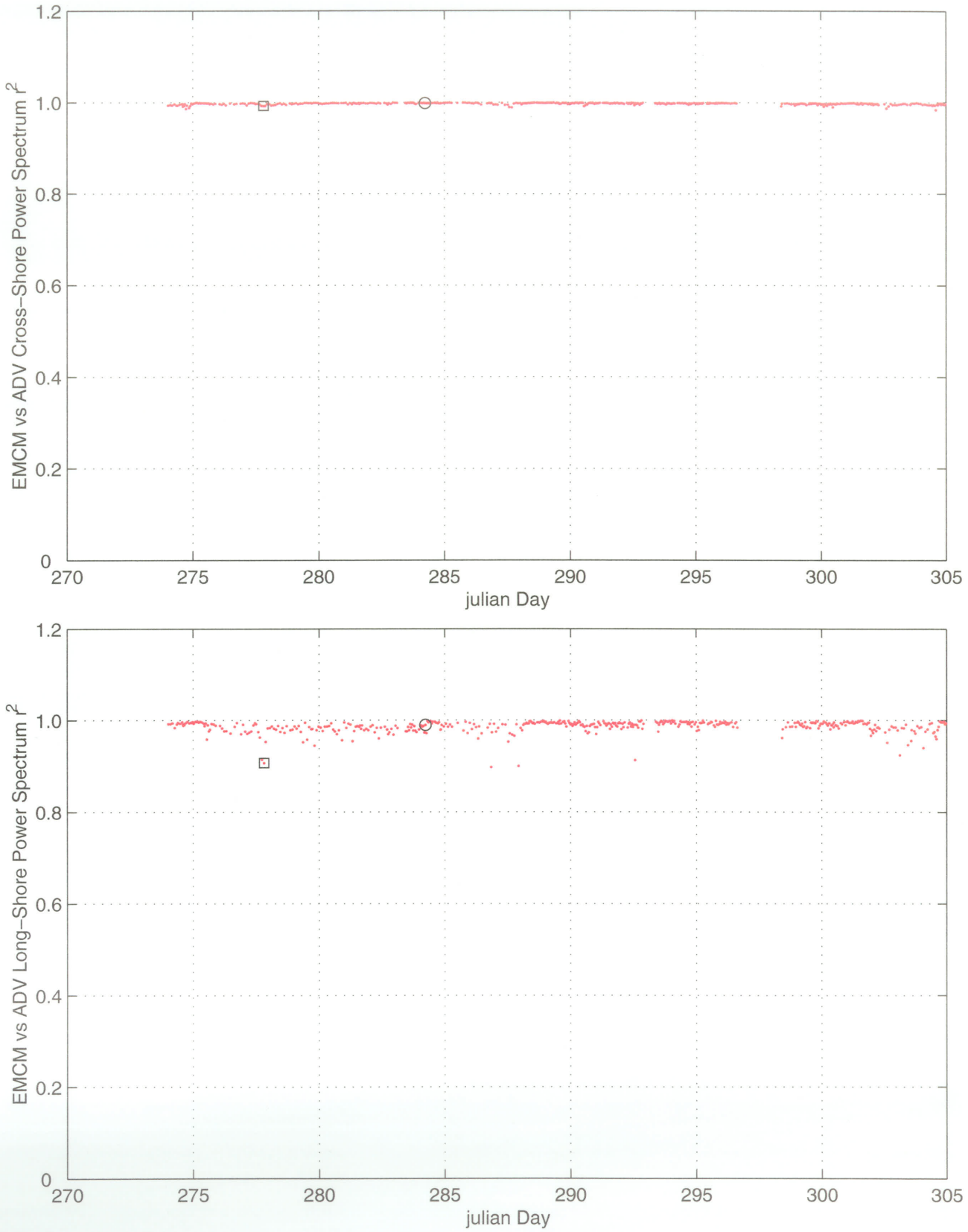

Figure 3.11. Power spectrum correlations for all records in the intercomparison dataset.

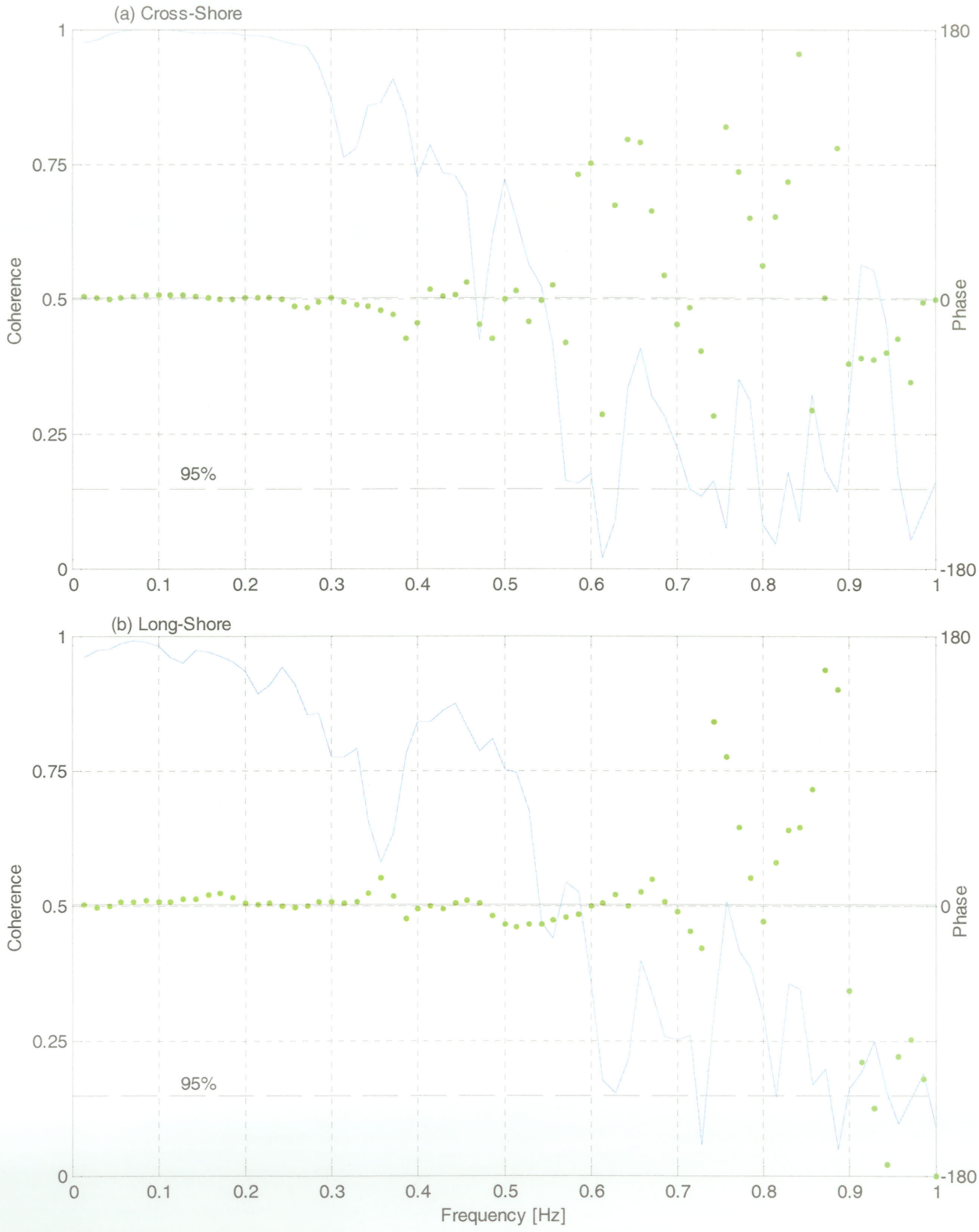

Figure 3.12. Coherence and phase spectra for 05:30, October 11, 1997.

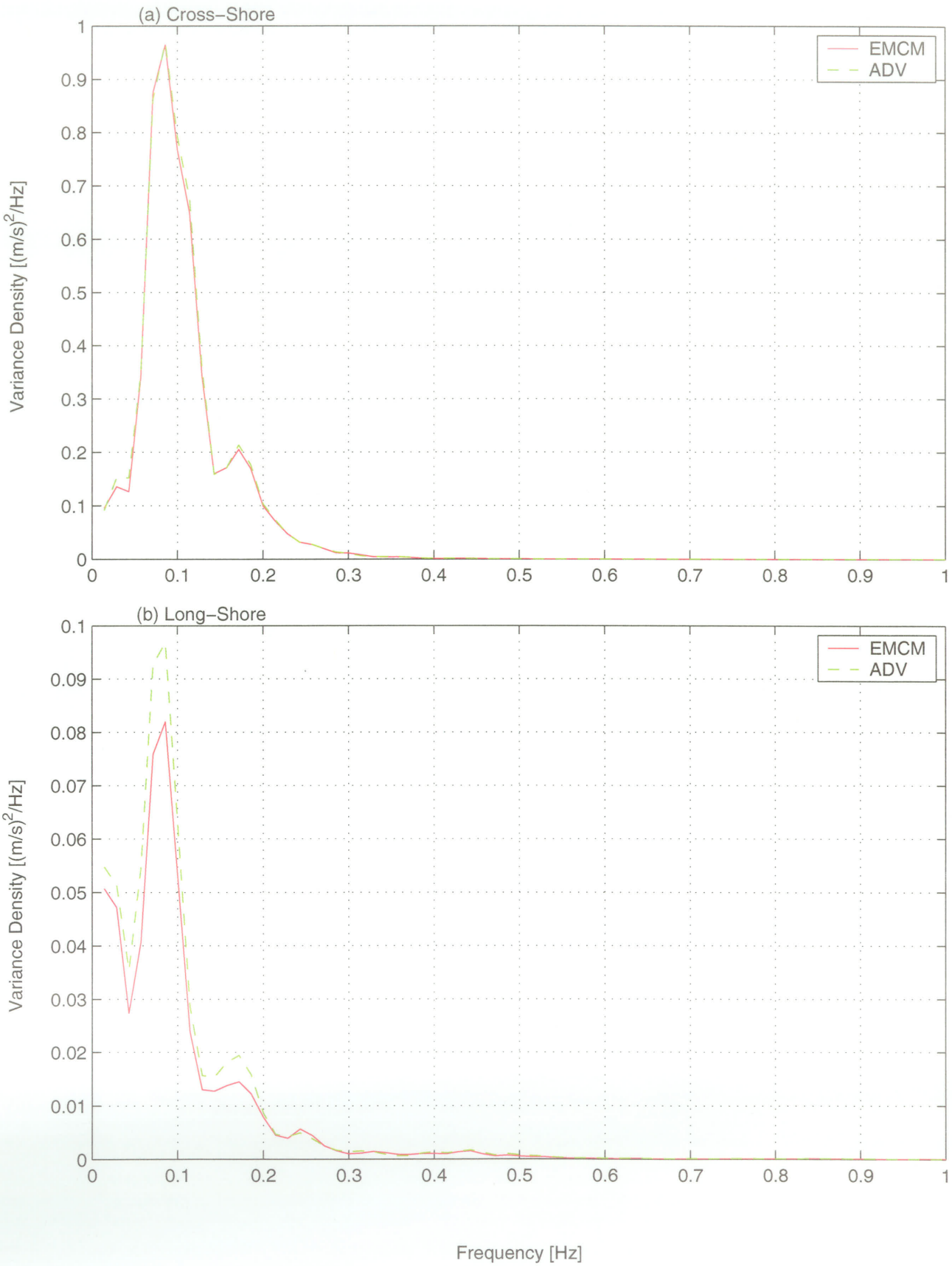

Figure 3.13. Power spectra for 05:30, October 11, 1997.

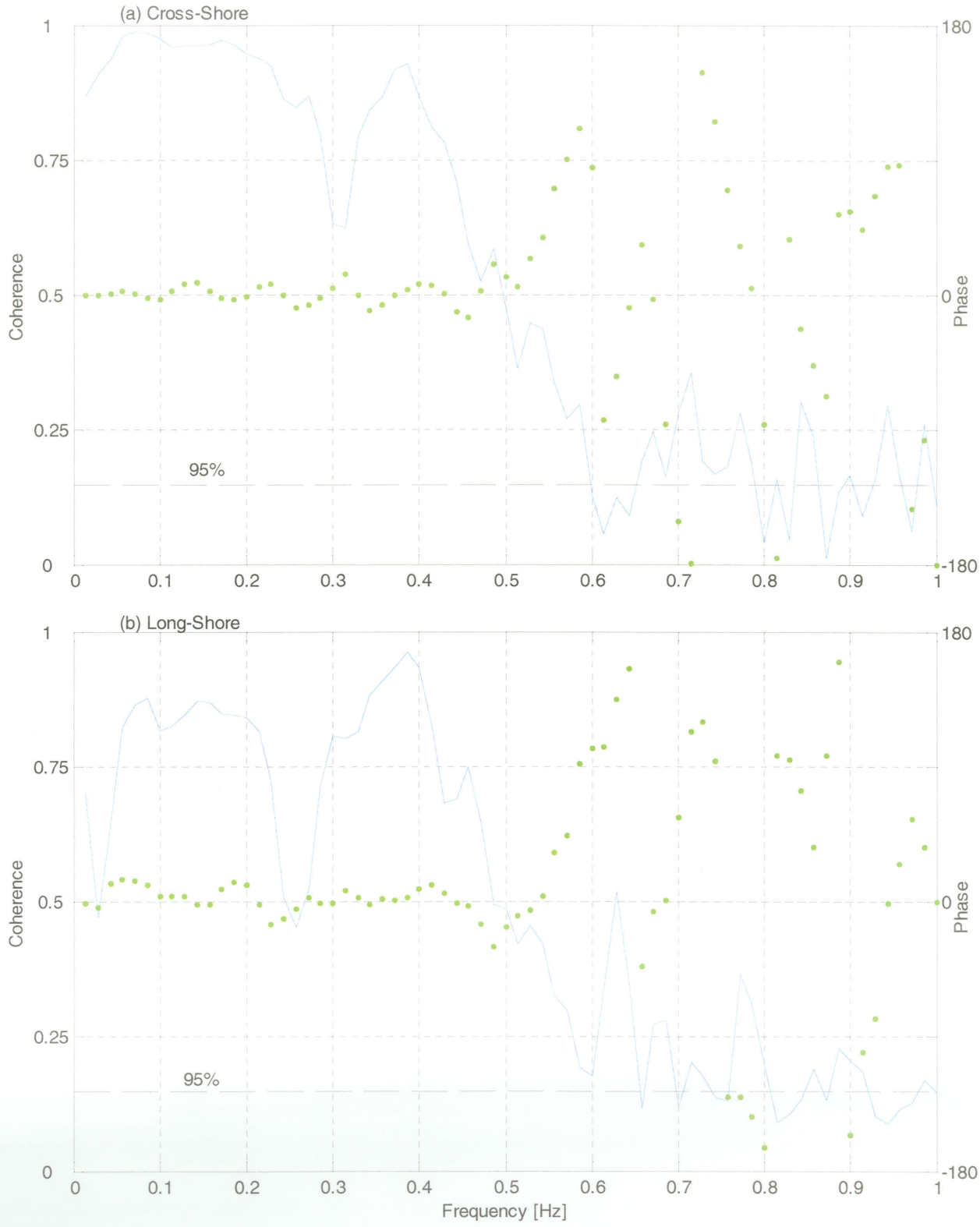

Figure 3.14. Coherence and phase spectra for 19:30, October 4, 1997.

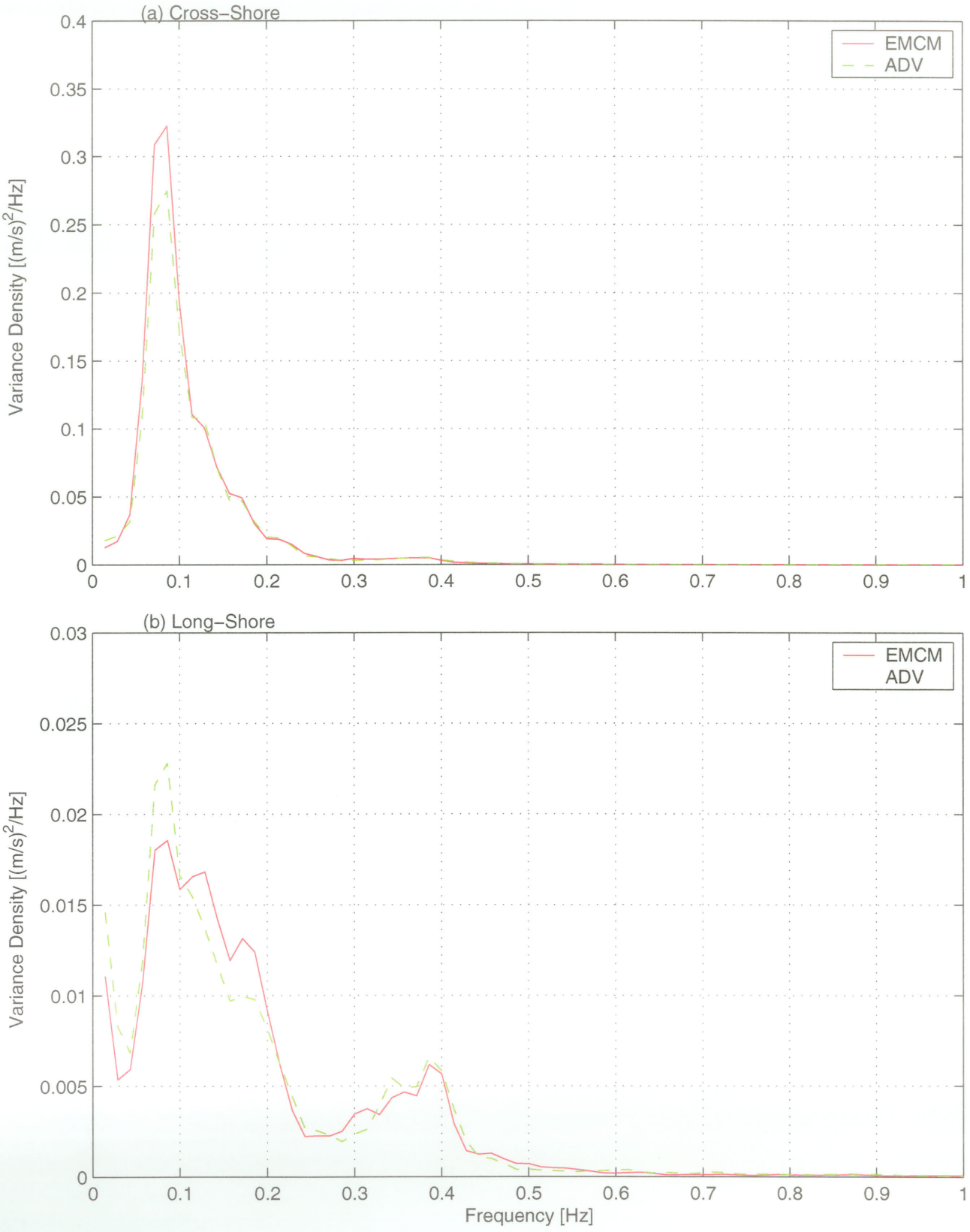

Figure 3.15. Power spectra for 19:30, October 4, 1997.

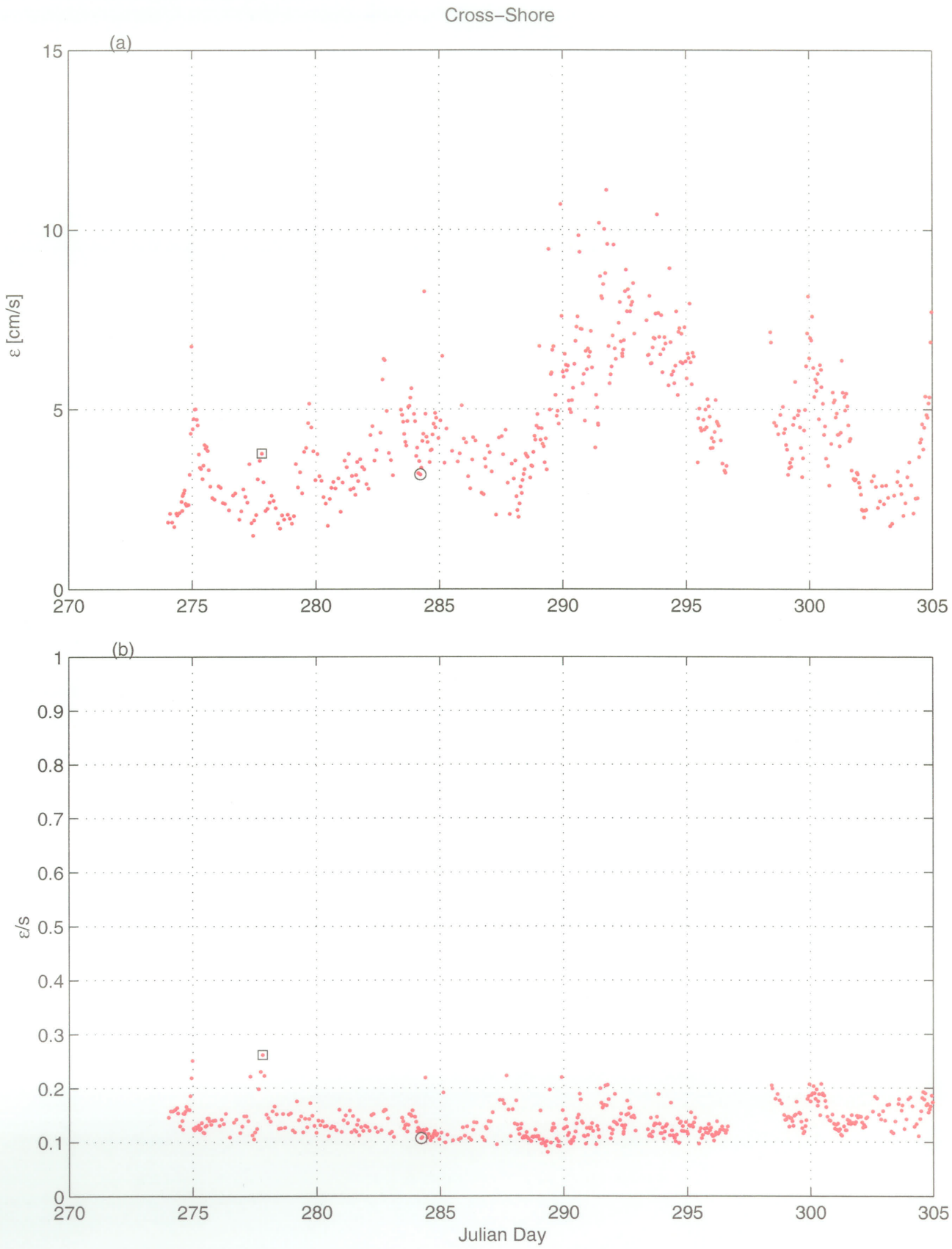

Figure 3.16. **(a)** Representation of the integrated variance of the incoherent signal between each ADV and EMCM (Cross-Shore) for frequencies up to 1 Hz. **(b)** Ratio of ε to the standard deviation of the respective record (Cross-Shore).

Figure 3.17. **(a)** Representation of the integrated variance of the incoherent signal between each ADV and EMCM (Long-Shore) for frequencies up to 1 Hz. **(b)** Ratio of ε to the standard deviation of the respective record (Long-Shore).

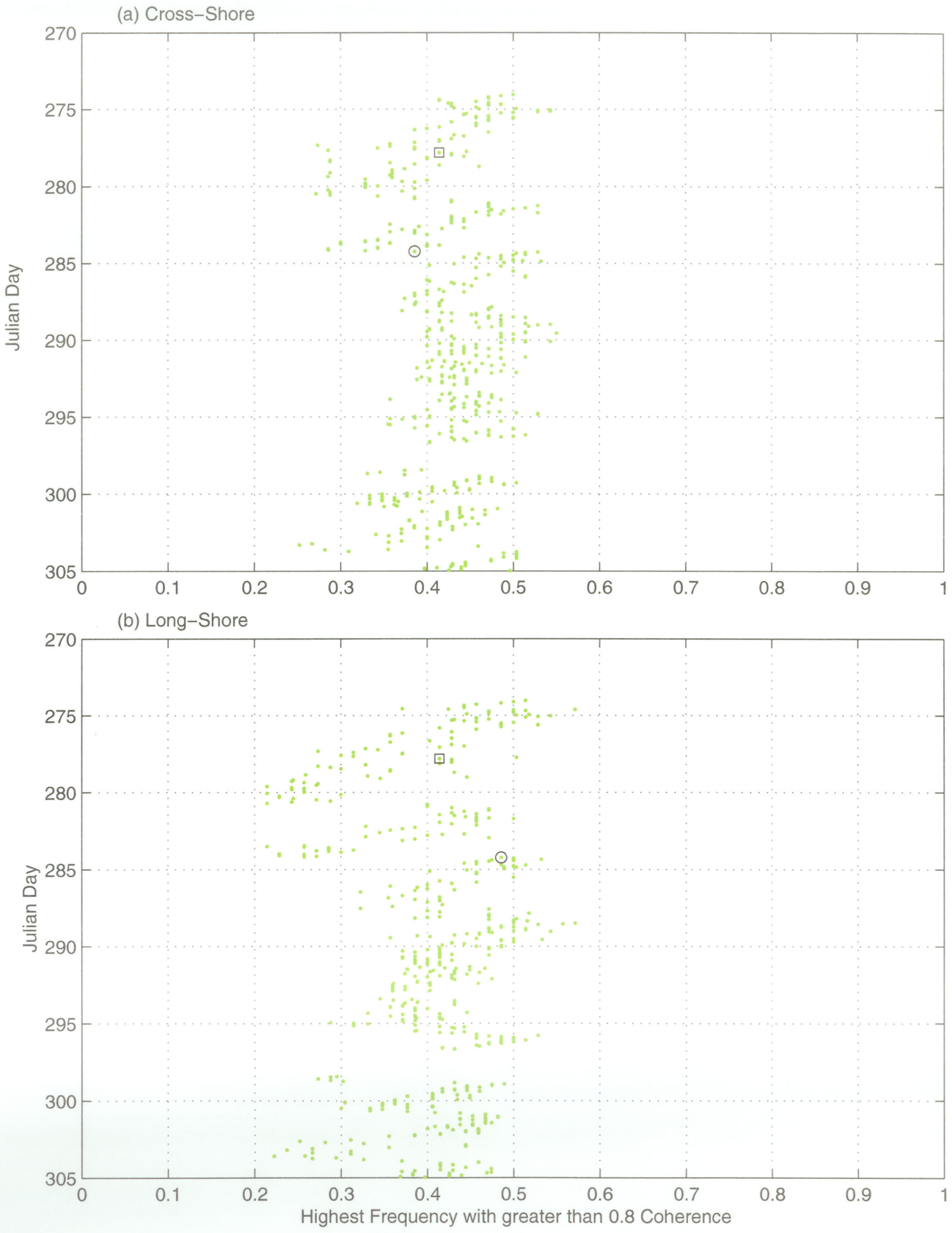

Figure 3.18. Upper frequency limit for coherence values greater than 0.8.

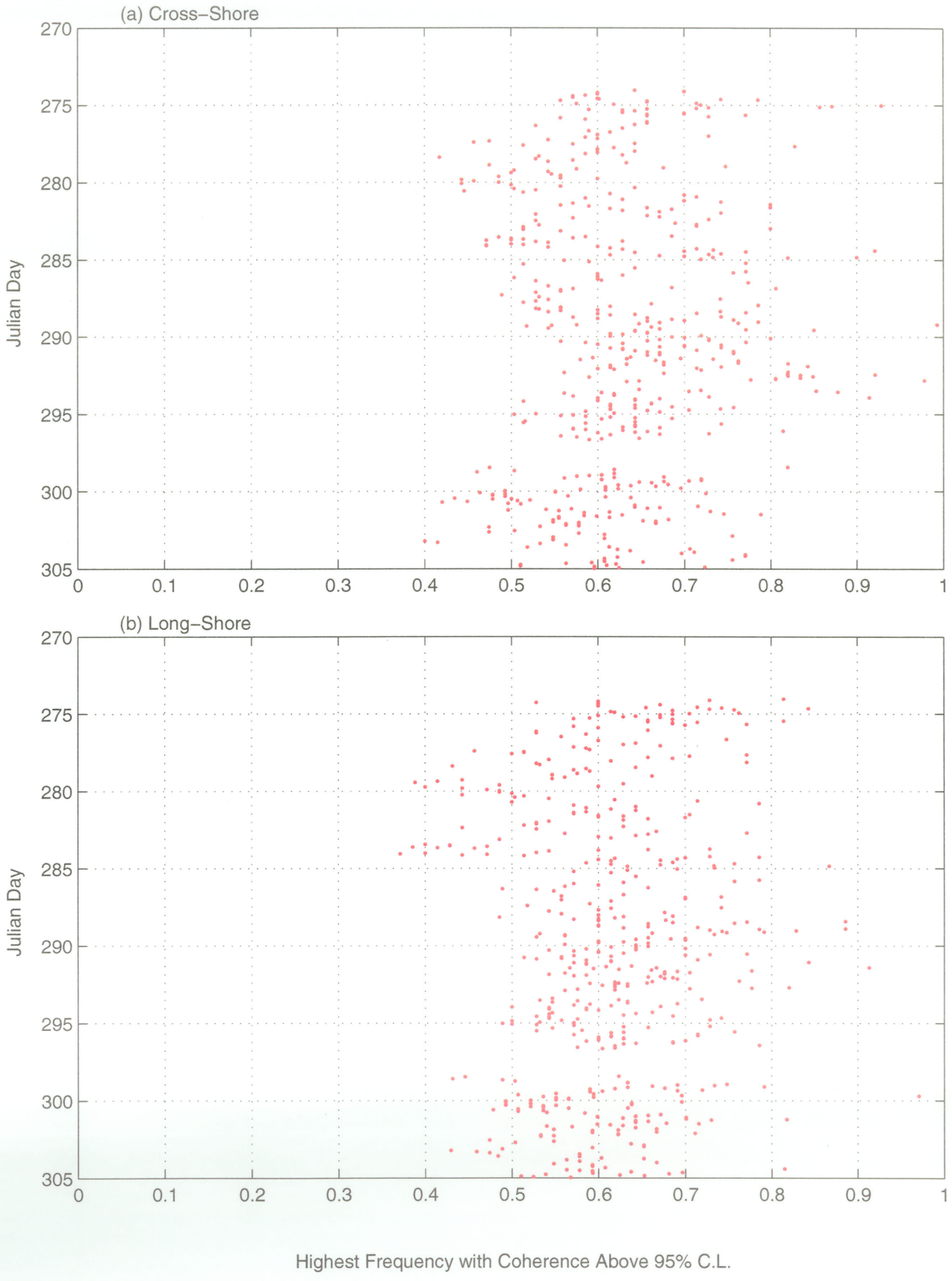

Figure 3.19. Upper frequency limit for coherence values greater than 95% C.L.

CHAPTER 4

Nearshore Velocity Skewness

4.1 Introduction

The response of nearshore beach sediments to wave skewness has been examined by many researchers. The earliest sediment transport models incorporated a skewness dependence and researchers such as Bailard and Inman (1981), etc, have theoretically and experimentally proven this dependence. Nearshore wave skewness, and contributions to skewness have been examined using simple moment analysis as well as bispectral analysis. The general motivation for such research is to attempt to resolve the spatial and temporal variability of wave induced skewness. This, in turn is needed in order to use sediment transport models for beach evolution modeling.

In chapter 1, sediment transport models were introduced. It has been shown (Bowen, 1980) that for a beach in equilibrium

$$\tan\beta = \tan\phi \frac{\langle u^3 \rangle}{\langle |u|^3 \rangle}. \tag{4.1}$$

This equation relates the skewness of the cross-shore wave field to the beach slope, β if beach equilibrium occurs by bedload transport, (i.e., $\langle i_b \rangle = 0$).

Attempts have been made to develop a means to estimate, or parameterize, the wave-induced skewness in the nearshore zone. Three such attempts are described in the following sections. These techniques or formulations are then used to estimate the skewness using the data described in §2.0 and compared with the skewness values computed from each time series. For the purpose of these comparisons, this computed skewness shall herein be referred to as "measured skewness".

4.2 Expansion of The 3rd Moment

The expansion of the third moment of near shore velocities was used by Foote and Huntley (1992) to examine the relative contributions of the various terms to the total skewness. The expansion or decomposition of $\langle u^3 \rangle$ in equation 4.1, yields ten terms, i.e.,

$$\langle u^3 \rangle = \left(\overline{\bar{u} + u_s + u_l}\right)^3 \tag{4.2}$$

$$= \bar{u}^3 + \overline{u_s^3} + \overline{u_l^3} + \overline{3\bar{u}u_s^2} + \overline{3\bar{u}u_l^2} + \overline{6\bar{u}u_s u_l} + \overline{3u_l^2 u_s} + \overline{3u_s^2 u_l} + \overline{3\bar{u}^2 u_s} + \overline{3\bar{u}^2 u_l}\,.$$

where u_s and u_l are the short and long wave components, respectively, and $\bar{u}$ is the mean cross-shore velocity.

Certain hypotheses about the magnitude of these terms are often used to simplify (4.2). Common hypothesis are (Bowen, 1980; Roelvink and Stive, 1989; Foote and Huntley, 1994)

- $u_s >> \bar{u}, u_l$
- u_s is uncorrelated to $|u_l^2|$

With these hypotheses, (4.2) is reduced to

$$\langle u^3 \rangle = \overline{u_s^3} + \overline{3\bar{u}u_s^2} + \overline{3u_s^2 u_l}\,, \tag{4.3}$$

where the terms $\overline{u_s^3}$, $\overline{3\bar{u}u_s^2}$, and $\overline{3u_s^2 u_l}$ will be herein after denoted term 2, term 4 and term 8, respectively.

The relative contributions of all ten terms to the total skewness, as defined in equation 4.2, for the ADV at frame B, just seaward of the bar, can be seen in Figures 4.1. It is readily apparent that terms 2, 4 and 8 comprise a large fraction of the total skewness. Foote and Huntley (1992) found that these terms dominate outside the surf zone. They found, however, positive (onshore) skewness for terms 2 and 4, and negative skewness (offshore) for term 8. The negative skewness found for term 4 is a

result of the offshore currents found at this site, which would promote an offshore transport of sediment. This term will have high values during energetic seas with non-zero current (Figure 4.2) because it represents the mean flow transported sediment that has been mobilized by the short waves. The positive values that are typical of term 8 indicate a positive correlation between the short and long wave components. These are not bound long waves, because they are in phase with the short wave part. Bound long waves are locked, and 180° out of phase with the short waves if they are forced by radiation stress phenomenon.

The trend and mean current were removed from all records but the mean of each was retained. The data were low and high-passed using Graham filters. In order to determine the cutoff and terminal frequencies, f_c & f_t, a unique method that incorporates the bispectrum (Appendix A) was used. The real part of the bispectrum describes the skewness contribution associated with various frequency interactions. Difference interactions, which result in negative contributions to the skewness, occur near the axis (i.e., either f_1 or f_2 is a low frequency). There typically exists an approximate frequency at which the high frequency interactions (positive skewness) begin to increase the total skewness. Figure 4.3 shows a band integration of the real part of the bispectrum, showing the integrated skewness between any two upper and lower limits in the bispectrum. The back face of this band integration surface (Figure 4.4) represents the integration between lower limit f_l and the maximum frequency, f_{max}, represented in the bispectrum. As the lower limit is reduced from f_{max} to f_{min}, the integrated values increase until they reach a maximum, after which the difference interactions, with negative values, begin to lower them again. This maximum, computed for each record of the experiment, was used as the cutoff for the high and lowpass filters. The terminal frequency, f_c was set to a value 0.005 below or above the lower or upper cutoff frequency, respectively.

Figure 4.5 shows the total skewness at Frame B (4.2) throughout the experiment vs. the skewness calculated using (4.3). Notice that the three terms in (4.3), alone, often do not completely describe the total skewness. This indicates that the remaining terms in (4.2) may be more significant than was hypothesised. It is apparent that although (4.3) does not completely account for the total skewness at Frame B, it predicts the most significant part thereof. Virtually all points lie above a one-to-one line on the figure. The best-fit line, with zero y-intercept, has a slope of m=0.75 and a resulting r^2 value of 0.71.

What might not be largely evident in Figure 4.1 is the strong correlation between some of the terms that have not been included in Eq. 4.3. Table 4.1 lists the correlation coefficients from each combination of the eight terms. Again, terms 9 and 10 were not included because their magnitudes are much too small to contribute appreciably to the total skewness.

TABLE 4.1, Correlation between terms in Equation 4.2

Term	*1*	*2*	*3*	*4*	*5*	*6*	*7*	*8*
1	1.00	-0.63	0.31	0.88	0.89	0.76	0.36	-0.52
2		1.00	-0.66	-0.86	-0.82	-0.81	-0.51	0.77
3			1.00	0.41	0.51	0.58	0.35	-0.72
4				1.00	0.93	0.85	0.53	-0.59
5					1.00	0.88	0.39	-0.76
6						1.00	0.49	-0.72
7							1.00	0.10
8								1.00

The table shows that many of the terms in (4.2) are strongly correlated. Of the terms neglected in the development of (4.3), terms 1, 5 and 6 are all strongly correlated with one another. Figure 4.6 shows the sum of terms 1, 5 and 6 compared to that of terms 2, 4 and 8. Although the correlation between terms 1, 5 and 6 may (or may not) be only the result of a shared correlation with the energy of the sea, the fact remains that when combined, they can contribute significantly to the total velocity skewness. In addition, Table 4.1 reveals that not only are terms 1, 5 and 6 strongly correlated with one another, they are strongly correlated with the terms in (4.3). As can be seen in Figure 4.7, terms 1, 5 and 6 are well correlated with the velocity variance, indicating that they are significant contributors to the total velocity moment during high-energy periods. The relationship between the sum of these terms and the velocity variance is exhibited in Figure 4.8. In fact, many of the terms exhibit similar relationships to the velocity variance.

4.3 Parameterization of Velocity Skewness

The parameterization equations described in §1.0 have been used to estimate the skewness of the data described herein. These include the parameterization techniques developed by Doering and Bowen (1995) and those developed by Doering and Elfrink (2000). The skewness for each velocity record is computed using the bispectrum, which provides a convenient means of determining the skewness and asymmetry arising from wave-wave (triad) interactions, something that cannot be examined using the typical 3rd-moment computation of skewness which simply gives bulk skewness.

The bispectrum is used to examine wave-wave interactions that lead to skewness through phase-coupling. The bicoherence spectrum is used to identify significantly phase-coupled modes. The relative contribution to the total skewness arising from phase-coupled modes is examined using the real part of the bispectrum. Similarly, the imaginary part of the bispectrum is used to examine the relative effect that each phase-coupled mode has on the total asymmetry.

The bispectrum is formally defined as the Fourier transform of the second-order covariance function (Hasselmann, 1963)

$$B(f_1, f_2) = \int_{-\infty}^{+\infty} \int_{-\infty}^{+\infty} S(\tau_1, \tau_2)\, \mathrm{e}^{-i(2\pi(f_1\tau_1 + f_2\tau_2))}\, d\tau_1 d\tau_2 \,, \tag{4.4}$$

where

$$S(\tau_1, \tau_2) = \mathrm{E}\left[\zeta(t)\zeta(t+\tau_1)\zeta(t+\tau_2)\right], \tag{4.5}$$

τ_1 and τ_2 are lags, and E[ ] indicates an expected value. The bispectrum can also be expressed in terms of complex Fourier coefficients (Kim and Powers, 1979)

$$B(f_1, f_2) = \mathrm{E}\left[A(f_1)A(f_2)A^*(f_3)\right], \tag{4.6}$$

where the convention is $f_1 + f_2 = f_3$, and * indicates a complex conjugate. $B(f_1, f_2)$ will be zero, unless

i) there are waves present at the frequencies f_1, f_2, and f_3, and

ii) there is a phase persistence, or phase relation, between the waves at these frequencies.

Physically, if the waves present at f_1, f_2, and f_3 are normally excited modes, then each wave will be characterized by a statistically independent, or random phase, and the expected value of $B(f_1, f_2)$ will be zero. If, however, the sum or difference wave, f_3, is generated through an interaction between f_1 and f_2, then a persistent phase relation exists and the expected value of $B(f_1, f_2)$ will be non-zero.

4.3.1 Bispectral Integration

In order to estimate the skewness arising from certain triad interactions, the bispectrum is integrated between frequencies. In the present study, the bispectrum was integrated across wind-wave frequencies and across the frequencies involved in the peak-peak triad interactions. These limits are determined using the power spectrum.

In order to isolate the wind-wave contribution to the total skewness, the lower limit of the high frequency interactions (wind-waves) are taken as those frequencies above the location on the rising limb of the peak, which corresponds to a power spectral value equal to half the peak (Figure 4.9). There is no upper limit.

The skewness, asymmetry and integrated biamplitude, resulting from integration of the real, imaginary and amplitude bispectra, respectively, were computed for all records on frame B. Note that these integrated values have been normalized by the variance of the frequencies involved in each particular interaction.

4.3.2 Observations

As discussed in Chapter 1, Doering and Bowen (1995) developed relationships for B_{ww}, S_{ww} and A_{ww}. These are again given in equations 4.7 through 4.9, respectively.

$$B_{ww} = 0.8 + 0.62\log(Ur) \tag{4.7}$$

$$S_{ww} = [0.8 + 0.62\log(Ur)]\cos\{[-90° + 90°\tanh(0.73/Ur)]\pi/180\} \tag{4.8}$$

$$A_{ww} = [0.8 + 0.62\log(Ur)]\sin\{[-90° + 90°\tanh(0.73/Ur)]\pi/180\} \tag{4.9}$$

Where the Ursell parameter, *Ur*, was computed using a shallow water approximation and is given by

$$Ur = \frac{3}{4}\frac{g}{8\pi^2}\frac{H_c T_p^{\,2}}{h^2} \tag{4.10}$$

To evaluate the parameterization equations developed by Doering (1995), the Ursell number was computed for each record using (4.10). Figure 4.10 shows the integrated biamplitude for the wind-wave frequencies vs. the Ursell number. The predicted value (4.7) is also shown. The observed and predicted wind-wave skewnesses and asymmetries are shown in Figure 4.11. While these equations were a reasonable fit to the data studied by Doering and Bowen (1995), they are obviously inadequate for the present data.

From Figure 4.11, it appears that there was very little wave asymmetry at this location during the experiment. Equation (4.9) predicts that the waves will begin to pitch forward, resulting in horizontal asymmetry, when the Ursell parameter reaches values over 0.4. As was discussed in §1.0, the presence or development of wave asymmetry leads to an eventual decrease in wave skewness, which was not exhibited in this dataset. Figure 4.12 illustrates a time series of pressure measurements recorded at 03:00, on October 21, 1997. This pressure record corresponds to the ADV record with the highest value for the Ursell parameter. It is evident from this pressure record that these wave are, in fact, not asymmetric. To add to this point, Figure 4.13 shows colormap plots of the real and imaginary bispectra for this same ADV record. Recall that the real and imaginary bispectra indicate the amount of skewness and asymmetry, respectively, arising from the interactions of any two frequencies. This figure also indicates that there is very little asymmetry in these waves.

The parameterization equation developed by Doering et. al. (2000) has also been evaluated using this data. As mentioned in §1.0, these researchers developed an analytical expression for the skewness using easily predicted nearshore parameters:, i.e.,

$$S = -14.076\left[\tanh\left(1 + a_1 + \sqrt{a_2 + a_3} + a_4\right)\right] + 14.133, \tag{4.11}$$

where

$$a_1 = \frac{2.582}{L/h}, \tag{4.12}$$

$$a_2 = \left|\xi - 0.207\right|, \tag{4.13}$$

$$a_3 = \sqrt{\left|-0.22 + \left|\frac{\xi \tanh(Ur) + 2.527}{L/h}\right|\right| + \left(\frac{L/h}{Ur^2}\right)}, \tag{4.14}$$

$$a_4 = \left|\frac{L/h}{Ur} - 0.218\right|, \text{ and} \tag{4.15}$$

$$Ur = \frac{H_s L^2}{h^3}. \tag{4.16}$$

From equation (4.11), developed using genetic algorithms, it is difficult to draw a clear physical meaning. Figure 4.14 compares the measured skewness to that predicted using (4.11) through (4.16).

It is readily apparent that actual skewness values at this location are not accurately represented by this relationship. These results are particularly disheartening considering the relative success attained by these authors using this relationship on data collected at the same location and time as the data used in the present study. It is noted, however, that their data were collected a distance over 300 m from shore at depths of roughly 4 meters, whereas the data described in §2.0 were collected a distance less than 100 m from shore at depths of roughly 2 m.

Figure 4.15 describes the relationship between skewness and the Ursell number, as defined in (4.11) and (4.16). Note that this definition for the Ursell Parameter results in values more than two orders of magnitude greater than those predicted using (4.10), (i.e. $(3/4)/(8\pi^2) = 105.276$). To be consistent with earlier analysis in this thesis, the Ursell number, from this point forward, is normalized by this value after (4.11) is calculated. Just as Doering and Bowens equation for skewness (1995), this equation predicts an eventual decrease in skewness with increased Ur. There appears to be two overlapping "bands" in Figure 4.14. One band seems to relate measured to predicted skewness in what appears to be a linear manner, while the second does not. Seemingly, the reason for this is that while (4.11) predicts a decrease in skewness with Ur, there was no such decrease in the measured waves. Figure 4.16 is a plot of the velocity variance throughout the experiment. All values with an Ursell number greater than 0.6 are indicated with green dots. These same records are indicated in Figure 4.17 with green dots. It is apparent from looking at Figure 4.15 that Ur $\approx$ 0.6 is an

approximate inflection point for the relationship between the Ursell number (4.16) and the skewness predicted by (4.11). It is apparent, again, that the waves in this environment were not subject to asymmetry.

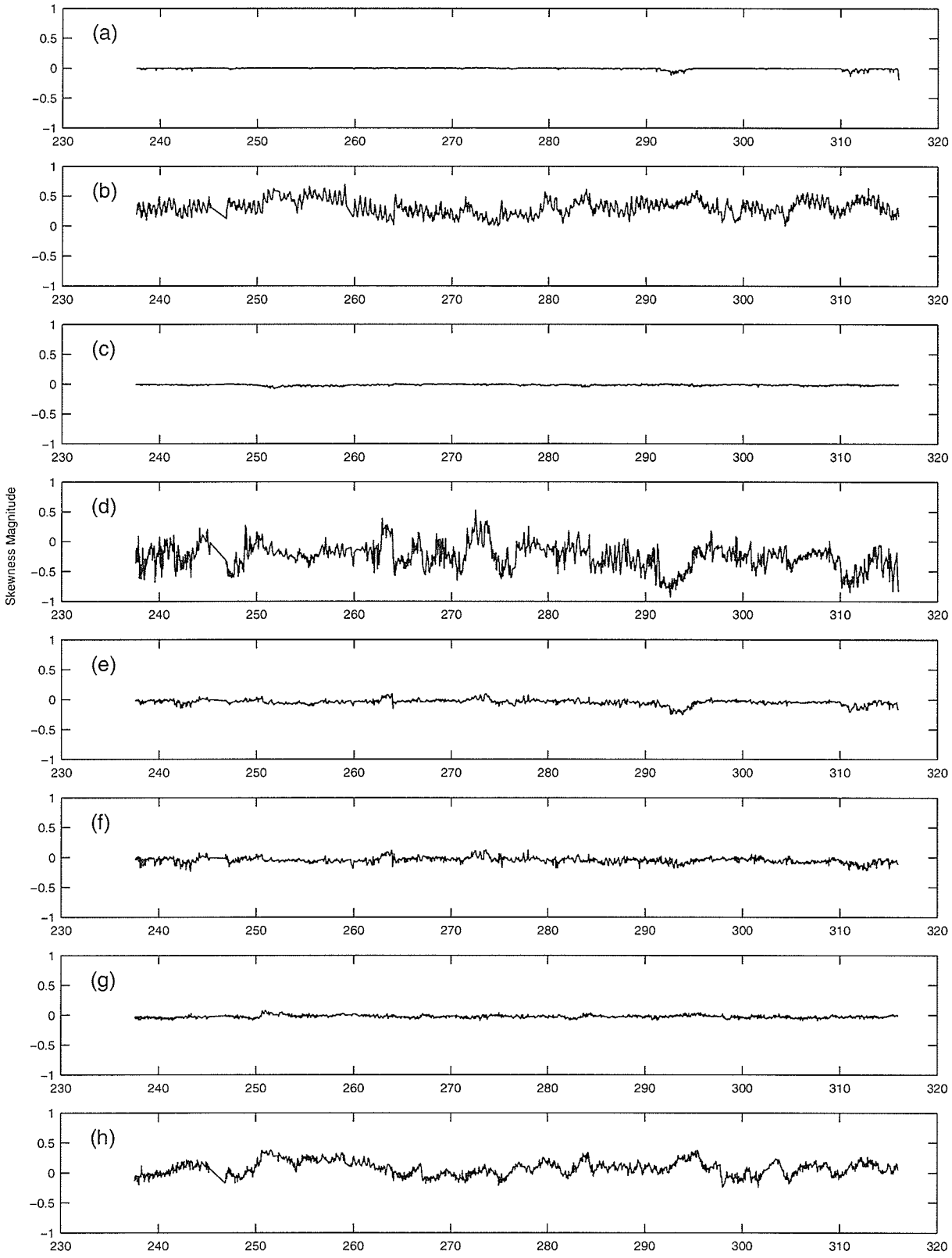

Figure 4.1: Skewness contributions at Frame B. The individual figures are the contributions arising from; **(a)** term 1, **(b)** term 2, **(c)** term 3, **(d)** term 4, **(e)** term 5, **(f)** term 6, **(g)** term 7 and **(h)** term 7.

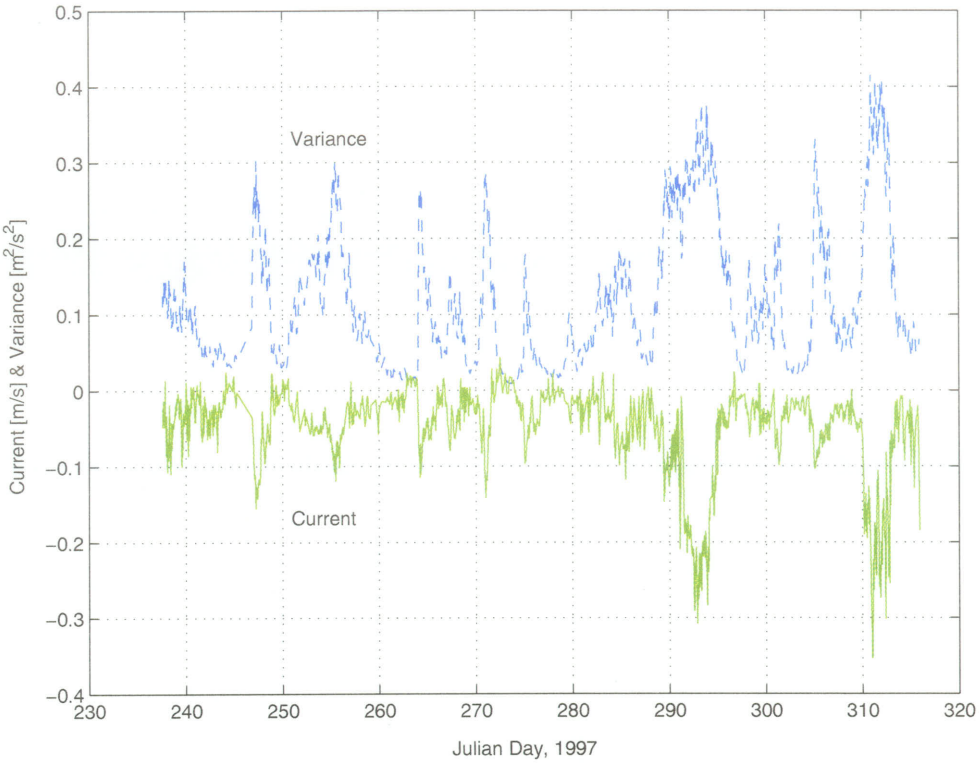

Figure 4.2: Cross-shore velocity variance (–) and current (– –) at frame B.

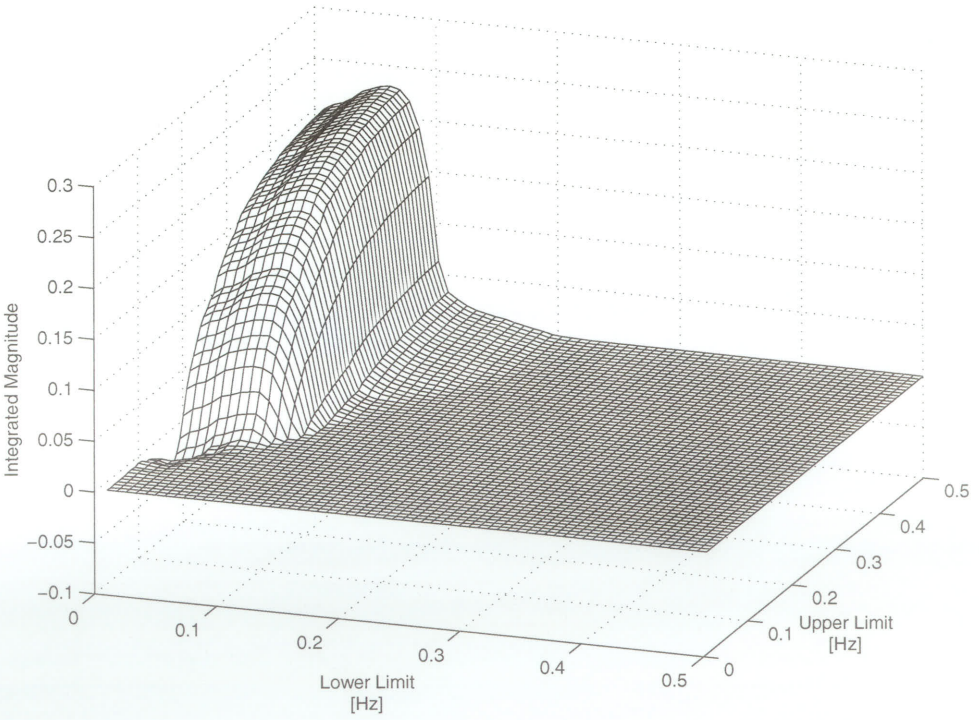

Figure 4.3: Example band integration of a record from Frame B.

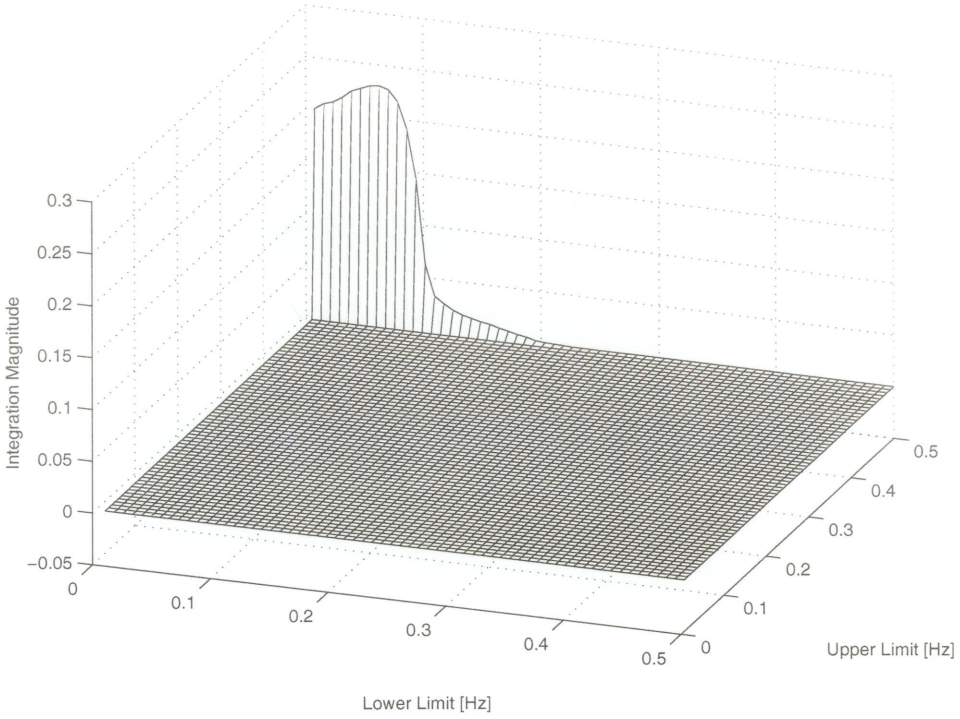

Figure 4.4: Back face of Band integration from Figure 4.4

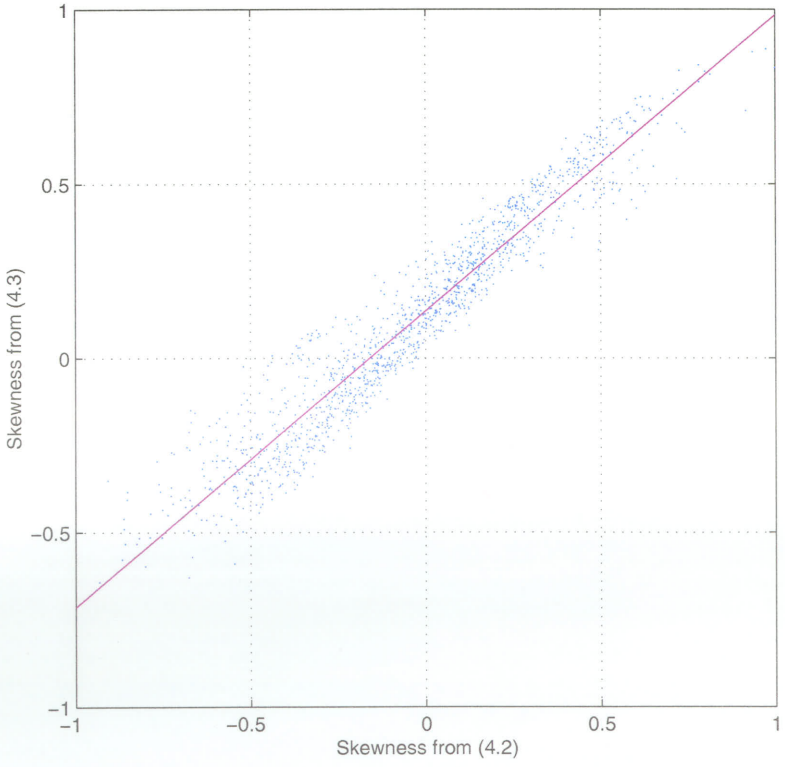

Figure 4.5: Skewness from Equation 4.3 vs. Total Skewness (Equation 4.2)

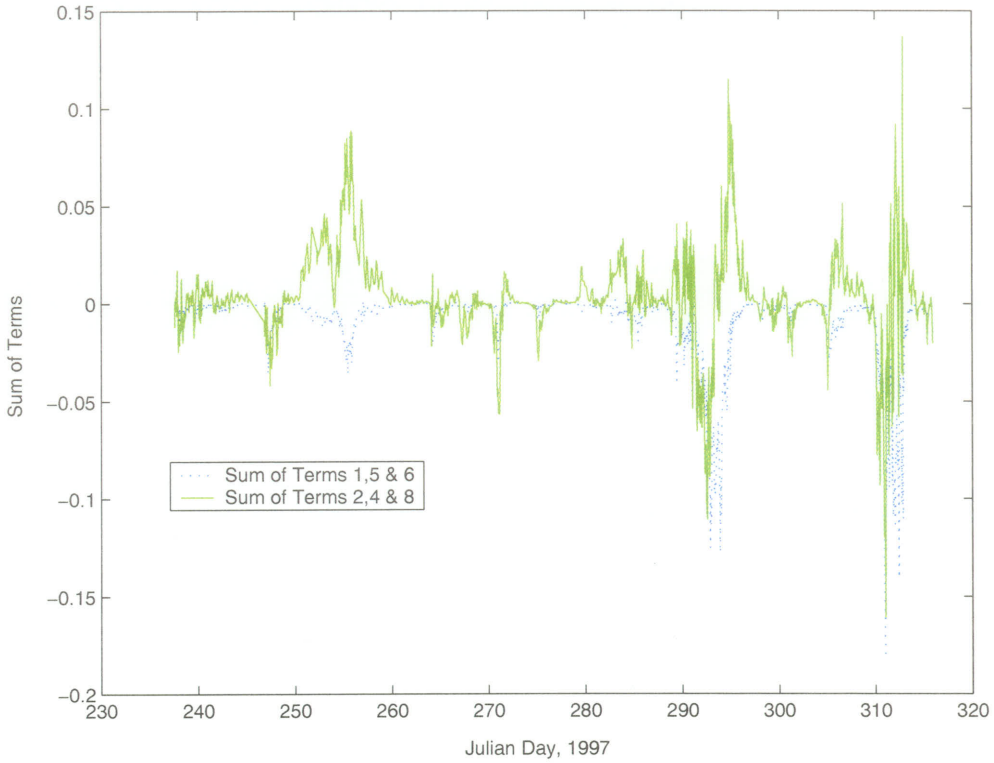

Figure 4.6: Total Skewness from terms 2, 4 & 8, and from terms 1, 5 & 6.

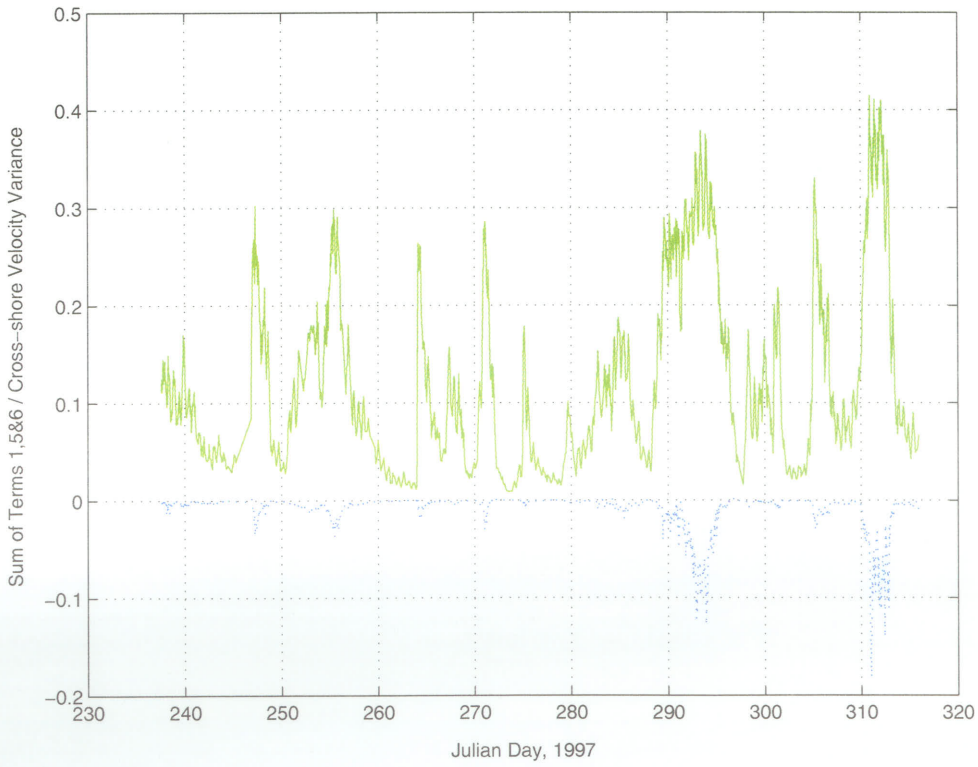

Figure 4.7: Skewness from terms 1, 5 & 6 and Cross-Shore Velocity Variance.

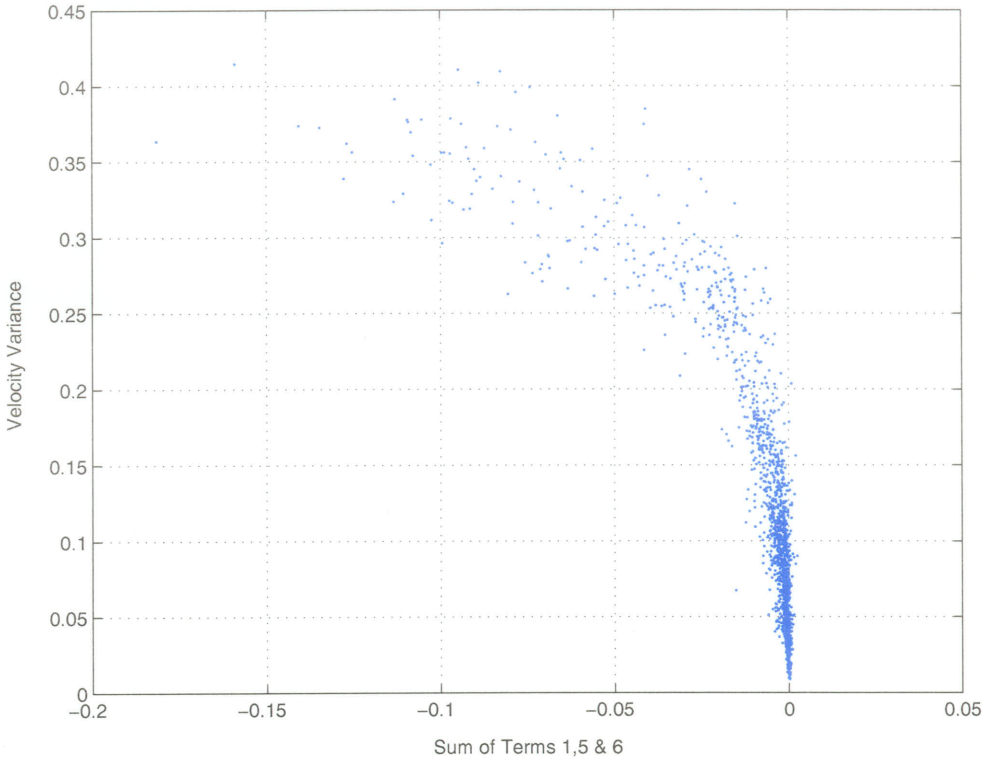

Figure 4.8: Velocity Variance vs. Skewness from Terms 1, 5 & 6.

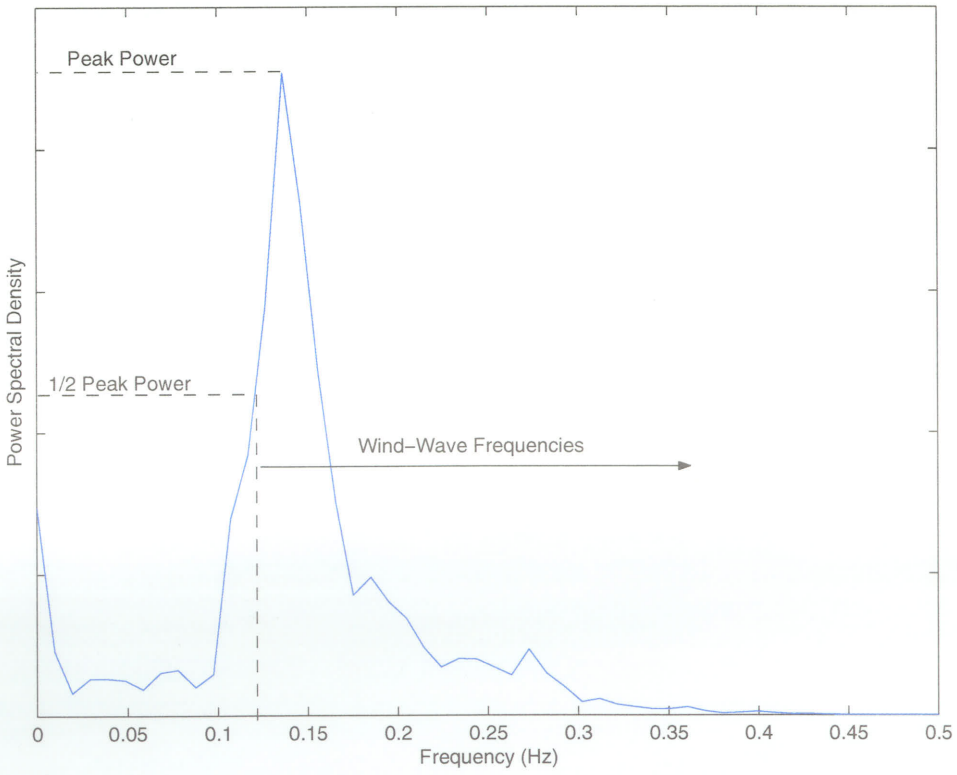

Figure 4.9: Example Power Spectrum illustrating adopted criteria for wind wave frequencies.

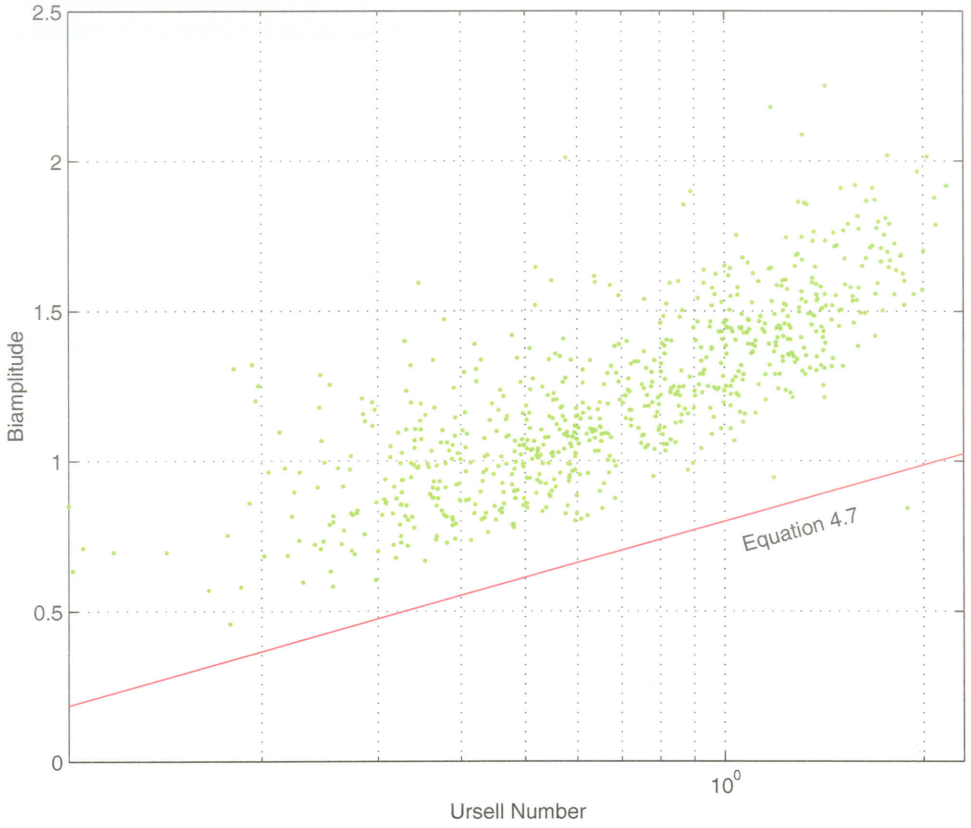

Figure 4.10: Measured and Predicted (Equation 4.7) Wind-Wave Biamplitude.

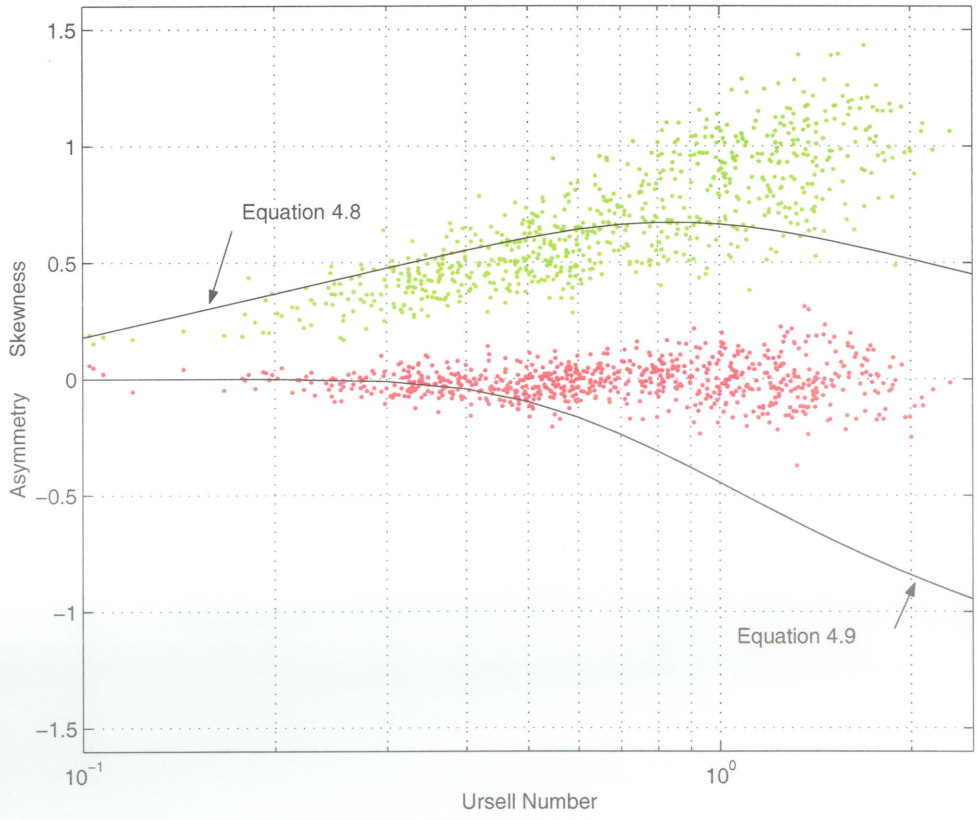

Figure 4.11: Measured and Predicted Skewnesses and Asymmetries.

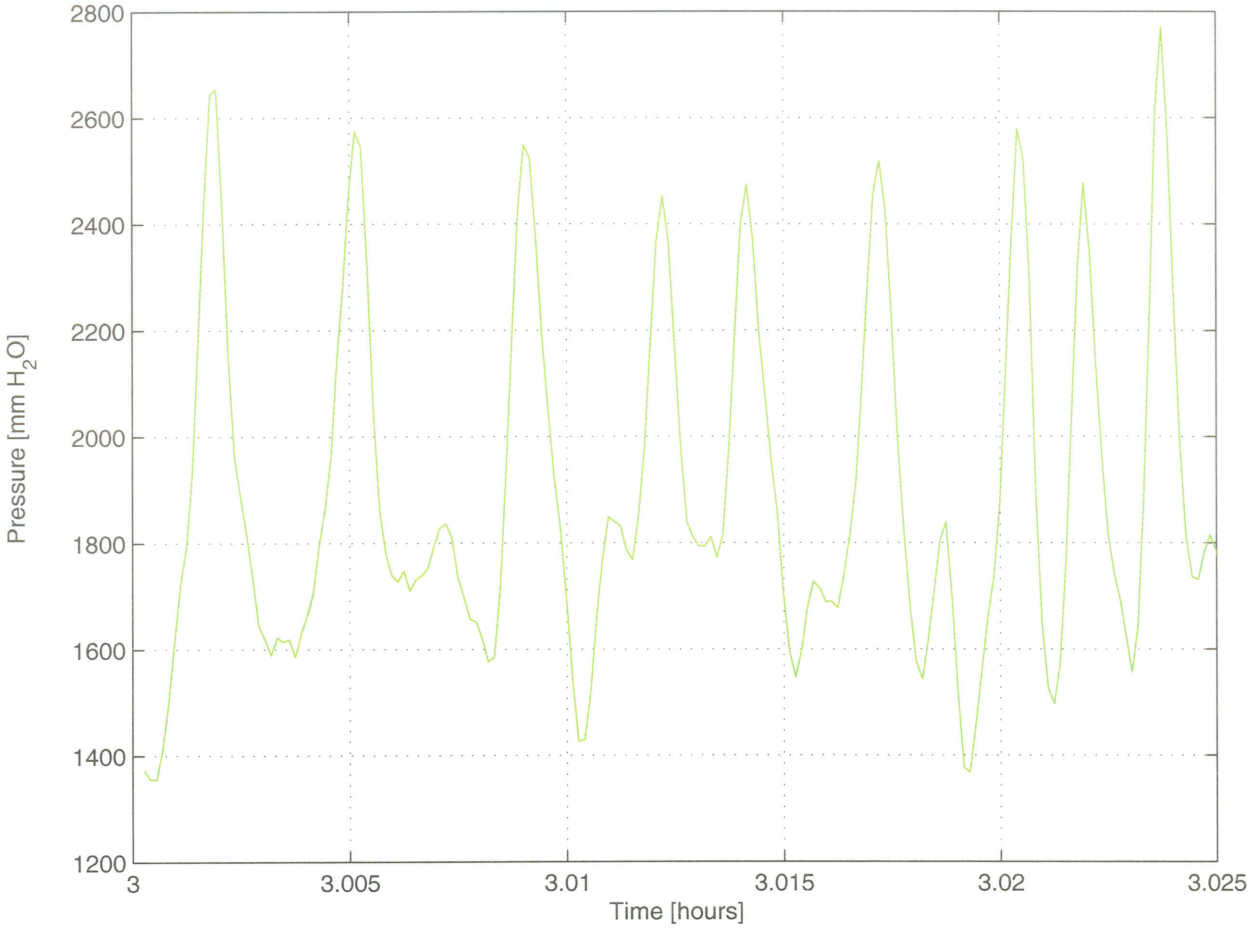

Figure 4.12. Pressure measurements from Frame B during the period of Highest Ursell Number, (03:00 October 21,1997).

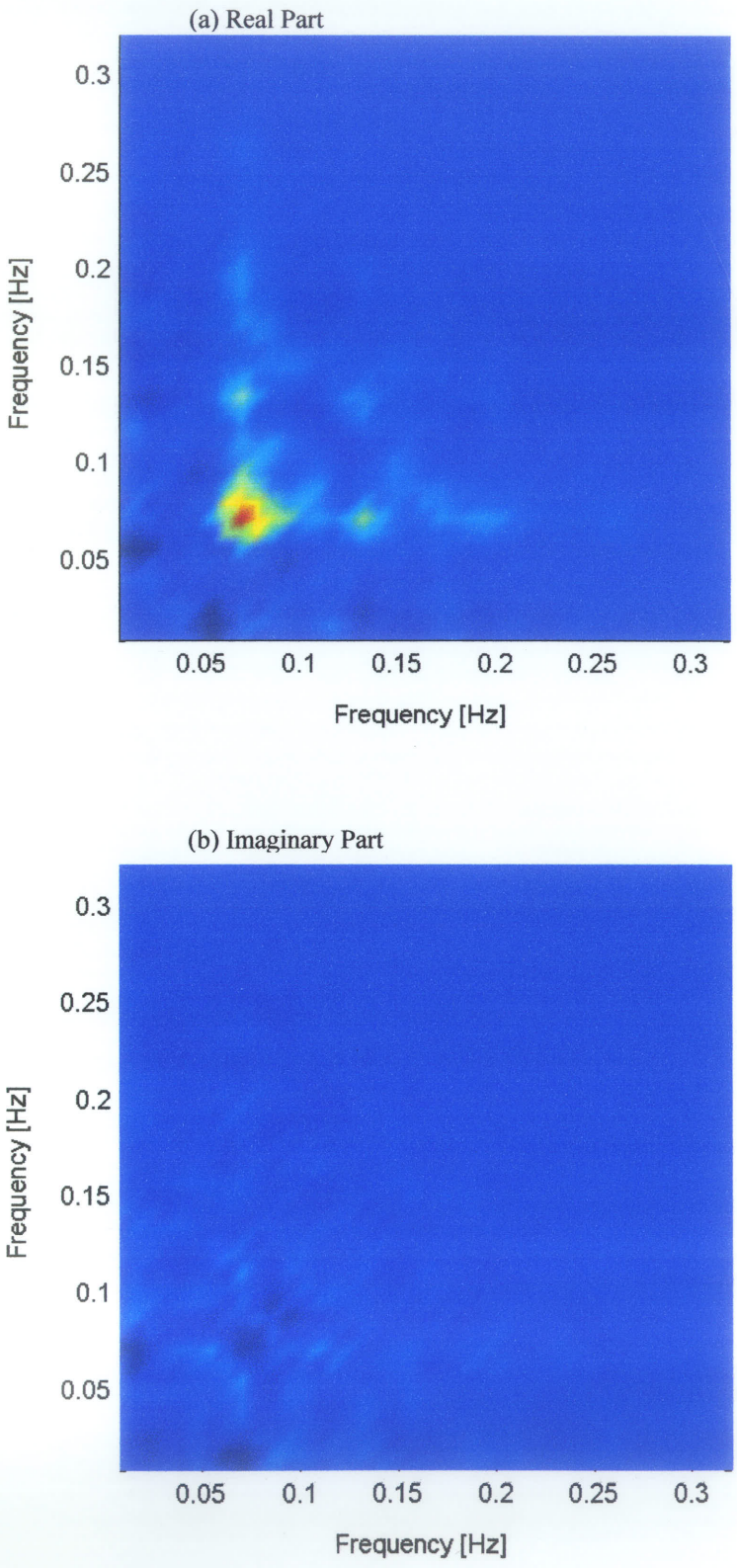

Figure 4.13. Real (a) and Imaginary (b) part of the bispectrum of velocity measurements from Frame B during the period of Highest Ursell Number.(03:00, October 21, 1997).

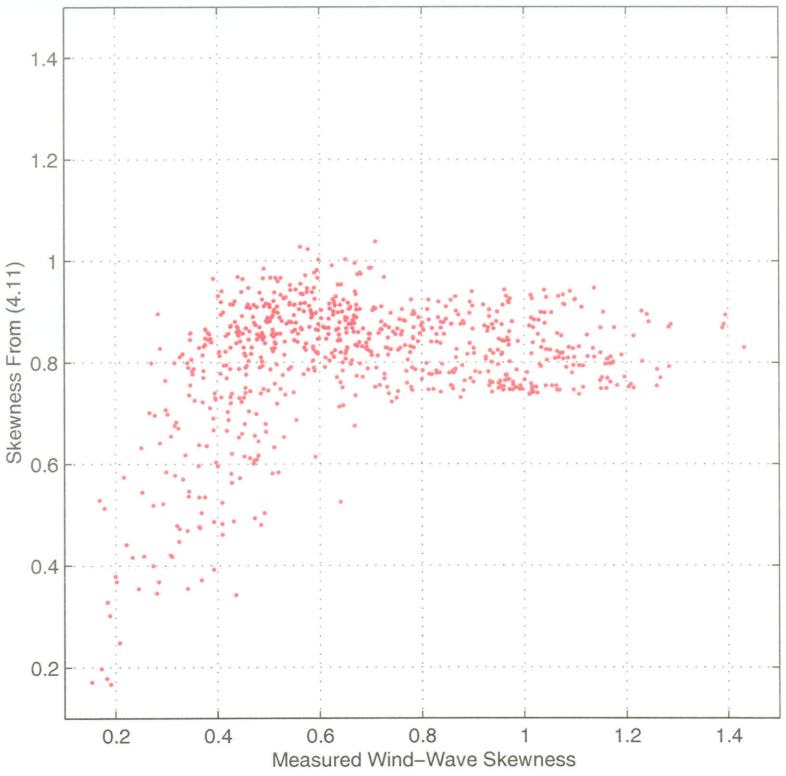

Figure 4.14: Measured Skewness vs. Skewness predicted by (4.11).

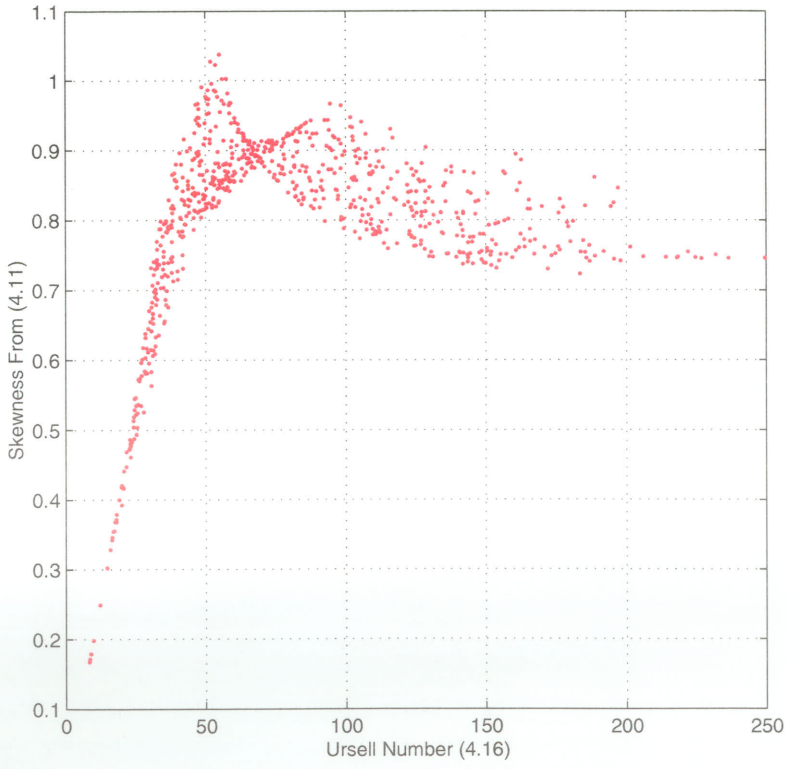

Figure 4.15: Skewness predicted from (4.11) as a function of the Ursell Number.

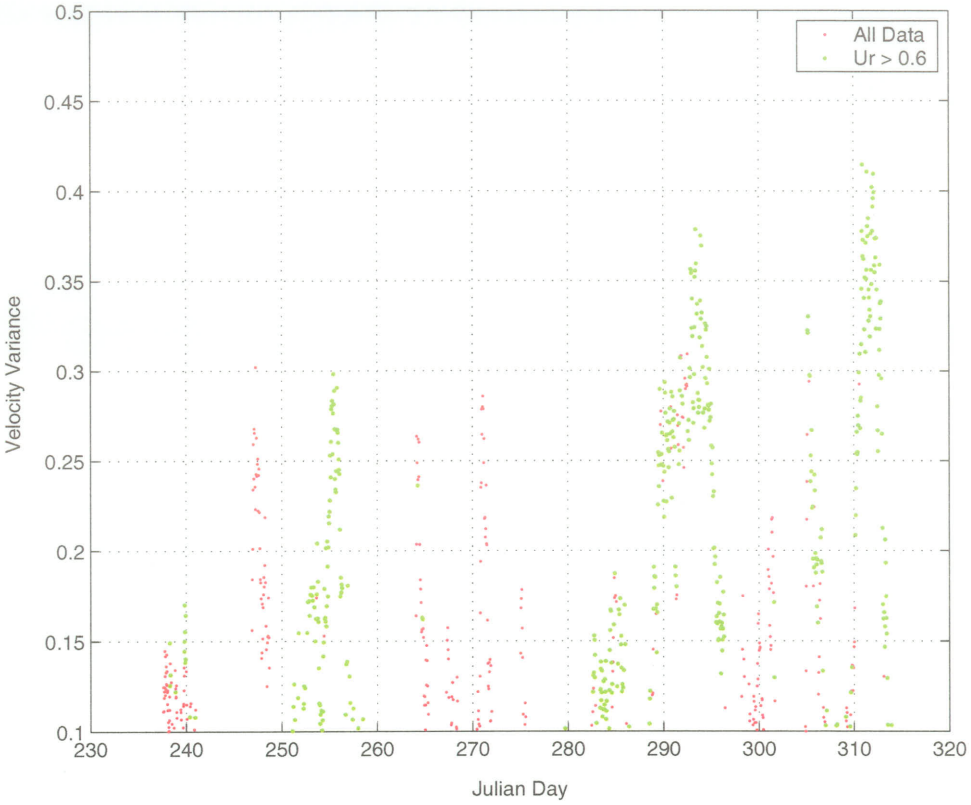

Figure 4.16: Time Series of Velocity Variance indicating records with Ur > 0.6.

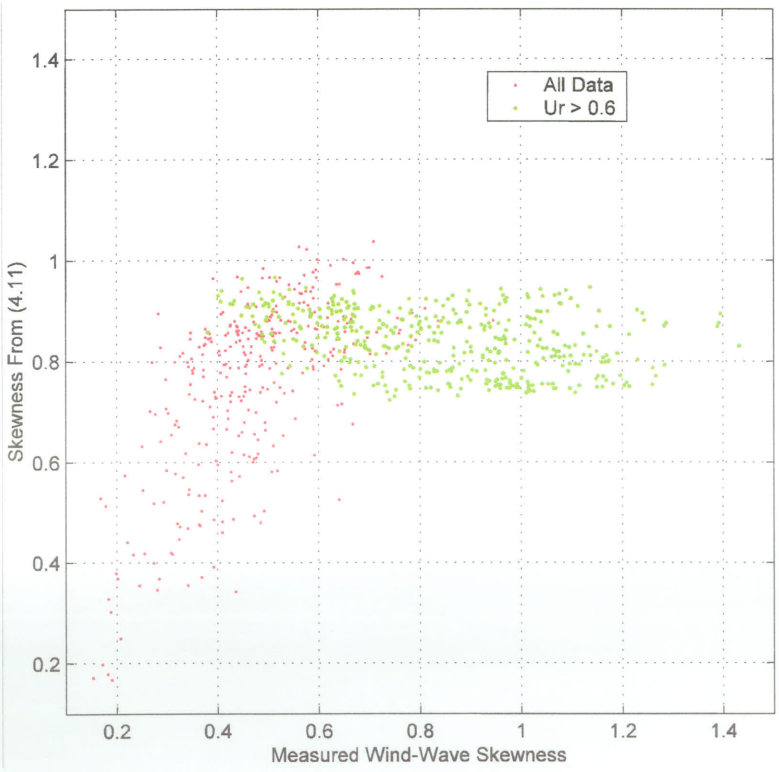

Figure 4.17: Measured Skewness vs. Skewness predicted by (4.11) indicating records corresponding to Ur > 0.6.

CHAPTER 5

Summary and Conclusions

5.1 Introduction

Researchers have been studying waves and wave-related phenomenon for centuries. The earliest of these focused their efforts on observation and the development of fundamental theories and mathematical relationships. With the emergence of electronic technology, instruments were developed to measure velocities, pressures, sediment load, etc. The capabilities of these instruments improved, but until recent times, hydrodynamic research was generally limited to datasets comprised of a few short records with low sampling-frequency.

Large collaborative coastal experiments have been increasing in popularity. One such collaboration of experimenters, SandyDuck '97, resulted in very large amounts of data, including the data set used in this study. The experiment took place in the fall of 1997, starting in August and ending in November. The research described in this thesis is part of a series of experiments within SandyDuck '97, performed by a Canadian team of Faculty and students from Dalhousie University, the University of Manitoba and Memorial University of Newfoundland.

The research is generally based on velocity data recorded at one of five locations in the nearshore that comprised the Canadian experiment. This location provided velocity measurements from near the ocean bottom recorded using modern acoustic instrumentation as well as concurrent and relatively collocated velocity measurements recorded using the more traditional electromagnetic current meter.

Using these data, this research generally included two very different objectives. The first, a comparison between the data recorded by these two instruments, was hoped to provide an irrefutable test of the accuracy of traditional electromagnetic current meters. The second objective was to

examine velocity skewness which has been shown to be an important factor in sediment transport and, therefore, influential to beach erosion and accretion.

In §1.0, an additional objective was to examine the adequacy of ADV instrumentation in measuring near bottom velocities. Two instrument frames, B and F, were equipped with both ADV and EMCM instrumentation, as described in §2.0. The ADV sensor on Frame F, being closer to shore and closer to the bottom, was subject to recurring instrument failures due to sedimentation and burial of the sampling volume. It was originally hoped that this frame would provide the most significant insight into the near-bed dynamics. As it turned out, however, the data was questionable, at best, for most of the duration of the experiment. With this being said, the ADV instrumentation was inadequate for measuring near bottom velocities in our case and conditions.

5.2 Summary

5.2.1 Intercomparison

As described in §2.0, a relatively large data set was available from instrument Frame B to perform an intercomparison between velocities recorded using acoustic doppler and electromagnetic sensors. The dataset, originally running from late August to mid-November, was limited to those records that were not expected to be significantly effected by bottom effects. Additionally, a time-jitter problem in the EMCM data through most of September, precluded its use in the intercomparison. It was decided that the data recorded during October and early November would be sufficient to perform the intercomparison.

With a dataset as large as this, the intercomparison necessarily involved bulk parameter comparisons. In order to introduce each comparitive parameter, two example records (05:30,October 11 and 19:30, October 4, 1997) were chosen to reflect the best and worst agreement, respectively, between the two instruments. Each comparative parameter was estimated for each of these example time series and then the bulk estimates were compared for all records simultaneously.

In order to compare the shapes of the recorded time series, the correlation coefficient was determined for each pair of records. The correlation coefficients were found to be very high, with r^2 values of 0.981 and 0.907 for the cross and long-shore records on October 11, 1997. The lowest correlations in

the entire dataset were found for the record on October 4, with r^2 values of 0.916 and 0.556 for cross and long-shore velocities, respectively. It was found for the entire dataset that in general, the cross-shore velocity records were highly correlated with r^2 values almost entirely exceeding 0.95. The long-shore velocities exhibited lower correlations with r^2 values generally exceeding 0.8.

The first four record moments; mean, variance, skewness and kurtosis were also computed in order to compare the shapes of the time series. The mean flows compared very well for the long-shore and cross-shore records, although the long shore exhibited a higher correlation. This is understandable since these current magnitudes were much higher (<1.5 m/s) than for the cross-shore (<0.4 m/s). Additionally, vertical variation is typically larger in the cross-shore oscillatory flow making the measurements more sensitive to vertical separation. The correlations were found to decrease for the higher moments with kurtosis ultimately exhibiting the poorest r^2 values. This is understandable since, for the higher moments, any differences between the two respective time series will be compounded.

In order to compare the velocity magnitudes and frequency distribution, which is not revealed in the preceding estimates, the time series were Fourier transformed and the power spectra compared. The power spectral value at a particular frequency indicates the amount of energy existing in the record at that frequency. Comparison of spectra correlations revealed very high r^2 values for both the cross- and long-shore records with values generally exceeding 0.98 and 0.95, respectively.

Coherence and phase spectra were compared for the two example time series and in bulk for the entire dataset. The integrated variance of the incoherent signal between each ADV and EMCM record was computed from these coherence spectra. Good agreement exists with deviations, ε, ranging from 2-12 cm/s, with the majority being below 5-7 cm/s, for both cross- and long-shore measurements. When normalized to factor out the velocity magnitudes, this integrated variance was generally found to be less than 15% of the record variance for cross-shore records and less than 40% for long-shore records.

Coherence values were found to drop below 0.8 beyond 0.3 Hz and 0.2 Hz, for cross- and long-shore records respectively. When compared to the 95% confidence limit for zero coherence, the majority of the records, both cross- and long-shore, were found to be coherent beyond 0.5 Hz. From observation

of power spectra, very little energy was found to exist beyond this value, indicating the incoherence is due to a high noise/signal ratio.

5.2.2 Nearshore Velocity Skewness

Skewness has been shown by many investigators to play a large role in the erosion and accretion of sandy sediments in beach environments. Skewness derives from nonlinearities in the wave field that cannot be estimated using linear theory. The use of higher order wave theories, such as Stokes Theory, for modeling the spatial variability of velocity moments like skewness is questionable because shoaling a Stokes wavetrain does not lead to wave asymmetry. This asymmetry is important because it lead to an eventual decrease in skewness.

If models such as Bagnold's model for bedload transport are to successfully be used to model beach evolution, a detailed spatial and temporal inventory of skewness will be necessary. Attempts to parameterize skewness have been presented. This study evaluates parameterization techniques proposed by; i) Doering and Bowen (1988), and ii) Doering and Elfrink (2000) using ADV data recorded for a period of over two months.

Contributions to skewness from low, high and mean flow components are also evaluated in order to evaluate relative importance to total skewness.

5.2.2.1 3rd Moment Expansion

Foote and Huntley (1992) examined the relative contributions to the total skewness by considering the total instantaneous cross-shore velocity as the sum of three constituent parts; the mean flow, high frequency and low frequency. This expansion lead to ten third moment constituent terms.

They found that, in general, three terms dominate the wave skewness outside the surf zone. These were the terms involving; i) the skewness of the incident short waves, ii) the correlation between incident waves and mean flow, and iii) the correlation between the short and long-wave motion. Inside the surf zone, the dominant terms involved; i) the skewness of the incident short waves, ii) the correlation between the incident short waves and a mean flow, and iii) the correlation between the long wave energy and a mean flow.

The same terms Foote and Huntley found to dominate the wave skewness outside the surf zone were found to dominate the data in the present research though these measurements were in transitional water.

Consistent with Foote and Huntley, the skewness of the incident short waves was positive indicating an onshore transport of sediment. Unlike Foote and Huntley, however, the second (and most) dominant contribution (term 4), where the incident waves mobilize sediments which then move with the mean flow, was found to be negative. This result of the offshore currents found at this site would act to promote offshore sediment transport. Finally, the last dominant term, (term 8), was found to be mostly positive unlike that found by Foote and Huntley.

The remaining terms, aside from the last two which will typically be negligible, have been further examined to evaluate their potential importance. It is shown that several of these remaining terms exhibit a strong correlation with each other and with the dominant three terms. Because of this correlation, these terms, when combined, could become more significant contributors to the total skewness at different locations in the Nearshore through wave migration.

5.2.2.2 Parameterization of Velocity Skewness

Using over two months of data, originally recorded at 25 Hz, two parameterization techniques have been tested. After evaluating the energy available beyond 2 Hz, it was decided to resample the data to 2Hz for computation efficiency.

The first parameterization technique, (Doering and Bowen, 1995), involved the use of equations relating Biamplitude, Skewness and Asymmetry to the Ursell number. When applied to the present dataset, relationships were evident but the results were tenuous.

The equation relating the skewness arising from wind-wave interactions to the Ursell was the first tested. The resulting relationships exhibited an r^2 value of 0.61 indicating a relationship, however the slope and intercept of the log-linear equation was not appropriate.

The parameterization equations for the wind-wave skewness and asymmetry were inappropriate for the present dataset for Ursell numbers greater than 0.6. The relationship between skewness and the Ursell number as proposed by Doering and Bowen (1995) facilitated the expectation that as waves

become pitched forward due to shoaling (asymmetric), the skewness should begin to decrease. In the present case, the calculated asymmetry values seemed unaffected by the Ursell parameter. In fact, no significant asymmetry was experienced at this experiment location. As a result, measured skewness values continued to increase with the Ursell number.

The second parameterization technique, (Doering and Elfrink, 2000), was developed using genetic algorithms to determine the best relationship between the following dimensionless parameters: 1) H_s/h, 2) L/h, and 3) $\xi = \tan\beta/(H_s/L_o)^{0.5}$. These algorithms were applied to more than 55,000 samples from four different experiments. One of these experiments was at the same location and period as the experiment used to collect the present data.

It was found that once again, the formula did not fit the present data as stated by the authors. In fact, the relationship between the measured skewness and the skewness predicted using their formulation was very poor and insensible. This is curious since, as mentioned above, the formulation used data collected at the same experiment as the present research, albeit at a different location further from shore.

Once again, because this equation also predicts the eventual decrease in skewness with increasing Ursell number, the formula was inappropriate for the present dataset. In addition, for Ursell numbers less than 0.6, while the relationship is linear, the slope and intercept of the equation were inappropriate..

5.3 Conclusions

- In general, the velocity measurements were found to agree very well in the intercomparison. The cross-shore records exhibited the highest agreement for most parameters except for long-shore current comparisons. This is to be expected because the cross-shore orbital velocities are generally much larger than the long-shore orbital velocities and percent errors should therefore be smaller. Mean currents, however, were found to be much larger in the long-shore direction, resulting in smaller percentage error than for the cross-shore.

- It is suggested that ADV and EMCM instrumentation perform very similarly. The differences that were found cannot be necessarily attributed to instrument error because of the vertical and horizontal separation of the instruments. Velocities are expected to vary with depth and can be subject to localized variations.

- Further experimentation, involving ADV measurements taken from within a much closer proximity to the EMCM (e.g. <10 cm) would be necessary to compare the instrumentation to any higher degree.

- The mean flow has been shown to be an important contributor to velocity skewness. This should be considered when performing bispectral analysis, which removes the effect of the mean.

- Two parameterization techniques for estimating near shore velocity skewness arising from nonlinear interactions were tested using a significant amount of velocity data. These techniques, as presented by the authors resulted in tenuous relationships, at best.

- The equation proposed by Doering and Bowen, (1995), for estimating Biamplitude arising from wind-wave interactions was found to be unsuitable for this data with an r^2 value of 0.61.

- The equations proposed by Doering and Bowen, (1995), for estimating skewness and asymmetry did not appear to be suitable for this environment because of an apparent lack of asymmetry at the experiment location.

- The formulation proposed by Doering and Elfrink, (2000), for estimating Nearshore skewness was also not successful for this site because of the lack of asymmetry. It has been shown, however, that the form of the equation does seem to have merit for the present data for Ursell values less than 0.6, if the slope and intercept were modified accordingly.

- It is believed that both parameterization techniques have merit in situations where asymmetry is present causing an eventual decrease in skewness. Further research is necessary to understand the processes leading to wave asymmetry and the prediction of its presence.

References

Aubrey, D.G., W.D. Spencer and J.H. Trowbridge, Dynamic response of electromagnetic current meters, *Tech. rep. 84-20*, 150 p., Woods Hole Ocean. Inst., Woods Hole, Mass., 1984

Bagnold, R.A., Mechanics of marine sedimentation; in *The Sea*, **3**, 507-528, 1963.

Bagnold, R.A., An approach to the sediment transport problem from general physics, *U.S. Geological Survey*, Professional paper **422-I**, 37 p., 1966.

Bailard, J.A. and D.L. Inman, An energetics bedload model for a plane sloping beach: Local transport, *J. Geophys. Res.*, **86**, 2035-2043, 1981.

Baryla, A.J., Laboratory measurements of wave-induced near-bed velocity over a sloping natural sand beach, *M.Sc. Thesis*, Department of Civil Engineering, University of Manitoba, 1998.

Bowen, A.J., Nearshore velocity measurements and beach equilibrium, *Proc. Canadian Coast. Conf.*, National Research Council Canada, 21-30, 1980.

Bowen, A.J. and J.C. Doering, Nearshore sediment transport: Estimates from detailed measurements of the nearshore velocity field, *Proc. of the 19th Conf. on Coastal Eng.*, ASCE, 1703-1714, 1984.

Cornaglia, P., Sul regime della spiagge e sulla regulazione dei porti (On beaches), 1887.

Cornish, V., On sea beaches and sand banks, *Geol.*, **2**, 628-674, 1898.

Coulomb, C.A., Essai sur une application des regles de maximis et minimis a quelqeus problems de statique relatifs a l'architecture, *Med. Acad. Roy Divers Sav.*, **5**, 343, 1776.

Doering, J.C., Wave-Wave interactions in the nearshore, *Ph.D. Thesis*, Physical Oceanography, Dalhousie University, 1988.

Doering, J.C. and A.J. Bowen, Skewness in the nearshore zone: A comparison of estimates from Marsh-McBirney current meters and colocated pressure sensors, *J. Geophys. Res.*, **92**, 13,173-13,183, 1987.

Doering, J.C. and A.J. Bowen, Parameterization of orbital velocity asymmetries of shoaling and breaking waves using bispectral analysis, *Coastal Engineering*, **26**, 15-333, 1995.

Doering, J.C., B. Elfrink, D.M. Hanes and B.G. Ruessink, Parameterization of velocity skewness under waves and its effect on cross-shore sediment transport, *Coastal Engineering, Proc. Conf. ASCE 2000*, 1383-1396, 2000.

Eagleson, P.S. and R.G. Dean, Wave-induced motion of bottom sediment particles, *Am. Soc. Civil Eng. Trans.*, **126**, 1162-1189, 1961.

Eagleson, P.S., B. Glenne and J.A. Dracup, Equilibrium characteristics of sand beaches, *J. Hydr. Div. Am. Soc. Civ. Eng.*, **89**, 37-57, 1965.

Elgar, S.L. and R.T. Guza, Observations of bispectra of shoaling surface gravity waves, *J. Fluid Mech.*, **161**, 425-448, 1985.

Foote, Y, D. Huntley, M. Davidson, P. Russell, J. Hardisty and A. Cramp, Incident wave groups and long waves in the nearshore zone, *Proceedings of the 23rd Coastal Eng. Conf.*, 974-989, ASCE, 1992.

Foote, Y. and D. Huntley, Velocity moments on a macro-tidal intermediate beach, *Coastal Dynamics '94*, 794-808, ASCE, 1994.

Greenwood, B. and D.J. Sherman, Wave, currents, sediment flux, and morphological response in a barred nearshore system, *Mar. Geol.*, **60**, 31-61, 1984.

Guza, R.T. and E.B. Thornton, Local and shoaled comparisons of sea-surface elevations, pressure, and velocities, *J. Geophys. Res.*, **85**, 1524-1530, 1980.

Guza, R.T. and E.B. Thornton, Velocity moments in the nearshore, *J. Waterway, Port Coastal Ocean Div.*, ASCE, **111**, 235-256, 1985.

Guza, R.T., Comment on "Kinematic and dynamic estimates from electromagnetic current meter data" by D.G. Aubrey and J.H. Trowbridge, *J. Geophys. Res.*, 1337-1334, 1988.

Hasselmann, K., W. Munk, and G. MacDonald, Bispectra of ocean waves in *Time Series Analysis* (edited by M. Rosenblatt), pp. 125-139, Wiley, New York, 1963.

Hardisty, J., An assessment and calibration of formulations for Bagnold's bedload equation, *J. of Sedimentary Petrology*, **53**, 1007-1010, 1983.

Huntley, D.A. and A.J. Bowen, Comparison of the hydrodynamics of steep and shallow beaches, *Proc., Symposium on nearshore sediment dynamics and sedimentation*, J.R. Hails and A. Carr. (ed.), Wiley, London, England, 69-109, 1975.

Inman, D.L. and R.A. Bagnold, Littoral processes; in *The Sea*, **3**, 529-543, 1963.

Inman, D.L. and J.D. Frautschy, Littoral processes and the development of shorelines in *Proc. Coast. Eng. Spec. Conf.*, ASCE, 511-536, 1966.

Ippen, A.T. and P.S. Eagleson, A study of sediment sorting by waves shoaling on a plane beach, *Beach Erosion Board, Corps of Engineers*, tech. memo **63**, 83 p., 1955.

Kim, Y.C., and E.J. Powers, Digital bispectral analysis and its applications to non-linear wave interactions, *IEEE Trans. On Plasma Sc.*, **1**, 120-131, 1979.

Roelvink, J.A. and Stive, M.J.F., Bar-generating cross-shore flow mechanisms on a beach. *J. of Geoph. Res.*, **94**, 4785-4800, 1989.

SonTek, T.R., Acoustic Doppler Velocimeter (ADV) Principles of Operation, *SonTek tech. notes*, 15 p., SonTek, 1996.

Stokes, G.G., On the theory of oscillatory waves, *Trans. Cambridge Philos. Soc.*, **8**, 441-455, 1847.

APPENDIX A

Bispectral Theory

A.1 Bispectral Theory

If one considers a plot of cross-shore velocity vs. time such as in Figure A.1(b), a lack of symmetry with respect to the horizontal axis is known as wave skewness. Similarly, a time series that lacks symmetry with respect to the vertical axis indicates wave asymmetry, Figure A.1(c). Sediment transport in coastal beach environments has been shown to be dependent on velocity skewness, (Doering, 1988). The bispectrum can be used to determine the nonlinear coupling between frequencies responsible for skewed and asymmetric flow.

The bispectrum was first used to examine the nonlinearities of shallow water waves in 1963, (Hasselmann et. al., 1963). Since then, bispectral techniques have been used by many investigators to study the nonlinearities in a wide variety of fields including earth noise, machine vibrations, and shoaling surface gravity waves, (Elgar, 1985, Guza, 1985, and Doering, 1995).

If $\zeta(t)$ is a stationary random function of time, it can be represented as a superposition of statistically uncorrelated waves (*i.e.,* the phase of each wave is random). The variance spectrum of this time series completely characterizes it and phase information is not needed. However, if the phase of the Fourier components of $\zeta(t)$ are not randomly distributed, then $\zeta(t)$ is not Gaussian. In this case, the variance spectrum cannot completely characterize $\zeta(t)$. In such cases, however, one cannot tell from the power spectrum whether or not $\zeta(t)$ is Gaussian and nonlinearities can be overlooked. The bispectrum however, is capable of identifying deviations from a Gaussian form. It reveals the relative energy arising from frequency-frequency interactions, much like the power spectrum reveals the relative energy for single frequencies. The bispectrum is defined as the Fourier transform of the second-order covariance function (Hasselmann et. al., 1963).

$$B(f_1,f_2)=\int_{-\infty}^{+\infty}\int_{-\infty}^{+\infty}S(\tau_1,\tau_2)\,e^{-i(2\pi(f_1\tau_1+f_2\tau_2))}\,d\tau_1 d\tau_2 \tag{A.1}$$

where

$$S(\tau_1,\tau_2)=E[\zeta(t)\zeta(t+\tau_1)\zeta(t+\tau_2)], \tag{A.2}$$

τ_1 and τ_2 are lags, and E[ ] indicates an expected value. The bispectrum can also be expressed in terms of complex Fourier coefficients (Kim and Powers, 1979),

$$B(f_1,f_2)=E[A(f_1)A(f_2)A^*(f_3)] \tag{A.3}$$

where the convention is $f_1+f_2=f_3$, and * indicates complex conjugation. $B(f_1,f_2)$ will be zero, unless

i) there are waves present at the frequencies f_1, f_2, and f_3, and

ii) there is a phase persistence, or phase relation, between the waves at these frequencies.

Physically, if the waves present at f_1, f_2, and f_3 are not interacting with one another (normally excited modes), then each wave will be characterized by a statistically independent, or random phase, and the expected value of $B(f_1,f_2)$ will be zero. If, however, the sum or difference wave, f_3, is generated through an interaction between f_1 and f_2, then a phase relation will exist and the expected value of $B(f_1,f_2)$ will be non-zero.

Noting that A(f) = A*(-f) for real $\zeta(t)$, it can be shown that the bispectrum has the following symmetry relations:

$$\begin{aligned}B(f_1,f_2)=B(f_2,f_1)=B(f_1,-f_1-f_2)=B(-f_1-f_2,f_1)\\ =B(f_2,-f_1-f_2)=B(-f_1-f_2,f_2)\end{aligned} \tag{A.4}$$

The bispectrum is therefore uniquely defined by the first octant defined by

$$0\le f_1\le\infty,\quad 0\le f_1\le f_2 \tag{A.5}$$

The Nyquist frequency (fN), however, is the maximum resolvable frequency. It is customary to compute only the bispectrum in the first bifrequency region indicated in Figure A.2.

Due to finite length effects the bispectrum of a Gaussian process will most likely be non-zero. In order to determine which interactions are truly due to phase-coupled modes, it is useful to express the bispectrum in a normalized form known as the bicoherence. Kim and Powers, (1979), define the bicoherence spectrum as

$$b^2(f_1,f_2)=\frac{\left|B(f_1,f_2)\right|^2}{\mathrm{E}\left[\left|A(f_1)A(f_2)\right|^2\right]\mathrm{E}\left[\left|A(f_3)\right|^2\right]}. \tag{A.6}$$

Since $b^2(f_1,f_2)$ is normalized by the Fourier coefficients it is independent of the wave amplitude, $B(f_1,f_2)$ is not. For a large number of degrees of freedom, ν, the bicoherence is expected to be χ^2 distributed with 2 degrees of freedom. The 95% confidence limit on zero bicoherence is given by

$$b^2_{95\%}=\frac{5.991}{\nu}. \tag{A.7}$$

The bispectrum can be expressed in terms of a biamplitude and a biphase such that

$$B(f_1,f_2)=\left|B(f_1,f_2)\right|\mathrm{e}^{-i\beta(f_1,f_2)} \tag{A.8}$$

where $\beta(f_1,f_2)$ is the biphase and is given by

$$\beta(f_1,f_2)=\tan^{-1}\left\{\frac{\Im\left[B(f_1,f_2)\right]}{\Re\left[B(f_1,f_2)\right]}\right\}. \tag{A.9}$$

The integral of the real part of the bispectrum gives the third moment of $\zeta(t)$, (Hasselmann, et. al., 1963), such that

$$\mathrm{E}\left[\zeta^3(t)\right]=\int_{-\infty}^{+\infty}\int_{-\infty}^{+\infty}\Re\left\{B(f_1,f_2)\right\}df_1\,df_2 \tag{A.10}$$

where $\Re\{\}$ denotes the real part. The skewness of $\zeta(t)$ is found by normalizing equation B.8 by the variance of $\zeta(t)$ to the 3/2 power. Therefore,

$$S = \frac{E\left[\zeta^3(t)\right]}{E\left[\zeta^2(t)\right]^{3/2}}. \tag{A.11}$$

Similarly the integral of the imaginary part of the bispectrum is used to define the wave asymmetry of $\zeta(t)$ such that

$$A = \frac{\int_{-\infty}^{+\infty}\int_{-\infty}^{+\infty} \Im\{B(f_1, f_2)\}\, df_1\, df_2}{E\left[\zeta^2(t)\right]^{3/2}} \tag{A.12}$$

where $\Im\{\}$ denotes the imaginary part.

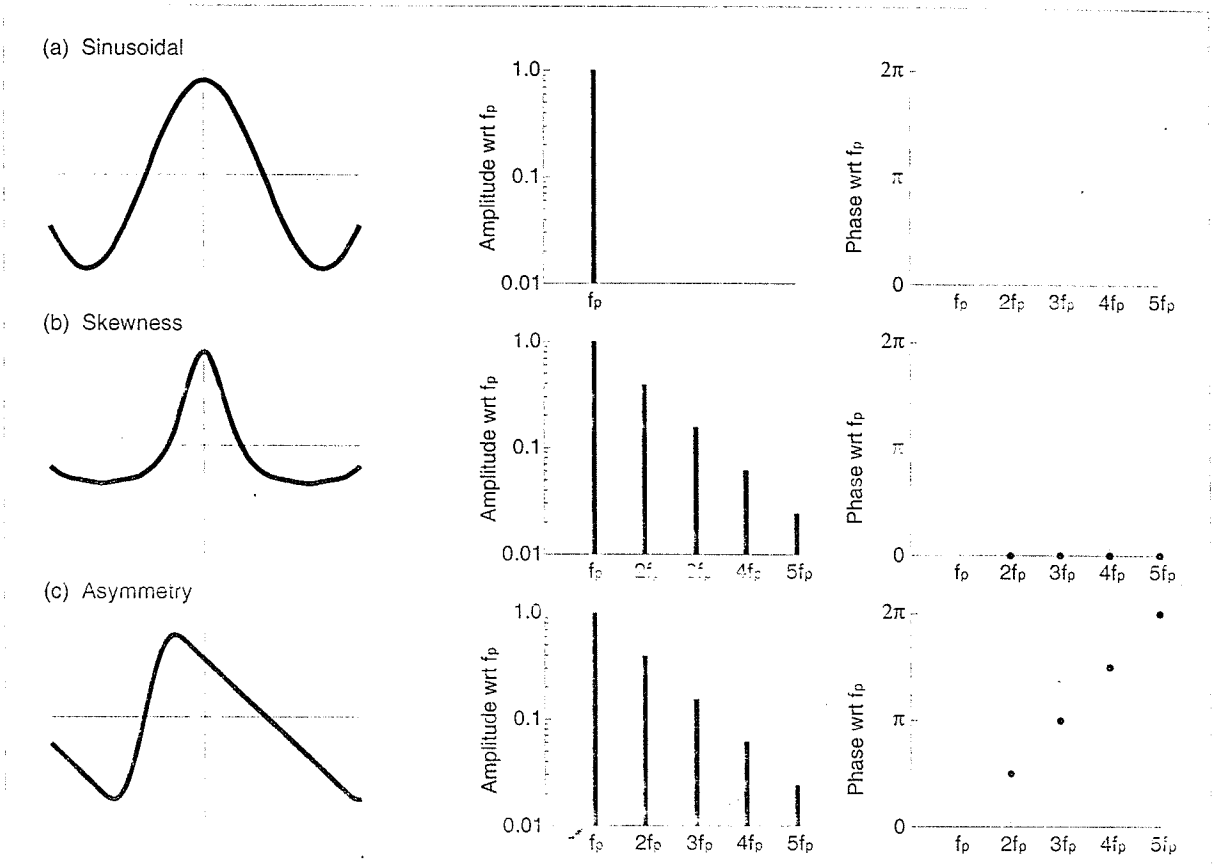

Figure A.1: Schematic showing **(a)** a sinusoidal profile that is symmetric with respect to both the horizontal and vertical axis. **(b)** A skewed profile, *i.e.*, one that lacks symmetry with respect to the horizontal axis. Note that this profile is vertically symmetric. **(c)** An asymmetric profile, *i.e.*, one that lacks symmetry with respect to the vertical axis. Note that this profile is horizontally symmetric. The spectral composition and phase of the harmonics with respect to the primary frequency (f_p) is shown to the right of the profiles. Notice that (b) and (c) have identical spectral compositions. However, the phase of the n^{th} harmonics is shifted by $n\pi/2$ for the asymmetric profile, whereas the harmonics are all phase-locked and in phase for the skewed Stokes-type wave. A phase relation between the harmonics and the primary other than that shown in (b) and (c) results in a profile that is both skewed and asymmetric. (source: *Doering*, 1988)

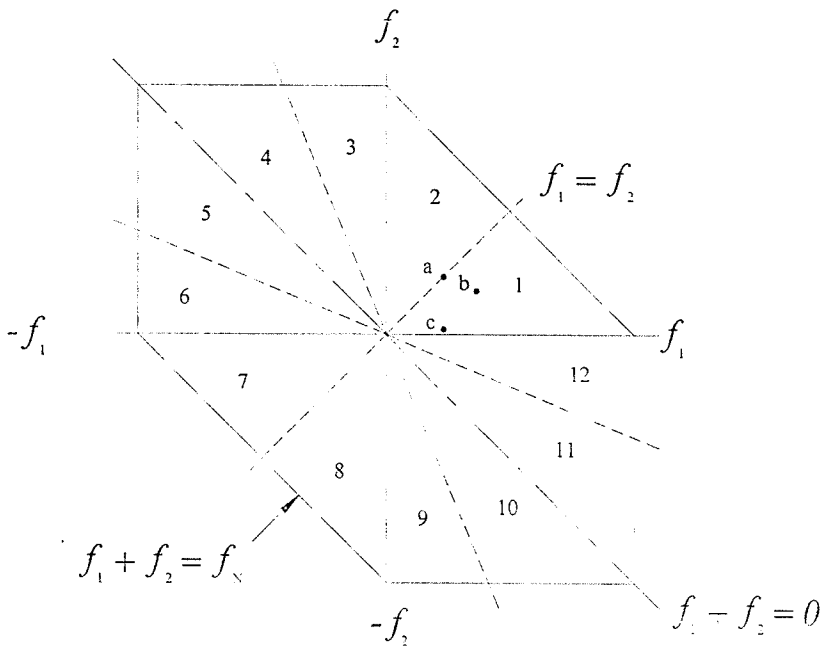

Figure A.2: Plan view of the bifrequency plane showing the area defined by a Nyquist frequency (f_N). Numbers indicate the twelve identical regions in the bispectrum. The six diagonals are indicated by ------. The line ——— indicates where $f_1 + f_2 \rightarrow f_3 = 0$. Points (a), (b) and (c) show where a self-self sum interaction, a general sum interaction, and a difference interaction, respectively, appear in the unique region (1) of the (auto) bispectrum. (*Doering, 1988*)